Title
Effects of Electronic Coherence in Ultrafast Spectroscopy

Author
Bennett, Kochise

Publication Date
2016

UNIVERSITY OF CALIFORNIA,
IRVINE

Effects of Electronic Coherence in Ultrafast Spectroscopy

THESIS

submitted in partial satisfaction of the requirements
for the degree of

MASTER OF SCIENCE

in Physics

by

Kochise Bennett

Dissertation Committee:
Professor Shaul Mukamel, Chair
Professor Craig Martens
Associate Professor Eric Potma

2016

TABLE OF CONTENTS

LIST OF FIGURES

LIST OF TABLES

ACKNOWLEDGMENTS

Foremost, I would like to thank my adviser, Professor Shaul Mukamel, for showing me a beautiful world I had never known. He is the smartest man I have met and it has been a true privelage to learn under his guidance. I would also like to thank my committee members, Professors Craig Martens and Eric Potma, for their generous contribution of time and effort.

I would like to thank all those incredible scientists and friends with whom I have worked in the Mukamel group over the years: Dr. Oleksiy Roslyak, Dr. Benjamin Fingerhut, Dr. Daniel Healion, Dr. Yu Zhang, Dr. Konstantin Dorfman, Dr. Weijie Hua, Dr. Frank Schlawin, Dr. Bijay Agarwalla, Dr. Arunangshu Debnath, Dr. Swapna lekkala, Dr. Jason Biggs, Dr. Alfonso Lam, Dr. Hideo Ando, Dr. Rachel Glenn, Dr. Markus Kowalewski, Dr. Jeremy Rouxel, and my fellow graduate student Prasoon Saurabh. In particular, I would like to thank my co-authors on the three articles that form the core of this thesis, Dr. Konstantin Dorfman and Dr. Markus Kowalewski. I have been very fortunate to have such stalwart talents to work alongside and have gained immesurably from the experience.

I would also like to thank all the friends, far too numerous to list, who have been a valuable source of companionship and support both during my time at UC-Irvine and in years past. I would also like to sincerely thank my parents for all they have done for me and contributed to my education; my mother for personally seeing to my for my early years of education, my father for working tirelessly to support me through college, and to both for their unending love and support. Finally, I would like to thank my wife May, who has been by my side throughout my graduate studies. Her love and guidance is a pillar of strength without which I would not be where I am.

Chapter 2 and portions of appendix adapted with permission from *Phys. Rev. A* **92**, 023826. Copyright (2015) American Physical Society

Chapter 3 and portions of appendix adapted with permission from *Phys. Rev. Lett.* **115**, 193003. Copyright (2015) American Physical Society

Chapter 4 and portions of appendix adapted with permission from *J. Chem. Theory Comput.*, **2016**, 12 (2), pp 740752 . Copyright (2016) American Chemical Society.

The co-authors listed in the above publications were instrumental in conducting the research on which this thesis reports.

CURRICULUM VITAE

Kochise Bennett

EDUCATION

Doctor of Philosophy in Physics **2016**
University of California-Irvine *Irvine, CA*

Master of Science in Physics **2016**
University of California-Irvine *Irvine, CA*

Bachelor of Science in Physics **2009**
University of California-Los Angeles *Los Angeles, CA*

RESEARCH EXPERIENCE

Graduate Research Assistant-Shaul Mukamel Group **2011–2016**
University of California, Irvine *Irvine, California*

TEACHING EXPERIENCE

Teaching Assistant-Introductory Graduate Laboratory Skills **Summer 2014–2016**
Universityof California, Irvine *Irvine, California*

Teaching Assistant-Graduate Molecular Spectroscopy **Spring 2012, 2013**
Universityof California, Irvine *Irvine, California*

Teaching Assistant **2010–2011**
Universityof California, Irvine *Irvine, California*

REFEREED JOURNAL PUBLICATIONS

Detecting Electronic Coherence by Multidimensional Broadband Stimulated X-Ray Raman Signals **2015**
Physical Review A

Catching Conical intersections in the Act: Monitoring Transient Electronic Coherences by Attosecond Stimulated X-Ray Raman Signals **2015**
Physical Review Letters

Nonadiabatic Dynamics May be Probed Through Electronic Coherence in Time-Resolved Photoelectron Spectroscopy **2015**
Journal of Chemical Theory and Computation

ABSTRACT OF THE THESIS

Effects of Electronic Coherence in Ultrafast Spectroscopy

By

Kochise Bennett

Master of Science in Physics

University of California, Irvine, 2016

Professor Shaul Mukamel, Chair

Electronic dynamics takes place on the attosecond timescale. Recent technological advancements permit the creation of light pulses with durations in the attosecond regime, opening up the possibility of monitoring this ultrafast dynamics in real time. In particular, it becomes possible to observe the time-dependent interference between material electronic states, thus tracking the electronic energies temporally. This information, originating in the coherence terms in the electronic density matrix, can provide spectral information in the time-domain. Such an approach is particularly useful when the desired information is transient. In this thesis, we examine how electronic coherences contribute to photoelectron and a variety of x-ray Raman signals. We then utilize photoelectron spectroscopy and linear off-resonant Raman (TRUECARS) to track the dynamics of a model system by way of example.

Chapter 1

Introduction

Light forms the basis of vision, our primary means of obtaining sensory data about the external world. Wtih Maxwell's seminal work in the early 1860's, the first steps were taken on the long road to understanding the nature of light and how it interacts with matter. A theory of light-matter interaction not only puts us in a position to comprehend in detail how our faculty of vision operates but also to pursue other means of using light to gain knowledge about objects. Indeed, the past century is replete with examples of the reciprocity of our understandings of light, matter, and how they interact. Attempts to explain blackbody radiation, the photoelectric effect, and atomic emission spectra, were all famously instrumental in the early development of quantum mechanics.

Since the pioneering work of Ahmed Zewail and the many who followed in his footsteps, it has been known that the ultrashort, coherent laser pulses that had recently been developed could be used to track the nuclear motion and thus monitor chemical dynamics in real time (see [2, 3] and references therein). The idea of creating molecular movies to visually reconstruct chemical reactions, obtaining clear physical pictures, is obviously very enticing. As pulse technology has continued to develop into the x-ray and attosecond regime, it has become possible to generate wavepackets of electronic excitations that evolve collectively as well as to probe ultrafast reaction dynamics such as occurs at certain key nuclear configurations called conical intersections, near which the nuclei move on a similar timescale to the electrons. The analysis of such signals and what information may be extracted from them has been an exciting area of recent inquiry. The goal of this manuscript is to introduce the basic formalism for describing a broad variety of spectroscopic techniques and analyze in depth several example signals, calculating them for a model system and demonstrating their information content in each case. We will show that attosecond x-ray spectroscopies form a powerful toolbox for monitoring ultrafast nuclear and electronic dynamics and, in particular, that the ability to monitor the time-dependent electronic coherences opens up exciting new ways to probe chemical dynamics in regions of NACs such as CIs or avoided crossings.

1.1 Background

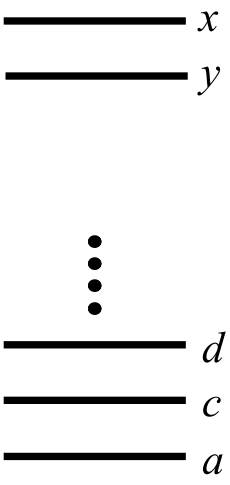

Figure 1.1: Level scheme for the broadband x-ray Raman experiment. a, c, d are low-frequency, valence electronic excitations and x, y are high-frequency core excitations.

Our goal in this manuscript will be to develop some understanding of the role of electronic coherences in ultrafast spectroscopies, typically on the attosecond-femtosecond timescales employing pulses in the extreme ultraviolet (XUV) to x-ray regime (we will refer to the pulses as "x-ray" throughout the manuscript). Although the discussion and formalism could be laid out quite generally, i.e., for an arbitrary energy-level scheme, we will concretize the subject by considering a system with two manifolds of electronic eigenstates; a lower manifold consisting of the ground state and valence excitations and an upper manifold consisting of a core excitation (core energy-levels are generally in the XUV to x-ray energy range) and valence excitation substructure (i.e., the direct product of a set of valence excitations and a single core excitation). This general level scheme is depicted in Fig. 1.1. Except for the scale of the energy gaps, this is the same level structure as formed by the direct product of a valence excitation and a set of vibrational excitations. As a result, the signals discussed generally possess analogs in the longer-wavelength regimes.

While our discussion of spectroscopic techniques must be limited in scope, we can gain a great deal of generality by introducing the "pump-probe" conceptual framework. We can imagine an arbitrarily-complex state preparation process (the pump) that yields an initial state. The state is allowed to evolve freely for some time before analysis via a probe, which may consist of one or more pulses. As long as the externally applied potentials (the pump and probe) are temporally well-separated, this dissection of the interactions into pump and probe is unambiguous. Since any technique could be considered as a sufficiently-complex probe, this separation is somewhat artifical. It is useful, however, to focus on what information about a given initial state may be obtained from different probing processes in a general sense. We thus consider the pumped state as arriving from a black-box process and express the signals in terms of the evolution of this pumped state. In this manuscript, we will limit our discussion to transient absorption, various types of Raman, and photoelectron spectroscopy. These correspond to direct transitions between core levels (i.e., intermanifold transitions), Raman transitions between valence levels (i.e., intramanifold transitions), or direct excitation of electrons to continuum states which are not yet included in our model and will be added in chapter 4. Through this development, we will discover that our analysis naturally leads to a large catalog of possible signals, some of which are quite novel [**?**]. An understanding of each of these possible probes and what information it accesses gives us a toolbox of techniques to probe system dynamics at various energies and timescales.

While the most obvious distinguishing feature of x-ray pulses is that they are a direct probe of core-level excitations, they possess two distinguishing and complementary features; a large bandwidth (on the order of eV) and an ultrashort duration (as-fs). The first of these properties permits the creation of wavepackets of valence electronic excitations via x-ray Raman processes, as well as the simultaneous probing of a broad spectral region. The second property permits the probing of ultrafast dynamics and, together, these imply the abilitiy to create wavepackets of valence excitations and monitor their subsequent evolution, in analogy to the use of lower-energy Raman interactions to create and monitor vibrational wavepackets. An equally exciting application however, is the possibility of monitoring ultrafast nuclear dynamics, and thus chemical reactions. This would allow the probing of reactions that take place on too-short a timescale for other spectroscopic techniques. Thus, although the energy-scales being probed in the problem might not seemingly call for an x-ray probe, the timescales might make x-rays necessary.

The inclusion of nuclear degrees of freedom, on top of the electronic, complicates matters since there are now three energy scales (vibrational, valence, and core). Equivalently, this introduces an additional level of time-dependence not present vibrational-valence spectroscopy and opens up a brand new avenue to probing nuclear dynamics. There are various levels of theory at which this topic may be approached. From the eigenstate perspective, the inclusion of the nuclear degrees of freedom adds a vibrational substructure to the valence excitations. Generally, a complete eigenstate solution of the joint electronic-nuclear is numerically taxing, particulary with more than one relevant nuclear coordinate. However, we are interested only in spectroscopic signals, which are determined by the transient response of the material. Fortunately, this response, and the associated signals, can be obtained via a direct, real-space time-propagation scheme (such as the Lanczos algorithm) described in appendix C.1 that is much faster than a full diagonalization.

Chemical reactions can be understood in terms of the motion of molecular nuclei along energy surfaces, the shape of which is determined by the electronic eigenvalue problem

$$\hat{H}_{\mathrm{el}}(\hat{\mathbf{q}})|\varepsilon_l(\hat{\mathbf{q}})\rangle = \hat{\varepsilon}_l(\hat{\mathbf{q}})|\varepsilon_l(\hat{\mathbf{q}})\rangle \tag{1.1}$$

where $\hat{H}_{\mathrm{el}}$ is the electronic Hamiltonian, $|\varepsilon_l(\hat{\mathbf{q}})\rangle$ is the state with energy $\hat{\varepsilon}_l(\hat{\mathbf{q}})$ and l runs over valence (a) and core (x) excitations. This equation is solved for each value of the nuclear coordinates, yielding the set of energy surfaces that determine the nuclear dynamics. The set of nuclear coordinates is collectively denoted $\hat{\mathbf{q}} \equiv \{\hat{q}_1, \ldots, \hat{q}_n\}$, the exact number of which is not important but we label as n for concreteness. Throughout this manuscript, we will use bold to indicate a vector quantity and the circumflex to represent an operator. The treatment of the nuclei is thus fully quantum-mechanical and the electronic energy $\hat{\varepsilon}_l$ is an operator due to the nuclear dependence. This procedure is known as the Born-Oppenheimer approximation (BOA) and is exact in the adiabatic limit in which the nuclei move infinitesimally slowly relative to the electrons. This picture can be fully corrected by the inclusion of intersurface couplings, called non-adiabatic couplings (NACs) or Non-BOA terms, that are due to the nuclear kinetic energy operator. These terms are often negligible but become important when the electronic potential surfaces cross (a conical intersection or CI) or nearly so (a so-called avoided crossing). These important, and not uncommon, exceptions to the BOA are an active area of research and will inform the model we analyze in chapters 3 and 4. In this manuscript, we will not concern ourselves with the solution of the electronic eigenvalue problem or the determination of the electronic transition dipole moments or NACs, taking these to be given as functions of the nuclear coordinates. The practical calculation of these quantities is generally a highly nontrivial problem that forms the subject of quantum chemical electronic structure theory.

To approach the problem of spectroscopic signals dependent on nuclear, valence, and core dynamics, we proceed in two steps. We first give an account of off-resonant and resonant x-ray Raman spectroscopy under the assumption of static nuclei (chapter 2), developing a multitude of probe techniques and giving examples of each for a sample level-scheme so as to illustrate their properties and use. The subsequent chapter utilizes one of these techniques, the off-resonant linear technique with a shaped pulse (known as TRUECARS), to examine the dynamics of a schematic 1-D model system as well as a more realistic 2-D model representing a CI in acrolein. This technique has a unique sensitivity to electronic coherences and is particularly easy to simulate. In chapter 4, we discuss time-resolved photoelectron spectroscopy (TRPES) and utilize this example to explore several levels of theory at which the nuclear motion may be included before simulating the photoelectron signal for the 1- and 2-D model systems of chapter 3. While TRUECARS and TRPES are only a few of the many possible signals, including those discussed in chapter 2, their analysis is sufficiently informative to provide a qualitative understanding of what other probes might yield and a general picture of the role of various probes in our toolbox.

1.2 Defining the Problem

In this section, we begin to formalize the above discussion and lay the groundwork for the evaluation of signals in the following chapter. Along the way, we will elucidate the assumptions under which we approach the problem. Spectroscopic signals are calculable via the time-dependent expectation value of a material operator. Throughout the manuscript, we evaluate these expectation values perturbatively in the electric field amplitude using the interaction picture with respect to the field-matter interaction. Terms in this perturbation series expansion are represented by loop diagrams [4, 5] in Hilbert space, which we employ in favor of the Liouville-space theory. The Liouville-space description is necessary when system-bath coupling is important and pure dephasing alters the dynamics. However, it complicates the description of the signals by forcing us to work with ladder diagrams, which are more numerous than loop diagrams since the relative order of ket vs. bra interactions is then important. Such an extension is necessary to fully describe the decoherence times but not to analyze the impact of electronic coherences while they remain, though it clearly has practical bearing on the observability of certain signals. As will be discussed in greater detail below, the present treatment is even general enough to incorporate system-bath interactions during the pump or the pump-probe delay period provided that such interactions are negligible during the probing process itself.

In this manuscript, we consider a system of identical, non-interacting molecules coupled to an externally applied electric field. Aside from a wavevector phase-matching factor that enforces momentum conservation, the response from such a system is just the response of a single molecule scaled by the number of molecules in the sample. The phase-matching condition is important experimentally for discriminating various signals (such as the various contributions to four-wave-mixing spectroscopy [6]) and justifies the focus on particular diagrams but does not affect the calculation of those diagrams, and thus the signals. We will thus generally ignore the phase-matching condition, only recollecting it occasionally to discuss the contributions of various diagrams. While most experiments are performed on many-molecule samples, many samples are sufficiently dilute so that their constituent particles may be considered as non-interacting. There are corrections to this picture, such as cascading contributions and molecule-molecule interactions, but they are beyond the scope of the present work. Within the dipole approximation, such a system can be described by the following Hamiltonian

$$\hat{H}(t) = \hat{H}_{\text{mol}} + \hat{H}_{\text{field}} + \hat{H}_{\text{I}}(t) \tag{1.2}$$

where

$$\hat{H}_{\mathrm{mol}} = \hat{T} + \hat{H}_{\mathrm{el}} = -\frac{1}{2}\sum_i \frac{1}{m_i}\nabla_i^2 + \sum_l \hat{\varepsilon}_l(\mathbf{q})|\varepsilon_l(\hat{\mathbf{q}})\rangle\langle\varepsilon_l(\hat{\mathbf{q}})|. \tag{1.3}$$

is the molecular Hamiltonian written as the sum of the nuclear kinetic energy $\hat{T}$ and the electronic Hamiltonian $\hat{H}_{\mathrm{el}}$,

$$\hat{H}_{\mathrm{field}} = \int \frac{d^3\mathbf{k}}{(2\pi)^3}\omega_{\mathbf{k}}\hat{a}^{\dagger}_{\mathbf{k}}\hat{a}_{\mathbf{k}} \tag{1.4}$$

is the Hamiltonian of the electromagnetic field written in terms of creation and annihilation operators, $\hat{a}^{\dagger}_{\mathbf{k}}$ and $\hat{a}_{\mathbf{k}}$, for field mode $\mathbf{k}$, and

$$\hat{H}_{\mathrm{I}} = -\hat{\mathbf{E}}(t)\cdot\hat{\mathbf{V}}(t) \tag{1.5}$$

is the dipolar field-matter coupling written in terms of the electric field operator $\hat{\mathbf{E}}(t)$ and the electronic transition dipole operator $\hat{\mathbf{V}}(t)$. We utilize atomic units ($\hbar = e = m_e = 1$) throughout and all time-dependencies are due to working in the interaction picture, wherein the interaction-free evolution is built into the operators. For an arbitrary operator $\hat{O}$, we have

$$\hat{O}(t) \equiv e^{i(\hat{H}_{\mathrm{mol}}+\hat{H}_{\mathrm{field}})t}\hat{O}e^{-i(\hat{H}_{\mathrm{mol}}+\hat{H}_{\mathrm{field}})t}. \tag{1.6}$$

where we could include $\hat{H}_{\mathrm{field}}$ in this interaction-free propagation for completeness but it will not be relevant in this manuscript since the quantum-nature of the field will only be used to derive arbitrary-order signal expressions (see appendix A), a semiclassical treatment being invoked for the actual calculation of expectation values. Note that, due to the dipole approximation and the single-molecule assumption, the spatial structure of the field is not relevant. The single-molecule assumption can be relaxed and, provided the field-matter interaction volume is large compared to the wavelength, the associated spatial integration over the phase factors $e^{i\mathbf{k}\cdot\mathbf{r}}$ is the origin of the aforementioned delta-function enforcing momentum conservation and the factor of the number of molecules in the sample. Such complications must be taken into account when considering wavevector-dependent signals, such as four-wave mixing, probing the spatial structure, as in diffraction, or discussing the effects of molecule-molecule interactions. The expansion of the electric field operator in plane wave modes is given by Eq. A.2 and the electronic transition dipole operator can be written as

$$\hat{\mathbf{V}}(t) = \sum_{xa} \hat{\mathbf{V}}_{xa}(\hat{\mathbf{q}}, t) |\varepsilon_x(\hat{\mathbf{q}})\rangle\langle\varepsilon_a(\hat{\mathbf{q}})| + \text{H.c.}, \tag{1.7}$$

where we we consider only core-valence transition dipole moments in this manuscript. This reflects our focus on x-ray wavelengths, beyond the range of valence excitations. Note that the electronic Hamiltonian, $\hat{H}_{\text{el}}$, is presumed diagonalized. In this manuscript, we do not discuss the problem of determining the electronic structure or its solution, but rather take the eigenstates, eigenvalues, and transition dipole moments $\hat{\mathbf{V}}_{kl}(\hat{\mathbf{q}})$ to be given from quantum chemistry calculations.

A vast array of spectroscopic signals and techniques can be understood from studying the evolution and properties of systems described by Eq. 1.2. Neglecting the $\hat{\mathbf{q}}$-dependence leads to a simplified Hamiltonian that applies to molecules in which the nuclei are static on the experimental timescale as well as to atoms, the latter of which lack internal nuclear coordinates. Time-dependence in spectroscopic signals is then determined by the electronic eigenfrequencies. The overlay of the coupled electronic-nuclear dynamics continuously changes these frequencies, complicating the signal but providing information on the evolution of the system. Additionally, the nuclear kinetic energy operator $\hat{T}$ can couple electronic energy levels, leading to transitions between electronic states that become important near avoided crossings or CIs.

While an exception to the Born-Oppenheimer approximation, CIs are ubiquitous in chemistry and determine the outcome and rates of nearly all photochemical reactions. By coupling nearby electronic surfaces, NACs provide radiationless de-excitation pathways for photo-excited molecules. This mechanism is well-known to serve the function of protecting the DNA base thymine from photodamage via UV excitation from sunlight as well as…and countless other examples. It is no surprise then that conical intersections have been an active area of intense research. The complicated entangled dynamics of the nuclei with valence and core electrons makes spectroscopic signals more difficult to interpret but allows a window into the progression of chemical reactions at crucial points in time. Making sense of spectroscopic signals that probe this complicated regime, transient dynamics of multiple, interacting energy-scales, requires tools that lie at the intersection of attosecond x-ray science, theoretical spectroscopy, quantum chemistry, and quantum dynamics. Clearly, this is a huge field of research and we cannot hope to offer more than a modest introduction backed by hopefully helpful and clear examples.

Chapter 2

Spectroscopy of Electronic Excitations

Many spectroscopic techniques involve the creation and manipulation of coherences followed by a stimulated Raman detection of a probe pulse [7, 8, 9, 10, 11, 12, 13, 14, 15, 16, 17, 18]. The field of multidimensional spectroscopy was launched by looking at the delays between impulsive stimulated Raman events [19]. In the simplest conventional one-dimensional (1D) time-domain stimulated Raman technique, the molecule is first prepared in a vibrational superposition state by an off-resonant Raman pulse and, after a variable delay period T, the transmission change of a second probe pulse is detected. The transmission oscillates with T between gain and loss at the vibrational period, and a Fourier transform then reveals the vibrational frequencies [20, 21, 22]. Optical Raman techniques have been applied to study electron transfer and nonadiabatic dynamics at conical intersections. Using recently developed FEL and HHG sources [23, 24, 25], Raman techniques can be further extended to the X-ray regime [26, 27, 28, 29, 30] whereby the system is initially prepared in the superposition of valence electronic states and an X-ray Raman probe then reveals information about electronic, rather than vibrational, coherence.

In this chapter, largely adapted from reference Ref. [31], we give an account of electronic spectroscopy neglecting nuclear motion. The analysis thus applies to atoms or to molecules in the frozen-nuclei approximation. First, in section 2.1, we describe off-resonant Raman signals. These can be understood with a simplified interaction Hamiltonian in which the linear polarizability $\hat{\alpha}$ is coupled to the electric field intensity, rather than the dipole being coupled to the field amplitude. In the second section, we generalize the previous discussion, defining the resonant linear polarizability $\hat{\alpha}(\omega)$ in terms of which resonant Raman as well as transient absorption and stimulated emission signals may be written. Throughout this chapter, we omit reference to the nuclear coordinates $\hat{\mathbf{q}}$, which will be reintroduced next chapter.

In sections 2.1-2.2, we consider both linearly- and quadratically-scaling terms in the electric field intensity. The basis of our description will be a frequency dispersed signal

$$S^{(\mathrm{fd})}(\omega_s, \Lambda) = \int dt \langle \dot{\hat{N}}_s \rangle (t) \tag{2.1}$$

defined as the integrated rate of change of photons in a "signal" mode of the electromagnetic field, i.e., the frequency-dispersed probe transmission. Note that defining the signal in this way assumes that one particular mode can be discriminated and seperately observed, i.e., an infinitely sharp spectrometer. Equation (2.1) depends on the set of parameters Λ defining the pulse parameters and the initial state (pumped) state of the system. Other detection protocols can be defined in terms of this base signal. In particular, we can define the total photon gain/loss as well as the field energy gain/loss

$$S^{(N)}(\Lambda) = \int d\omega S^{(\mathrm{fd})}(\omega_s, \Lambda) \qquad\qquad S^{(\mathrm{E})}(\Lambda) = \int d\omega \omega S^{(\mathrm{fd})}(\omega_s, \Lambda). \tag{2.2}$$

These are just the zeroth and first moments of the frequency-dispersed signal. They have straightforward physical interpretations and provide a different perspective on the system dynamics, as will be demonstrated with both resonant and off-resonant signals. Moreover, they require no frequency-selective detectors or spectrometers and are thus easier to implement easier to implement experimentally.

The information accessed in the above signals obviously depends to a high degree on the pulse shapes, which we must therefore specify to give example spectra. We will consider two cases, experiments performed with pulses of arbitrary bandwidth (termed broadband) and experiments performed with hybrid broadband-narrowband pulses formed by the temporal overlay of their constituents. Depending on the signal, the latter can decouple the spectral and temporal resolution, since they will be determined by different components of the field the intensities of which are separately scalable. However, pure broadband signals are simpler experimentally and the additional complication may not be necessary depending on the system and what information is sought. This will be quantified and explicated further after the presentation of the signals.

Throughout, we apply the signals to a simple model system to analyze the electronic level structure and dynamics of perturbatively-prepared excitations. This analysis reveals several differences in the way that electronic coherences versus populations contribute to the various signals. This understanding will be exploited in the next chapter when nuclear dynamics are considered.

2.1 Off-Resonant Raman Signals

The field-matter interaction Hamiltonian for an off-resonant Raman process is given by

$$\hat{H}_{\mathrm{I}}(t) = \hat{\alpha}^{(0)}(t)|\mathcal{E}(t)|^2, \tag{2.3}$$

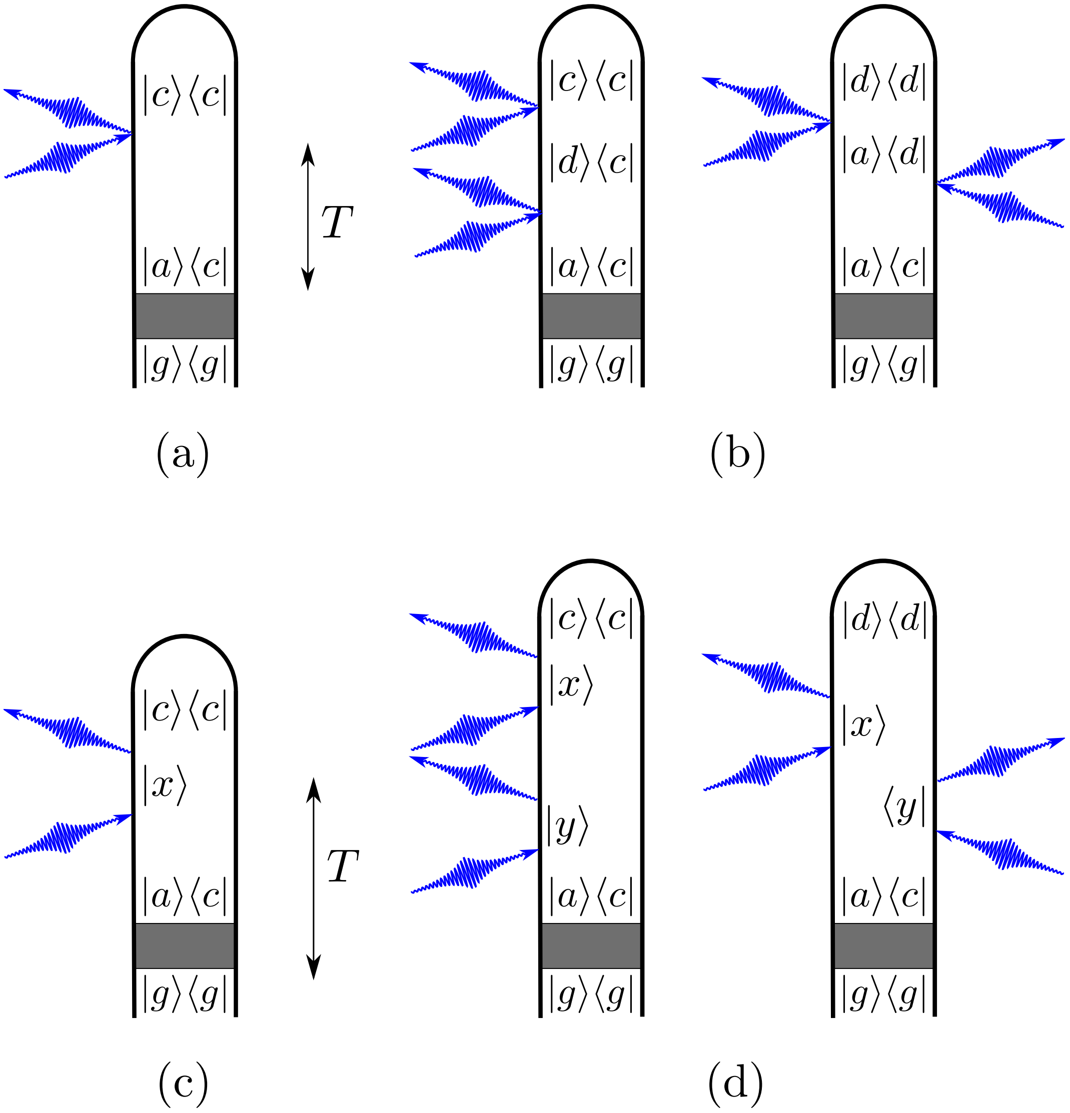

Figure 2.1: Loop diagrams representing the off-resonant linear (a) and quadratic (b) signals as well as the resonant linear (c) and quadratic (d) signals. In all diagrams, the system is assumed to be prepared from the ground state by some unspecified process (depicted by the grey rectangles). The preparation process terminates at time τ_0 after which the system evolves freely until it begins interacting with the probe which is taken to be centered at time t_0. The delay parameter $T = t_0 - \tau_0$ is therefore shown next to the diagrams. Note that in the off-resonant case, no core-valence coherences are created while these are created for certain times in the resonant case. For the linear processes ((a) and (c)), $\omega_{ca} > 0$ implies a red (Stokes) contribution while the reverse condition implies a blue (anti-Stokes) contribution. For quadratic signals, this analysis holds only for one of the two relevant diagrams and so the quadratic signals are more difficult to interpret (since it depends on the state d). Details of the loop diagrams are given in [1].

where $\alpha^{(0)}$ represents the off-resonant, polarizability, which is a Hermitian operator in the valence space. That is, it is assumed to have the structure

$$\hat{\alpha}^{(0)} = \sum_{ab} \alpha^{(0)}_{ab} |a\rangle\langle b|. \tag{2.4}$$

In many systems, there are dipole-forbidden transitions due to symmetry. That is, there exist at least some states for which V_{ab} vanishes identically. These transitions are therefore inaccessible via direct dipolar excitation as in transient absorption. This is an important fact and is one of the key reasons to perform Raman experiments in the first place. The separation into absorption- and Raman-active modes is well-known in the context of vibrational spectroscopy in the infrared wavelengths [32, 6]. All this being said, we will not be concerned with the selection rules associated with $\hat{\alpha}$ as we will not be comparing to direct valence spectroscopy (i.e., in the visible to deep UV range or on the order of eV).

The frequency-dispersed transmission of the probe pulse (heterodyne-detected, frequency-dispersed photon-number change) is given by

$$S^{(\text{fd})}_{\text{O}}(\omega, \Lambda) = 2\Im \int_{-\infty}^{\infty} dt e^{i\omega(t-t_0)} \mathcal{E}^*(\omega)\mathcal{E}(t)\langle\hat{\alpha}^{(0)}(t)\rangle(t), \tag{2.5}$$

where The O subscript indicates an off-resonant signal, and $\Im(\Re)$ denotes the imaginary (real) part. From Eqs. (2.2), we have

$$S^{(N)}_{\text{O}}(\Lambda) = 2\Im \int dt |\mathcal{E}(t)|^2 \langle\alpha^{(0)}(t)\rangle(t) \tag{2.6}$$

$$S^{(\text{E})}_{\text{O}}(\Lambda) = -2\Re \int dt \dot{\mathcal{E}}^*(t)\mathcal{E}(t)\langle\hat{\alpha}^{(0)}(t)\rangle(t) \tag{2.7}$$

where, for brevity, we suppress the limits of integration when the domain is all-space (i.e., $\int_{-\infty}^{\infty} \to \int$), a convention we will adopt throught this manuscript. Before proceeding to analyze the particular information one obtains from these signals, we can already tell some general features of off-resonant Raman. As the integrand in (2.6) is real, $S_{\mathrm{O}}^{(N)}$ identically vanishes at all orders. Thus, there is no net emission or absorption of photons. Instead, off-resonant Raman processes preserve the total number of photons while redistributing them betwen modes of the electromagnetic field, using the matter degrees of freedom as intermediaries. This leads to a red (Stokes) or blue (anti-Stokes) shift in the pulse spectrum corresponding to a loss or gain of field energy due to interaction with the material.

As described in appendix D.0.2, the expansion of Eqs. (2.5)-(2.7) perturbatively in $\hat{H}_{\mathrm{I}}$ to obtain signals may be done with the density matrix ρ or, assuming a pure state, with the wavefunction $|\psi\rangle$. In this chapter, we will present formal time-domain expressions in both representations as well as eigenstate expansions of these in the more general density-matrix representation. As discussed in appendix D.0.2, the time-evolution in the two pictures will be the same since we assume Hamiltonian (commutator) evolution of ρ during the probing process. The difference then is simply the compact handling of the mixed state. Thus, depending on the state of the system, we use one of

$$\langle\hat{\alpha}^{(0)}(t)\rangle(t) = \langle\psi(\tau_0)|\hat{U}^{\dagger}(t,\tau_0)\hat{\alpha}^{(0)}(t)\hat{U}(t,\tau_0)|\psi(\tau_0)\rangle \leftrightarrow \mathrm{Tr}\,[\hat{\alpha}^{(0)}(t)\hat{U}(t,\tau_0)\rho(\tau_0)\hat{U}^{\dagger}(t,\tau_0)] \tag{2.8}$$

where $U(t,t') = \mathcal{T}e^{-i\int \hat{H}_{\mathrm{I}}(\tau)d\tau}$ is the time-ordered exponential propagator and $|\psi(\tau_0)\rangle$ $(\rho(\tau_0))$ is the state (density matrix) immediately following the end of the pumping process. To obtain explicit expressions for off-resonant signals, we need only expand Eqs. (2.5)-(2.7) to the desired order. As mentioned above, these can then be evaluated either by taking matrix elements in the molecular eigenstates or via direct propagation. This latter approach is more easily carried out in the wavefunction representation and we therefore give formal expressions both in terms of ρ and $|\psi\rangle$.

2.1.1 Linear Off-Resonant Raman Signals

Expanding Eq (2.5) to linear order in the field intensity, i.e., zeroth order in the interaction Hamiltonian, we obtain

$$S_{\mathrm{OL}}^{(\mathrm{fd})}(\omega, T) = 2\Im \int dt e^{i\omega(t-t_0)} \mathcal{E}^*(\omega)\mathcal{E}(t) \,\mathrm{Tr}\,[\hat{\alpha}^{(0)} e^{-i\hat{H}_0(t-\tau_0)} \rho(\tau_0) e^{i\hat{H}_0(t-\tau_0)}], \tag{2.9}$$

where we explicitly list only the most important of the pulse-dependent parameters, the delay time T. It is also worth recalling that, as throughout this manuscript, we assume the pump and probe are temporally well-separated so that $\mathcal{E}(t) = 0$ for $t \leq \tau_0$. When working with a pure state, the trace operation can be recast as a usual wavefunction expectation value.

$$\mathrm{Tr}\,[\hat{\alpha}^{(0)} e^{-i\hat{H}_0(t-\tau_0)} \rho(\tau_0) e^{i\hat{H}_0(t-\tau_0)}] = \langle \psi(\tau_0) | e^{i\hat{H}_0(t-\tau_0)} \hat{\alpha}^{(0)} e^{-i\hat{H}_0(t-\tau_0)} | \psi(\tau_0) \rangle, \tag{2.10}$$

This technique would seem the simplest, most obvious to examine. Yet, from the diagram in figure 2.1(a), it is clear that no transitions are possible in the absence of coherences in the initial density matrix. It is then as if the pulse did not interact at all with the material and the signal would thus vanish. Thus, this signal is frequently unobserved due to the absence of electronic coherences.

This technique is essentially a stimulated Raman pump-probe and is the off-resonant analogue of transient absorption. Here, the photons undergo a redistribution among field modes rather than being absorbed.

Linear Broadband (LB) Probe

We now expand the signal (Eq. (2.9)) in molecular eigenstates and substitute into Eq. (2.2) to obtain

$$S^{(\mathrm{fd})}_{\mathrm{OLB}}(\omega, T) = -2\sum_{a,c} |\mathcal{E}(\omega)||\mathcal{E}(\omega - \omega_{ac})|\alpha^{(0)}_{ca}|\rho_{ac}| \sin\phi_{ac}(T), \tag{2.11}$$

$$S^{(\mathrm{E})}_{\mathrm{OLB}}(T) = -\sum_{a,c}\int \frac{d\omega}{2\pi}|\mathcal{E}(\omega)||\mathcal{E}(\omega - \omega_{ac})|\alpha^{(0)}_{ca}|\rho_{ac}|\omega_{ac} \sin\phi_{ac}(T). \tag{2.12}$$

Here, $\rho_{ac} = |\rho_{ac}|e^{i\phi^{\rho}_{ac}}$ is the initial density matrix, the phase is given by $\phi_{ac}(T) = \omega_{ac}T - \phi^{\rho}_{ac}$, and we neglect the linewidth for the valence states. In Eq. (2.11), terms in which $\omega_{ac} > 0$ ($\omega_{ac} < 0$) lead to broad peaks below (above) the central pulse frequency which we denote as "red" ("blue") in allusion to the direction of the spectral shift. Each pair of states therefore generates a complementary pair of red and blue contributions. The two oscillate in T with a π phase shift (as sine is an odd function of its argument). The frequency-dispersed signal therefore oscillates between Stokes (positive red contributions and negative blue) and anti-Stokes (negative red contributions and positive blue) processes as shown in Fig. 2.2(a1).

Equation (2.12) is plotted in Fig. 2.2(b1) but, aside from indicating that some nontrivial phase is involved (since the signal doesn't vanish for $T \to 0$), not much information is directly apparent from the time-domain measurement. Taking the Fourier transform $\int dTe^{i\Omega T}S(T) = S(\Omega)$ (Fig. 2.2(c1)) reveals peaks at each transition energy ω_{ac} whose heights are given by the factor $\omega_{ac}\alpha_{ca}|\rho_{ac}|$. The ratios of these peak heights thus give information on the polarizabilities or the magnitudes of the initial coherences. Finally, it is worth noting that $\phi_{aa}(T) = 0, \forall T$ so that populations do not contribute to the off-resonant linear broadband signal. This confirms the aforementioned fact that these signals provide a background-free detection of electronic coherences, a useful property that will be leveraged in chapter 3.

Linear hybrid (LH) probe

A hybrid probe is a shaped pulse consisting of a broadband attosecond pulse $\mathcal{E}(\omega) = |\mathcal{E}_0(\omega)|e^{i\phi_0}$ and a narrowband femtosecond pulse $\mathcal{E}_1(t) = |\mathcal{E}_1|e^{-i\omega_1 t+i\phi_1}$ centered at frequency ω_1. The signal is the frequency-dispersed transmision of the broadband component and, in this case, Eq. (2.9) yields

$$S^{\text{(fd)}}_{\text{OLH}}(\omega,\omega_1,T) = -4\pi|\mathcal{E}_0(\omega)||\mathcal{E}_1|\sum_{a,c}\alpha^{(0)}_{ca}|\rho_{ac}|\sin\phi^1_{ac}(T)\delta(\omega-\omega_1-\omega_{ac}), \tag{2.13}$$

where $\phi^1_{ac}(T) = \omega_{ac}T - \phi^\rho_{ac} + \phi_0 - \phi_1$. Note that if the broadband and the narrowband components have the same phase, $\phi_0 = \phi_1$, then $\phi^1_{ac}(T) = \phi_{ac}(T)$. Due to the dependence on the relative phase of the pulses $\phi_0 - \phi_1$, observation of the linear hybrid signals requires phase-control (averaging over random ϕ_0, ϕ_1 causes the signal to vanish). Eq. (2.13) yields clearly resolved Raman resonances unlike the LB case where the red ($\omega_{ac} > 0$) and blue ($\omega_{ac} < 0$) components only enter through the pulse envelope. This signal, depicted for $\omega_1 = \omega_0$ in Fig. 2.3(a1), shows sharp peaks at each transition frequency ω_{ac}. Of particular significance is the ability to extract the phase ϕ^ρ_{ac} from the oscillations of the separate peaks. This information is not available in the *LB* signal.

Calculation of the energy change is slightly more subtle; the hybrid pulse contains both broad and narrowband components and we need to take into account the contribution to the signal where the last interaction is with narrowband component. This results in

$$S^{\text{(E)}}_{\text{OLH}}(\omega_1,T) = -4\pi\sum_{a,c}|\mathcal{E}_1||\mathcal{E}_0(\omega_1-\omega_{ac})|\alpha^{(0)}_{ca}|\rho_{ac}|\omega_{ac}\sin\phi^1_{ac}(T). \tag{2.14}$$

Note the similarity between this and Eq. (2.11) (they only differ by the factor $\omega_{ac}\mathcal{E}(\omega)$). The ω integration erodes the sharp resolution afforded by the narrowband pulse, leaving virtually the same result as the $S^{\text{(fd)}}_{\text{OLB}}$ signal. The $S^{\text{(E)}}_{\text{OLH}}$ signal is shown in Fig. 2.3(b1). Note that the presence of the ω_{ac} factor which reverses the sign under $a \to c$ relative to Eq. (2.11) rendering both red and blue contributions the same sign for a given T. The sign of $S^{(\mathrm{E})}_{\mathrm{OLH}}(T)$ then indicates whether the process is Stokes ($S^{(\mathrm{E})}(T) < 0$) or anti-Stokes ($S^{(\mathrm{E})}(T) > 0$). Energy conservation implies that the pulse energy change and the molecular energy change must have equal magnitude and opposite sign. In particular, the diagram in Fig. 2.1(a) assumes that, after preparation, the molecule is in the superposition of states a and c and the final state of the molecule after interacting with transmitted pulse is a population cc. Similarly using the permutation $a \leftrightarrow c$ one can end up in the final state aa. If the energy of state a is higher (lower) than that of c this is a Stokes (anti-Stokes) process.

2.1.2 Off-Resonant Signals Quadratic in the Probe

Quadratic signals, i.e., second-order in the probe intensity, are obtained by expanding Eqs. (2.2) to first-order yielding

$$S^{(\mathrm{fd})}_{\mathrm{OQ}}(\omega, T) = 2\Im i \int dt \int_{-\infty}^{t} dt' e^{i\omega(t-t_0)} \mathcal{E}^*(\omega)\mathcal{E}(t-t_0)|\mathcal{E}(t'-t_0)|^2 \times \{\langle \hat{\alpha}(t)\hat{\alpha}(t')\rangle - \langle \hat{\alpha}(t')\hat{\alpha}(t)\rangle\}, \tag{2.15}$$

$$S^{(\mathrm{E})}_{\mathrm{OQ}}(T) = 2\Im \int dt \int_{-\infty}^{t} dt' \dot{\mathcal{E}}^*(t-t_0)\mathcal{E}(t-t_0)|\mathcal{E}(t'-t_0)|^2 \times \{\langle \hat{\alpha}(t)\hat{\alpha}(t')\rangle - \langle \hat{\alpha}(t')\hat{\alpha}(t)\rangle\}, \tag{2.16}$$

where the two-point time correlation functions of the off-resonant polarizability $\hat{\alpha}^{(0)}$ can be expressed in terms of the density matrix

$$\langle \hat{\alpha}(t)\hat{\alpha}(t')\rangle = \mathrm{Tr}\,[e^{i\hat{H}_0(t-\tau_0)}\hat{\alpha}^{(0)}e^{-i\hat{H}_0(t-t')}\hat{\alpha}^{(0)}e^{-i\hat{H}_0(t'-\tau_0)}\rho(\tau_0)], \tag{2.17}$$

which we will use for general eigenstate expansions, or the wavefunction

$$\langle\hat{\alpha}(t)\hat{\alpha}(t')\rangle = \langle\psi(\tau_0)|e^{i\hat{H}_0(t-\tau_0)}\hat{\alpha}^{(0)}e^{-i\hat{H}_0(t-t')}\hat{\alpha}^{(0)}e^{-i\hat{H}_0(t'-\tau_0)}|\psi(\tau_0)\rangle \tag{2.18}$$

which is convenient for nuclear dynamics simulations.

Quadratic Broadband (QB) Probe

The frequency-dispersed quadratic signal (2.15) for a broadband probe expanded in eigenstates reads

$$\begin{aligned} S^{(\mathrm{fd})}_{\mathrm{OQB}}(\omega,T) = -2\int\frac{d\omega'}{2\pi}|\mathcal{E}(\omega)||\mathcal{E}(\omega')|\sum_{a,c,d}\alpha^{(0)}_{cd}\alpha^{(0)}_{da}|\rho_{ac}|\cos\phi_{ac}(T) \\ \times\left[|\mathcal{E}(\omega-\omega_{dc})|\mathcal{E}(\omega'+\omega_{da})| - |\mathcal{E}(\omega+\omega_{da})||\mathcal{E}(\omega'-\omega_{dc})|\right], \end{aligned} \tag{2.19}$$

where the first (second) term in the square brackets corresponds to the left (right) diagrams in Fig. 2.1(b). Equation (2.19) has a more complex dependence on the Raman shift ω_{ac} than the linear signal (2.11). The field envelopes are now shifted by the electronic transition frequencies ω_{ad} and ω_{dc} which yields difference $\omega_{dc}-\omega_{da} = \omega_{ac}$. The quadratic signal oscillates with a phase that depends on states d other than a and c that create the resonance and involves the phases of the polarizability $\hat{\alpha}^{(0)}$.

Comparing this to the corresponding linear signal (Eq. (2.11)) shows that a $\pi/2$ phase change. As a result, the fact that $\phi_{aa}(T) = 0$ no longer eliminates contributions from populations and they form a time-dependent background to all quadratic signals. Because the initial density matrix is assumed to be perturbative (so that the ground state dominates the populations) the contribution due to populations is primarily Stokes overall. Since the contribution due to the populations is Stokes and the oscillating coherences are too weak to overcome this, the overall process is Stokes at all times T (as illustrated in Fig. 2.2)(a2).

The energy change signal (Eq. 2.16) is given by

$$S^{(\mathrm{E})}_{\mathrm{OQB}}(T) = -\int \frac{d\omega}{2\pi} \int \frac{d\omega'}{2\pi} |\mathcal{E}(\omega)||\mathcal{E}(\omega')| \sum_{a,c,d} |\mathcal{E}(\omega+\omega_{da})||\mathcal{E}(\omega'-\omega_{dc})|$$
$$\times (\hbar\omega_{da}+\hbar\omega_{dc})|\rho_{ac}|\alpha^{(0)}_{cd}\alpha^{(0)}_{da}\cos\phi_{ac}(T). \tag{2.20}$$

Since the populations contribute a static off-set, there is now a strong zero-frequency peak in the Fourier transform of Eq. (2.20). Additionally, the peak heights are no longer as simply related to the α_{ac}, ρ_{ac} as in the linear case. In particular, since the peak heights are determined by a free summation over the intermediate state d, the terms in this sum can interfere constructively or destructively leading to enhanced or suppressed peaks (note that the $\omega_{ac} = 4$ eV peak is suppressed in Fig. 2.2)(c2).

Quadratic Hybrid (QH) Probe

Again expanding the quadratic frequency-dispersed transmission signal (2.15) in eigenstates but this time considering a hybrid field, we obtain

$$S^{(fd)}_{QH}(\omega-\omega_1,\omega_1,T) = -\frac{4\pi}{\hbar^2}|\mathcal{E}_0(\omega)||\mathcal{E}_1|^2 \sum_{a,c,d} \alpha^{(0)}_{da}\alpha^{(0)}_{cd}|\rho_{ac}|\cos\phi_{ac}(T)$$
$$\times \left[|\mathcal{E}_0(\omega_1+\omega_{da})|\delta(\omega-\omega_1-\omega_{dc}) - |\mathcal{E}_0(\omega_1-\omega_{dc})|\delta(\omega-\omega_1+\omega_{da})\right]. \tag{2.21}$$

As in the linear case, the narrowband pulse allows us to clearly resolve the transition peaks. Unlike the linear signal (2.13), the quadratic hybrid signal is independent of the phases of the narrowband and broadband pulses, ϕ_1 and ϕ_0, and is therefore observable without phase-controlled pulses. Just as in the broadband case, the signal is sensitive to populations which contribute a static Stokes spectrum. In Fig. 2.3(a2), we plot this signal for $\omega_1 = \omega_0$ as well as separate plots for the contributions due to populations and coherences.

Summary of Off-Resonant Stimulated Raman Techniques.		
Signal	$S^{(\mathrm{fd})}$	$S^{(\mathrm{E})}$
S_{OLB}	Eq. (2.11): Oscillatory gain/loss pattern shows Stokes/anti-Stokes oscillations in T.	Eq. (2.12): No spectral resolution due to ω integration. May visualize weak transitions due to weighting ω_{ac}.
S_{OLH}	Eq. (2.13): High spectral resolution compare to S_{OLB}. Each peak oscillates at it's frequency ω_{ac} and with phase ϕ^{ρ}_{ac}.	Eq. (2.14): Does not carry new information compared to $S^{(\mathrm{fd})}$.
S_{OQB}	Eq. (2.19): Always Stokes due to dominance of populations (which do not contribute to linear signals).	Eq. (2.20): Transition spectra can be achieved by Fourier transform over T.
S_{OQH}	Eq. (2.21): spectral and temporal resolutions are higher than S_{OLH} (not conjugated) but retrieval of frequencies and phases is more complicated.	Eq. (2.22): with Fourier transform over T can visualize weak transitions.

Table 2.1: Summary of off-resonant Stimulated Raman Techniques. The total photon number change $S^{(N)}$ vanishes at all orders.

To calculate the integrated signals we must also include contributions from diagrams whereby the last interaction is with narrowband pulse $\mathcal{E}_1$. The corresponding pulse energy change which includes both broadband and narrowband components is

$$\begin{aligned} S^{(E)}_{QH}(\omega_1, T) = -2|\mathcal{E}_1|^2 \sum_{a,c,d} \alpha^{(0)}_{cd} \alpha^{(0)}_{da} |\rho_{ac}| \cos\phi_{ac}(T) \\ \times [\omega_{dc}|\mathcal{E}_0(\omega_1+\omega_{dc})||\mathcal{E}_0(\omega_1+\omega_{da})| + \omega_{da}|\mathcal{E}_0(\omega_1-\omega_{da})||\mathcal{E}_0(\omega_1-\omega_{dc})|]. \end{aligned} \tag{2.22}$$

Note that in the quadratic case the energy flux involves also another state d in addition to states a and c, so the different fluxes corresponding to all relevant pairs of states should be added to get the overall energy change of the pulse.

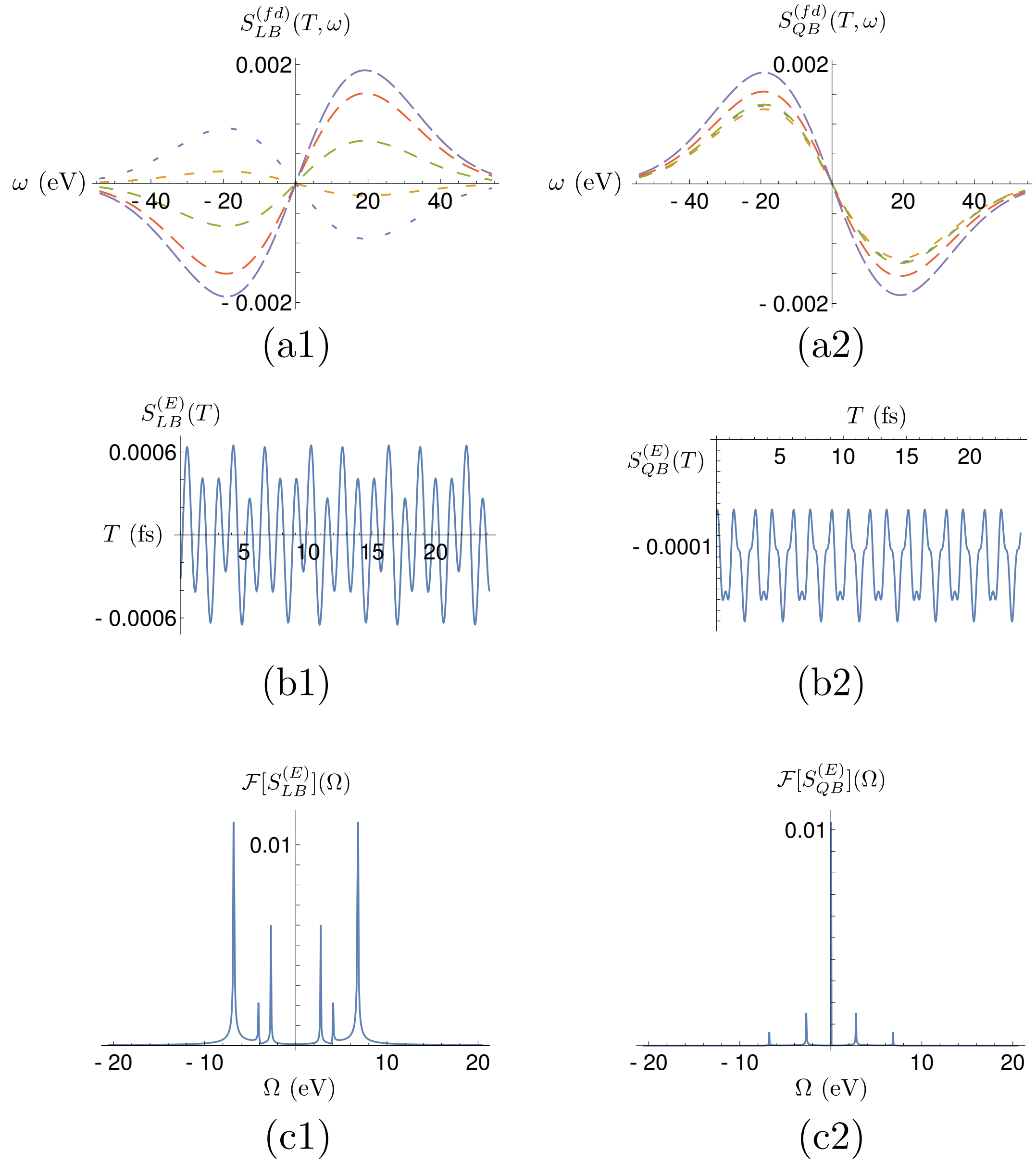

(a1) (a2)

(b1) (b2)

(c1) (c2)

Figure 2.2: (Color online) (a1) and (a2): Off-resonant linear and quadratic frequency-dispersed signals (Eqs. (2.11) and (2.19)) at various times T after state preparation (T advances in units of ∼60 attoseconds as the dashes lengthen). (b1) and (b2): Off-resonant linear and quadratic broadband energy signal as a function delay time T (Eqs. (2.12) and (2.20)). Note that the linear signal oscillates about zero but the quadratic signal has a static offset corresponding to the contribution from populations. (c1) and (c2): Fourier transforms of (b1) and (b2). In the linear case, peaks corresponding to all ω_{ca} coherences are visible. In the quadratic case, there is a large central peak at zero corresponding to the populations. In the quadratic signal, the states $c-a$ are coupled indirectly through a third state d and the summation over intermediate states can suppress or enhance the Raman peak magnitudes relative to their linear proportions.

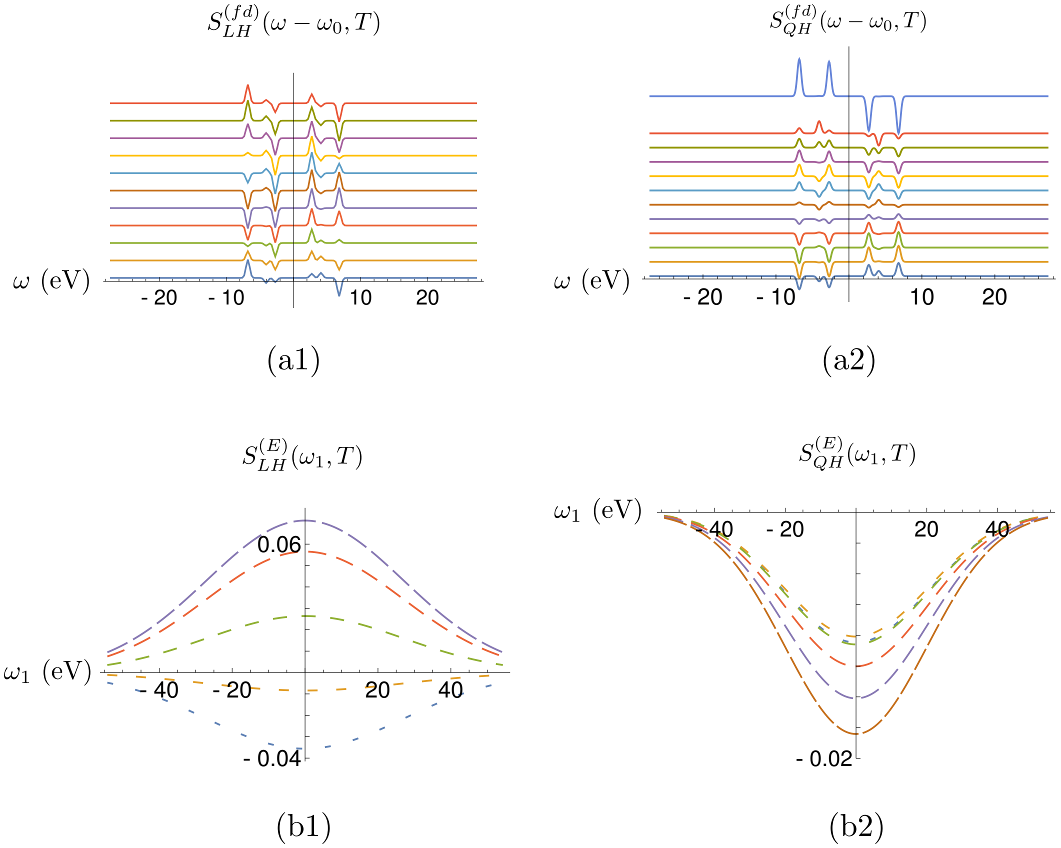

(a1)

(a2)

(b1)

(b2)

Figure 2.3: (a1) and (a2):Off-resonant linear and quadratic hybrid frequency-dispersed signals (Eqs. (2.13) and (2.21)) at various times T after state preparation (T advances in units of ∼60 attoseconds as one goes up the vertical axis). The quadratic signal is split into the static contribution due to populations (a2 top spectrum) and the time-dependent contribution due to coherences (a2 lower spectra). In contrast to the broadband signals, the narrowband pulse allows us to resolve the individual transition peaks. (b1) and (b2): Off-resonant linear and quadratic hybrid energy signals (Eqs. (2.14) and (2.22)) as a function of narrowband frequency ω_1 and delay time T (T advances in units of ∼60 attoseconds as the dashes lengthen). The broadband detection renders individual transition peaks unobservable and the result is similar to the broadband case (Eq. (2.22)) but symmetric (rather than anti-symmetric) about $\omega = \omega_0$. Note that $S_{QH}^{(E)}(T) < 0$ revealing that the quadratic process is always Stokes while the linear process oscillates between Stokes and anti-Stokes.

2.1.3 Discussion of Off-Resonant Signals

Having obtained eigenstate expressions for a variety of off-resonant Raman signals, we present example spectra calculated from a simple model consisting of a ground state and two valence excitations at $\varepsilon_{a(c)} \in \{0, 2.7, 6.8\}$ (eV). The polarizabilities α_{ac} are symmetric but otherwise random numbers of $\mathcal{O}(.1 - 1)$ and the ρ_{ac} are random but taken from a pure perturbative state (i.e., a state $|\psi\rangle$ in which the ground state amplitude is near unity in magnitude).

Figure 2.2 shows the linear and quadratic off-resonant broadband signals side-by-side. We do not plot $S^{(N)}$ since it vanishes in the off-resonant regime. For the frequency-dispersed signal (Eqs. (2.11), (2.13), (2.19), and (2.21)), the broadband detection makes discerning individual transitions impossible but nicely illustrates the Stokes/anti-Stokes oscillations in time. In the linear case, the red contributions are positive and the blue are negative at $T = 0$ so the process is Stokes at this time and oscillates with T. The quadratic detection is always Stokes due to the population contributions. The time-domain energy signal (Eqs. (2.12), (2.14), and (2.20), and (2.22)) confirms that the quadratic process is always Stokes while the linear process oscillates between Stokes and anti-Stokes. Transforming these signals reveals the ω_{ca} transitions (though the quadratic possesses a large $\Omega = 0$ peak due to populations that is of course missing from the linear signal).

For comparison, the linear and quadratic hybrid signals are shown in figure 2.3. The spectral resolution of the narrowband pulse gives sharp peaks at the $\omega - \omega_1 = \omega_{ac}$. In the linear case, each ω_{ac} peak is due to a term that oscillates with this same frequency. However, in the quadratic case, each oscillating term contains peaks at all different ω_{da}, ω_{dc} (as per Eq. (2.21)) and the phases of the peak oscillations do not as directly reveal the phases ϕ^{ρ}_{ac}. Note that the intermediate summation in the quadratic signal implies that peaks will be visible even for states not initially occupied (i.e, for which $\rho_{ac} = 0$) while the peaks observable in the linear signal are restricted to those initially occupied. Linear off-resonant signals therefore vanish for systems in their ground state and purely probe transient, excited-state phenomena.

In summary, $S^{(\mathrm{fd})}$ shows an oscillatory pattern of gain and loss features in the red and blue regimes that depend on the initial phase of ρ_{ac}. This information is integrated out in $S^{(\mathrm{E})}$ where the entire probe pulse envelope exhibits Stokes (loss) or anti-Stokes (gain) shifts periodically [33]. The broadband signals alone do not possess a sufficient resolution to directly observe the transition spectrum and only access to it through the Fourier transforms of the energy signals $S^{(\mathrm{E})}(T)$. Utilizing a hybrid broad-narrow pulse combined with frequency-dispersed detection allows high spectral and temporal resolution thus permitting spectral snapshots to be taken that clearly resolve all transitions and therefore permit extraction of the phases from the oscillation patterns. In the linear case, this requires control of the relative pulse phases (the phases cancel in the quadratic case). The quadratic and linear signals generally carry the same information about coherences but this is accessed without the background due to populations in the case of linear signals. One important caveat to this is that the magnitudes of the various transition peaks can be enhanced or suppressed by the interference of different pathways (characterized by the intermediate state d). Since each oscillation term contributes to multiple peaks through this intermediate state, a given peak ω_{ac} will not oscillate at the corresponding phase ϕ^{ρ}_{ac}, making retrieval of the wavepacket's phase more difficult in the quadratic case.

2.2 Resonant Stimulated Raman Techniques

The off-resonant techniques considered in section 2.1 conserve the number of probe photons. Photon energy gets redistributed among the broadband modes: $S^{(N)}$ vanishes while $S^{(\mathrm{E})}$ is finite. When the X-ray pulses are resonant with core transitions, true photon absorption can take place. This renders $S^{(N)}$ finite as well, revealing new matter information. In this regime, the field-matter interaction Hamiltonian may no longer be recast using a frequency-independent, off-resonant polarizability but should rather be described by a dipole interaction Hamiltonian as in Eq. (1.5). This interaction Hamiltonian is very general and leads to a variety of techniques, such as the photon echo, double quantum coherence, sum/difference frequency and harmonic generation, and general n-wave-mixing experiments. Our focus will be on obtaining the resonant analogues of the Raman signals discussed in the previous section and we will therefore keep only those terms in the expansion that correspond to diagrams of the form in Fig. 2.1. This and other complications, to be clarified later, prevent us from writing arbitrary-order expressions in the form of Eqs. (2.5)-(2.7) that specify only the resonant-Raman-type contributions in which we are interested. We will find that, under certain assumptions, these signals may be recast in terms of a frequency-dependent, resonant polarizability $\hat{\alpha}(\omega)$ that represents consecutive creation and annihilation of a core excitation. This will be accomplished by integrating over the time spent in the core excited state, thus combining the two core-valence transition dipole operators into an effective valence-valence x-ray polarizability.

2.2.1 Linear Probe

The frequency-dependent resonant analogue of Eq. (2.9) is

$$S_{\mathrm{RL}}^{(\mathrm{fd})}(\omega, T) = 2\Im i\mathcal{E}^*(\omega)\int dt e^{i\omega(t-t_0)}\int_{-\infty}^{t} dt'\mathcal{E}(t')\langle\hat{V}(t)\hat{V}(t')\rangle \tag{2.23}$$

while integrated photon number and pulse energy change are given by

$$S_{\mathrm{RL}}^{(N)}(T) = 2\Im\int dt\int_{-\infty}^{t} dt'\mathcal{E}^*(t)\mathcal{E}(t')\langle\hat{V}(t)\hat{V}(t')\rangle \tag{2.24}$$

and

$$S^{(\mathrm{E})}_{\mathrm{RL}}(T) = 2\Re \int dt \int_{-\infty}^{t} dt' \frac{d\mathcal{E}^*(t)}{dt_0} \mathcal{E}(t') \langle \hat{V}(t) \hat{V}(t') \rangle \tag{2.25}$$

respectively. Equation (2.23) is obtained by expanding Eq. (A.4) to first order in $\hat{H}_{\mathrm{I}}$ and keeping only the term analogous to Eq. (2.9). We have therefore omitted the contribution due to $\langle \hat{V}(t')\hat{V}(t)\rangle$. Throughout this thesis, it is our assumption that the pumped state contains no core excitations. Thus, the omitted term vanishes within the rotating wave approximation, since the dipole interaction at t corresponds to a photon emission event. Equation (2.23) therefore corresponds to transient absorption while the omitted term is stimulated valence-core emission.

Linear Broadband (LB) Probe

Expanding the frequency-dispersed transmission (2.23) as a sum over states and evaluating time integrals we obtain

$$S^{(\mathrm{fd})}_{\mathrm{RLB}}(\omega, T) = -2 \sum_{a,c} |\rho_{ac}| \left(\alpha_{ca}^{(\mathcal{E}\mathcal{E})'}(\omega) \sin\phi_{ac}(T) - \alpha_{ca}^{(\mathcal{E}\mathcal{E})''}(\omega) \cos\phi_{ac}(T) \right), \tag{2.26}$$

where $\Phi_{ac}(T) = \omega_{ac}T - \phi^{\rho}_{ac}$, α' and α'' represent the real and imaginary parts of the polarizability

$$\alpha_{ca}^{(jk)}(\omega) = \sum_{x} \frac{\tilde{\mathcal{E}}_j^*(\omega)\tilde{\mathcal{E}}_k(\omega+\omega_j-\omega_k+\omega_{ca})(\mathbf{e}_k\cdot V_{cx})(\mathbf{e}_j\cdot V_{xa})}{\omega+\omega_j-\omega_{xc}+i\Gamma_x}, \tag{2.27}$$

where ω_m, $m = j, k$ is the central frequency of the pulse given by $\mathcal{E}_m(t) = \int \frac{d\omega}{2\pi}\tilde{\mathcal{E}}_m(\omega)e^{i(\omega+\omega_m)t}$, where we redefined the frequency domain amplitude $\tilde{\mathcal{E}}_m(\omega)$ to be centered at zero frequency (for a Gaussian pulse with bandwidth σ_m, $\tilde{\mathcal{E}}_m(\omega) = \frac{1}{\sqrt{2\pi}\sigma_m}e^{-\frac{\omega^2}{2\sigma_m^2}}$), Γ_x is the inverse core excited state lifetime, which is assumed to be shorter than the valence excitations a and

c. Thus, the polarizability implicitly depends on the pulse parameters, such as its central frequency. For $j = k$, Eq. (2.27) reduces to the commonly used polarizability (see Eq. (5) of [34]). Note that in the off-resonant case the polarizability matrix elements are real and the second term in Eq. (2.26) vanishes and the Stokes and anti-Stokes components oscillate with opposite phase as seen in Section II. The integrated photon numbe signal (2.24) is

$$S^{(N)}_{\mathrm{RLB}}(T) = \frac{2}{\hbar^2}\sum_{a,c}|\rho_{ac}|\alpha^{(\mathcal{E}\mathcal{E})''}_{ca}\cos\phi_{ac}(T), \tag{2.28}$$

where the integrated polarizability is given by

$$\alpha^{(jk)}_{ca} = \int_{-\infty}^{\infty}\frac{d\omega}{2\pi}\alpha^{(jk)}_{ca}(\omega) \tag{2.29}$$

and we used the symmetry $\alpha^{(\mathcal{E}\mathcal{E})}_{\alpha\beta} = \alpha^{(\mathcal{E}\mathcal{E})}_{\beta\alpha}$. We first note that the signal is given by the imaginary part of the polarizability. Therefore, when the polarizability is real (as in the off-resonant case) the signal vanishes, which is consistent with our earlier results. Again, the Stokes ($\omega_{ac} > 0$) and anti-Stokes ($\omega_{ac} < 0$) components oscillate with an opposite phase. The energy change of the pulse signal (2.25) is given by

$$S^{(\mathrm{E})}_{\mathrm{RLB}}(T) = -\sum_{a,c}|\rho_{ac}|\left[\omega_{ac}\alpha^{(\mathcal{E}\mathcal{E})'}_{ca}\sin\phi_{ac}(T) - (\beta^{(\mathcal{E}\mathcal{E})''}_{ca} + \beta^{(\mathcal{E}\mathcal{E})''}_{ac})\cos\phi_{ac}(T)\right], \tag{2.30}$$

where the tensor β represents the first moment of the polarizability:

$$\beta^{(jk)}_{ca} = \int\frac{d\omega}{2\pi}(\omega + \omega_j)\alpha^{(jk)}_{ca}(\omega). \tag{2.31}$$

Unlike the photon number signal (2.28), the energy change (2.30) involves both the real part of the polarizability tensor and the imaginary part of its first moment. Equation (2.30) reduces to Eq. (2.12) in the off-resonant case, where the polarizability is real and the second term vanishes.

Linear Hybrid (LH) Probe

The frequency-dispersed transmission of the broadband pulse $\mathcal{E}(\omega)$ in the presence of the narrowband pulse $\mathcal{E}_1$ is given by

$$S_{\mathrm{RLH}}^{(\mathrm{fd})}(\omega-\omega_1,\omega_1,T) = -2\sum_{a,c}|\rho_{ac}|\left(\alpha_{ca}^{(01)'}(\omega)\sin\phi_{ac}(T) - \alpha_{ca}^{(01)''}(\omega)\cos\phi_{ac}(T)\right), \quad (2.32)$$

where the ω_1 dependence is now implicitly included in $\alpha_{ca}^{(01)}$ by setting $\tilde{\mathcal{E}}_1(\omega) = \tilde{\mathcal{E}}_1\delta(\omega)$. The integrated photon number for a shaped pulse has to be calculated differently than the broadband case. In particular, one has to take into account the photon number change in both the broadband and narrowband pulses. This yields

$$S_{\mathrm{RLH}}^{(N)}(\omega_1,T) = -2\sum_{a,c}|\rho_{ac}|\left([\alpha_{ca}^{(01)'} + \alpha_{ca}^{(10)'}]\sin\phi_{ac}(T) - [\alpha_{ca}^{(01)''} + \alpha_{ca}^{(10)''}]\cos\phi_{ac}(T)\right), \quad (2.33)$$

where the first (second) terms in each square bracket represents the last interaction with the broadband (narrowband) pulse. For the hybrid pulse, both α' and α'' contribute to the signal, thus providing additional molecular information than the simple broadband pulse. Furthermore, the form of the anti-Stokes and Stokes polarizabilities suggests that the signal depends exclusively on the phase difference between both broadband and narrowband fields $\phi_0 - \phi_1$ which provides an additional control knob. Note, that in general the hybrid polarizabilities $\alpha_{ac}^{(10)}$ are not symmetric under permutation of their indices. However in the limit when $\phi_0 = \phi_1$, we have $\alpha_{ac}^{(10)} = \alpha_{ca}^{(01)}$ and Eq. (2.33) yields

$$S_{\mathrm{RLH}}^{(N)}(\omega_1,T) = \frac{2}{\hbar^2}\sum_{a,c}|\rho_{ac}|[\alpha_{ca}^{(01)''} + \alpha_{ca}^{(10)''}]\cos\phi_{ac}(T). \quad (2.34)$$

Finally, the total pulse energy change (narrowband and broadband components) can be obtained similarly

$$S^{(\mathrm{E})}_{\mathrm{RLH}}(\omega_1,T) = -2\sum_{a,c}|\rho_{ac}|\left([\beta^{(01)'}_{ca}+\beta^{(10)'}_{ca}]\sin\phi_{ac}(T)-[\beta^{(01)''}_{ca}+\beta^{(10)''}_{ac}]\cos\phi_{ac}(T)\right). \tag{2.35}$$

2.2.2 Quadratic Probe

The diagrams for the quadratic signal are depicted in Fig. **??**(d). We read the signal from the diagrams in Hilbert space to obtain

$$S^{(\mathrm{fd})}_{\mathrm{RQ}}(\omega,T) = 2\Im\int dt\int_{-\infty}^{t}dt'\int dt_1\int_{-\infty}^{t_1}dt_1'\tilde{\mathcal{E}}^*(\omega)\mathcal{E}(t'-t_0)e^{i(\omega+\omega_0)(t-t_0)}$$
$$\times[\mathcal{E}^*(t_1-t_0)\mathcal{E}(t_1'-t_0)\langle\hat{V}(t)\hat{V}(t)\hat{V}(t_1)\hat{V}(t_1')\rangle+\mathcal{E}(t_1-t_0)\mathcal{E}^*(t_1'-t_0)\langle\hat{V}(t_1')\hat{V}(t_1)\hat{V}(t)\hat{V}(t')\rangle], \tag{2.36}$$

where the first (second) term in Eq. (2.36) represents the left (right) diagram in Fig. 2.1(d). Extension of the upper limit of dt_1 integration to ∞ follows from the assumption of a sufficiently short core-excitation lifetime or under the assumption that the (chronologically) first two interactions are temporally well-separated from the final two. This is the key assumption which permits the recasting of the quadratic resonant signals in terms of an effective polarizability in the form of Eq. (2.27). In the most general case, the upper limit of the dt_1 integration should be set at t' and t for the first and second terms above respectively, as can be seen from the diagrams. The corresponding photon number and energy change signals are given by Eqs. (2.2).

Quadratic Broadband (QB probe)

For a broadband pulse we expand the signal (2.36) in eigenstates which yields a compact formula

$$S^{(\mathrm{fd})}_{\mathrm{RQB}}(\omega, T) = -\Im 2i \sum_{a,c,d} [\alpha^{(\mathcal{E}\mathcal{E})}_{cd}(\omega)\alpha^{(\mathcal{E}\mathcal{E})}_{da} - \alpha^{(\mathcal{E}\mathcal{E})}_{da}(\omega)\alpha^{(\mathcal{E}\mathcal{E})*}_{dc}]\rho_{ac}(T), \tag{2.37}$$

where $\rho_{ac}(T) = |\rho_{ac}|e^{-i\phi_{ac}(T)}$. In the off-resonant case $\alpha'' = 0$ and Eq. (2.37) reduces to Eq. (2.19). The integrated photon number signal reads

$$S^{(N)}_{\mathrm{RQB}}(T) = -4 \sum_{a,c,d} |\rho_{ac}|\alpha^{(\mathcal{E}\mathcal{E})''}_{cd}[\alpha^{(\mathcal{E}\mathcal{E})'}_{da} \sin\phi_{ac}(T) - \alpha^{(\mathcal{E}\mathcal{E})''}_{da} \cos\phi_{ac}(T)], \tag{2.38}$$

which clearly vanishes in the off-resonant case when $\alpha'' = 0$. The total energy change of the pulse is given by

$$S^{(\mathrm{E})}_{\mathrm{RQB}}(T) = -\Im 2i \sum_{a,c,d} [\beta^{(\mathcal{E}\mathcal{E})}_{cd}\alpha^{(\mathcal{E}\mathcal{E})}_{da} - \beta^{(\mathcal{E}\mathcal{E})}_{da}\alpha^{(\mathcal{E}\mathcal{E})*}_{dc}]\rho_{ac}(T). \tag{2.39}$$

Quadratic Hybid (QH) probe

The frequency-dispersed transmission of the broadband component of a hybrid broad-narrow probe reads

$$S^{(\mathrm{fd})}_{\mathrm{RQH}}(\omega - \omega_1, \omega_1, T) = -\Im 2i \sum_{a,c,d} [\alpha^{(01)}_{cd}(\omega)\alpha^{(10)}_{da} - \alpha^{(01)}_{da}(\omega)\alpha^{(01)*}_{dc}]\rho_{ac}(T), \tag{2.40}$$

which is similar to Eqs. (9)-(10) of [35] for the model with zero linewidth of electronic states. The integrated photon number signal, which includes the change in both broadband

and narrowband fields, is

$$S^{(N)}_{\mathrm{RQH}}(\omega_1,T) = -\Im 2i \sum_{a,c,d} [\alpha^{(01)}_{cd}\alpha^{(10)}_{da} + \alpha^{(10)}_{cd}\alpha^{(01)}_{da} - \alpha^{(01)}_{da}\alpha^{(01)*}_{dc} - \alpha^{(10)}_{da}\alpha^{(10)*}_{dc}]\rho_{ac}(T) \quad (2.41)$$

and the energy change of the pulse is given by

$$S^{(\mathrm{E})}_{\mathrm{RQH}}(\omega_1,T) = -\Im 2i \sum_{a,c,d} [\beta^{(01)}_{cd}\alpha^{(10)}_{da} + \beta^{(10)}_{cd}\alpha^{(01)}_{da} - \beta^{(01)}_{da}\alpha^{(01)*}_{dc} - \beta^{(10)}_{da}\alpha^{(10)*}_{dc}]\rho_{ac}(T). \quad (2.42)$$

2.2.3 Discussion of Resonant Signals

For the simulations of the resonant signals, we extended the model used in the off-resonant case to include core states with energies $\varepsilon_{x(y)} \in \{136, 141.5, 149.5\}$ (eV). Figure 2.4 shows the resonant linear and quadratic broadband signals. The frequency-dispersed signals (a/b) contain the valence-core resonances but not the Raman (this is due to the lack of field resolution). However, the Raman transitions ω_{ac} are in the same region as the shifted valence-core transitions $\omega_{xa} - \omega_0$ so they appear similar. Since the ω_{xa} peaks can arise from any a, c pair in the summation, the phases ϕ^{ρ}_{ac} are not directly accessible as the phases of peak oscillations. Taking Fourier transform of the energy of photon number signals (c) and (d) gives peaks corresponding to the Raman transitions only since these are the oscillation frequencies. As in the off-resonant case, the linear and quadratic signals have different relative peak intensities controlled by the different forms of the coupling.

Figure 2.5 shows 2D spectra of the resonant linear (left column) and quadratic (right column) hybrid frequency-dispersed signals for populations only (top panels) and populations and coherences together at different times (remaining panels). As $\omega_1 - \omega_0$ varies, peaks corresponding to Raman transitions (ω_{ca}) move along diagonals forming resonant streaks. In contrast, the core transitions ω_{xa} do not vary with ω_1 and therefore, each transition forms a series of repeated vertical peaks where the ω_{xa} transition intersects the diagonal streaks.

The magnitude of these peaks then reveals the strength of the coupling between the core and Raman transitions. Note that the population contribution makes only a single diagonal streak in the linear case but results in all streaks in the quadratic case (this is due to the summation over the intermediate state d). For the linear signal, we can therefore identify each linear streak with a particular a, c pair in the summation and each streak will undergo Stokes/anti-Stokes oscillations at the respective phase $\Phi_{ac}(T)$, therefore allowing the retrieval of the phases ϕ^{ρ}_{ac}.

Figure 2.6 displays linear and quadratic hybrid energy and photon number signals. In both cases, the contribution due to populations is stronger than that from coherences. This is due to the resonant nature of the signal since the population contribution vanishes for linear off-resonant signals. Unlike in the off-resonant case, the signal contains sharp peaks due to the valence-core transitions but the same lack of field resolution prevents direct identification of the Raman transitions. These can however be obtained via the Fourier transform. Figure 2.7 shows the Fourier transform (magnitude) with respect to delay time T of the linear and quadratic photon number and energy signals. The quadratic is notably weaker but all four signals show the same basic pattern of $\omega_{xa} - \omega_0$ resonances along the y-axis and $\Omega = \omega_{ac}$ resonances along the x-axis.

2.3 Summary of Raman Signals

The above two sections present an account of off-resonant and resonant Raman spectroscopies in terms of the polarizability $\hat{\alpha}$, formed from the consecutive creation and annihilation of a core excitation.

We presented a systematic classification scheme applicable to spectroscopic techniques in which a nonstationary state's creation is well-seperated from it's detection (pump-probe style spectroscopies). In this scheme, a particular spectroscopic technique is specified by the choice of state preparation and detection procedures. We consider various detection procedures and examine what sort of information one may obtain and in what ways the signals considered differ. We demonstrated the various signals for a model consisting of a few valence and a few core states and calculated the frequency-dispersed, photon number, and energy change signals for both linear or quadratic field intensity scaling and broad or hybrid spectral field shapes.

There are two mechanisms whereby the photon modes can change their occupation numbers. A photon can either redistribute amongst the modes, swapping from one frequency to another as in Raman interactions or, alternatively, it can be absorbed or emitted by matter. The former process is governed by the real parts of the polarizabilities α (and β) while the latter is governed by the imaginary parts. In the off-resonant regime, only the redistributive mechanism is operative. In the resonant regime, both contribute and oscillate with different phases in delay time T (the redistributive being a Sine funcion and the absorbtive/emittive being a Cosine).

The spectrum of the nonstationary state (the energy levels of the occupied states), can be obtained by taking the Fourier transform of any of the time-dependent signals, resonant or off-resonant. The relative magnitude of the various peaks in these signals varies depending on the coupling constants for each signal. In the simpler, linear signals, the relative peak magnitudes are directly indicative of the product of the coherence ρ_{ac} and the polarizability α_{ac}, while in the quadratic case, there is an additional α and a free summation over the intermediate state. Using broadband pulses, we had to sacrifice the time resolution to obtain frequency resolution of the ω_{ac} transitions. This limitation was surpassed by using a shaped, hybrid pulse consisting of broad and narrowband components. The resultant frequency-dispersed signals naturally show the peaks at the ω_{ac} transitions which oscillate in time. In the linear case, each peak oscillates with its own phase $\omega_{ac}T+\phi^{\rho}_{ac}$, thus allowing determination of the phase induced by the state preparation process. This technique therefore exploits the simultaneous resolution of narrowband and detected frequencies combined with the time-resolution granted by the broadband pulse to obtain the phases of the electronic wavepacket. Without frequency-dispersed detection, one is left with the photon number and energy change signals. Even though they contain less information than the frequency dispersed hybrid signals, the resolution granted by the narrowband pulse allows one to access essentially the same information as the frequency dispersed broadband signal.

Finally, we note that the present formalism also applies to optical signals. X-ray signals allow one to probe valence excitations rather than vibrations. Furthermore, both the initial preparation and/or the preparation process can then be the product of an X-ray scattering, photoionization, or Auger process (as recently discussed in [36, 30]) in addition to an X-ray Raman process. The signals obtained by a Raman probe then detect both the amplitude and phase of the coherent superpositions of singly or doubly ionized states. These are signatures of many- body effects in the photoionization and the Auger processes.

Compared to previous work, here we present the most general systematic description of a series of x-ray Raman signals. Using abbreviations of the signals of the present paper in earlier work [21] $S_{\mathrm{QH}}^{(\mathrm{fd})}$, $S_{\mathrm{QB}}^{(N)}$, and partially $S_{\mathrm{QH}}^{(N)}$ signals. Using the present terminology, the signals studied in [37] are $S_{\mathrm{QH}}^{(\mathrm{fd})}$ and $S_{\mathrm{LH}}^{(\mathrm{fd})}$ while in [38], the $S_{\mathrm{QH}}^{(N)}$ signal was investigated.

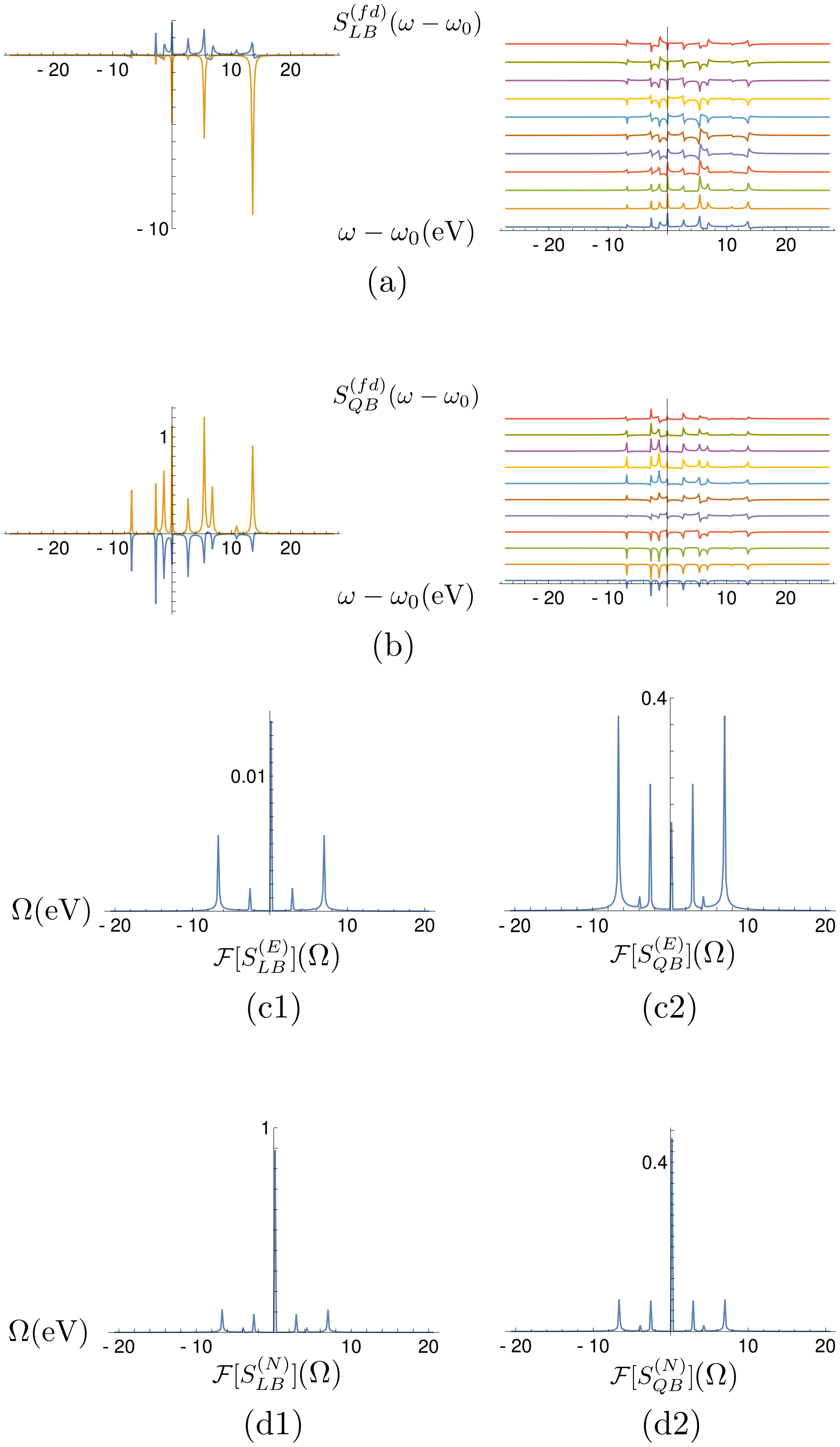

Figure 2.4: (Color online) (a): Resonant linear broadband frequency-dispersed signal for the populations (time-independent) and coherences at $T = 0$ (left) and time evolution of coherences (right). (b): Resonant quadratic broadband frequency-dispersed signal for the populations (time-independent) and coherences at $T = 0$ (left) and time evolution of coherences (right). For coherences in both (a) and (b), T advances in units of $\sim$60 attoseconds as one goes up the vertical axis. (c1) and (c2): Resonant linear (c1) and quadratic (c2) broadband energy signal Fourier transformed. (d1) and (d2): Resonant linear (d1) and quadratic (d2) broadband photon number signal Fourier transformed.

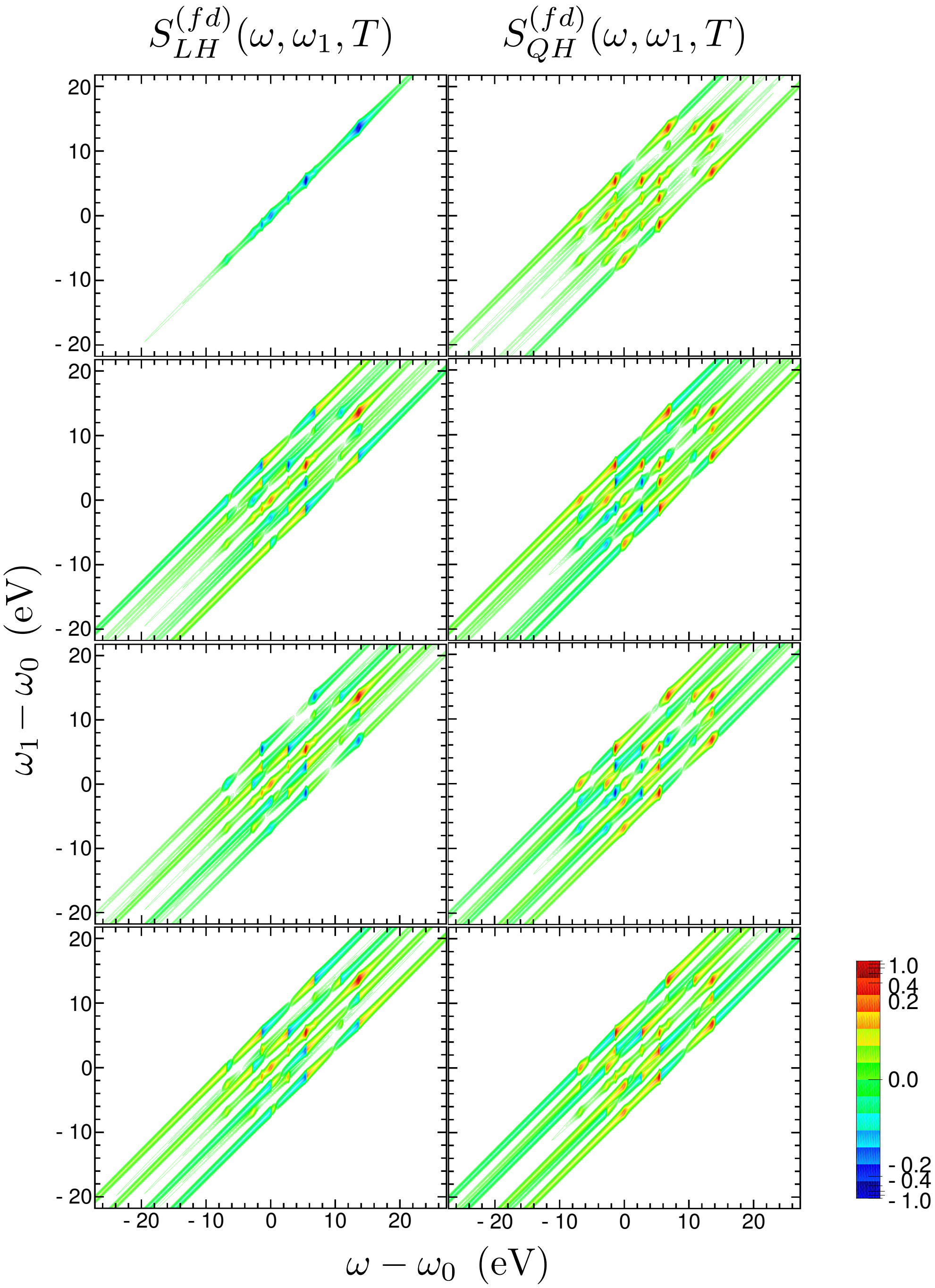

Figure 2.5: (Color online) Resonant linear (left column) and quadratic (right column) hybrid frequency-dispersed signals. The top of each column is the time-independent contribution due to populations. The second panel from the top is the total signal at $T = 0$ and the remaining two panels per column are for $T = 240$(as) and $T = 480$(as). This form of the signal allows one to disentangle valence-core (ω_{xa}) transitions from Raman (ω_{ca}) transitions.

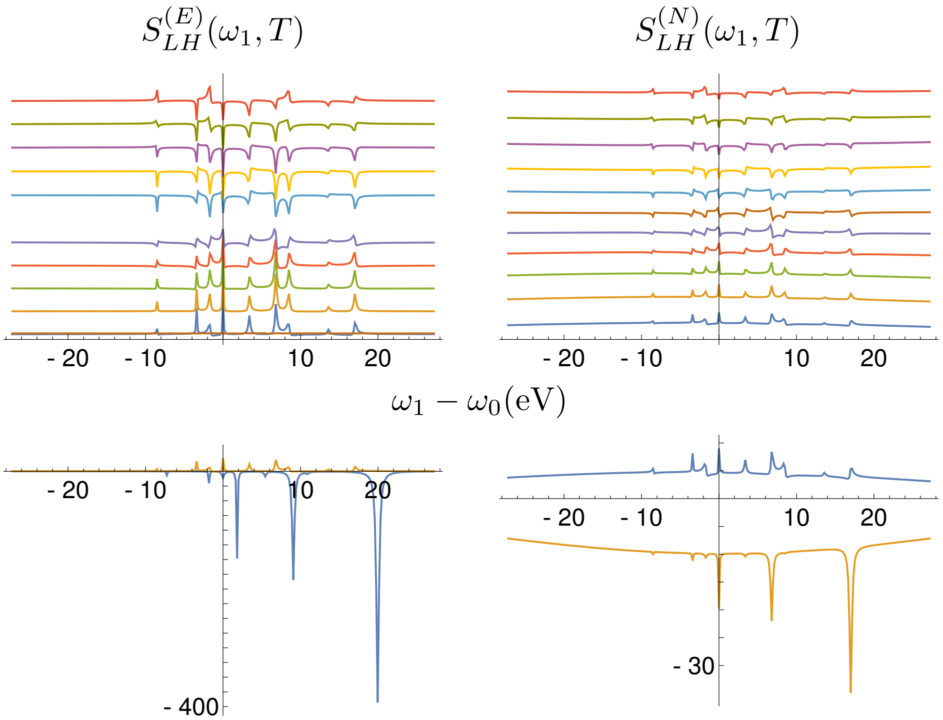

(a)

(b)

Figure 2.6: (Color online) (a): Resonant linear hybrid energy signal for coherences at multiple times T (top) and comparison of populations with initial coherences (bottom). (b): Resonant linear hybrid photon number signal for coherences at multiple times T (top) and comparison of populations with initial coherences (bottom). For time-dependence of coherences, T advances in units of ∼60 attoseconds as one goes up the vertical axis.

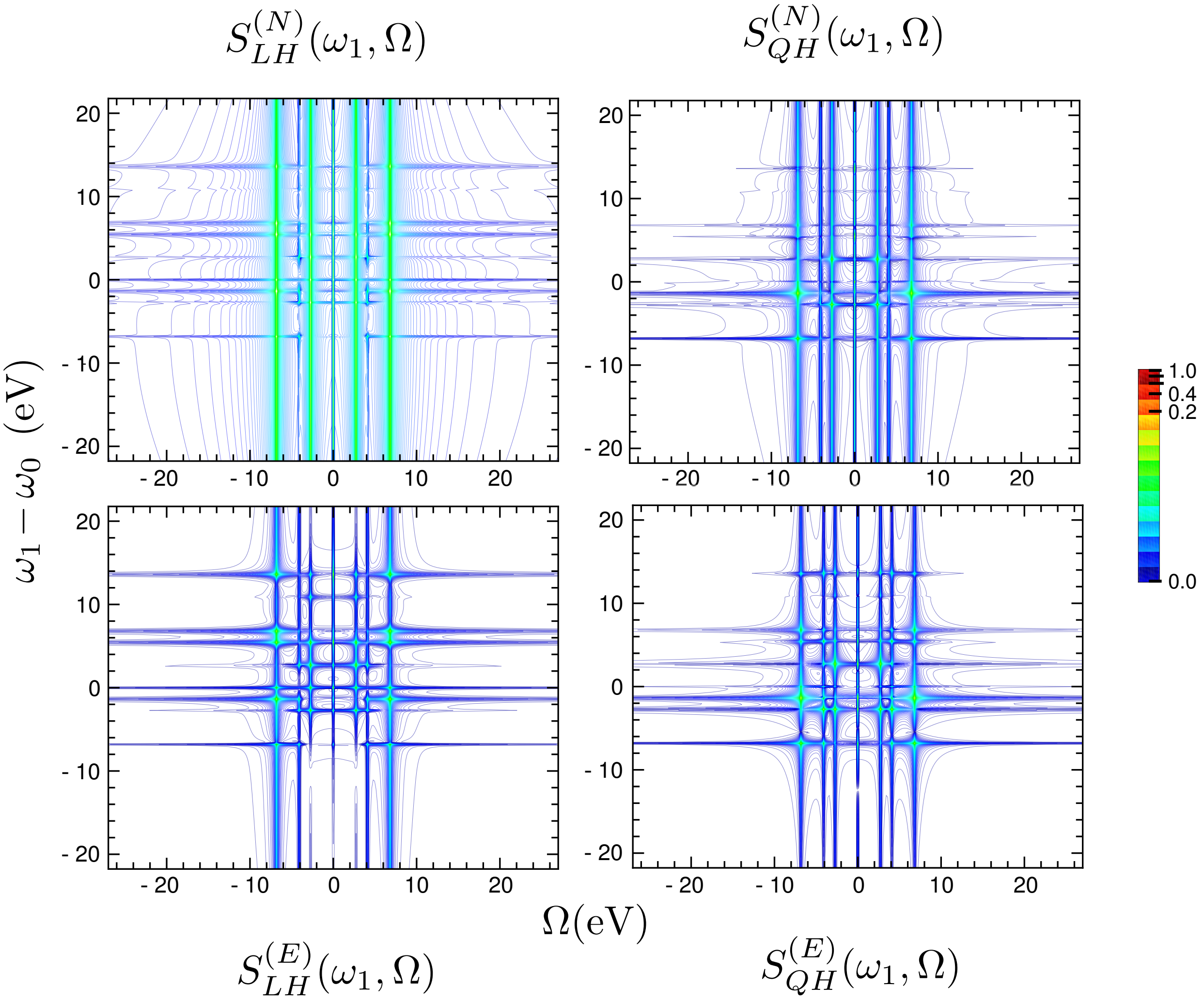

Figure 2.7: (Color online) (Resonant linear (left column) and quadratic (right column) hybrid photon number (top) and energy change (bottom) signals. These signals show Ω resonances at the Raman transitions ω_{ac} allowing their separation from the valence-core transitions ω_{xa}.

Chapter 3

Transient Redistribution of Ultrafast Electronic Coherences

The photochemistry of molecules is of considerable fundamental interest with direct impact on synthesis [39], chemical sensors [40], and biological processes [41, 42, 43, 44, 45]. As discussed in chapter 1, conical intersections of electronic states provide a fast, sub-100-femtosecond non-radiative pathway that controls product yields and rates in virtually all photochemical and photo-physical processes. At a CI, electronic and nuclear degrees of freedom become strongly coupled and the Born-Oppenheimer approximation, which allowed their separation, breaks down. Strong experimental evidence for CIs is based on the observation of fast conversion rates or other indirect signatures (e.g., suppression of vibrational absorption peaks [46]). However, their direct experimental observation has not been reported yet. The main obstacle is the rapidly decreasing electronic energy gap during the dynamics, requiring an unusual combination of temporal and spectral resolutions which is not available via conventional femtosecond optical and infrared experiments [41, 47, 48, 49].

We describe here a novel, background-free technique, recently proposed to directly and unambiguously monitor the passage through a CI by using recently-developed attosecond broadband X-ray sources (the contents of this chapter being largely taken from [50]). Available optical techniques monitor state populations [41, 49] or look for signatures in transient vibrational spectra to identify CIs [46, 48, 51, 52]. The technique looks directly at electronic Raman resonances created by the electronic coherence generated as the system passes through the CI and is not sensitive to electronic populations. The time-dependent energy splitting between the two adiabatic surfaces as well as the phase of the wave function can be directly read off the Raman shift between gain and loss features in the Stokes and anti-Stokes signals. Simulations demonstrate how this new method allows the precise timing of when and how a nuclear wave packet reaches and passes through the CI.

3.1 TRUECARS

Any direct measurement of CIs simultaneously requires ultra-fast time resolution and adequate spectral resolution in order to resolve the time dependent electronic energy gap. As the nuclei approach a CI from the vertical transition Franck-Condon point of an optical excitation (Fig. 3.1(a)), they acquire large velocities and the passage through the CI or a seam occurs in a few femtoseconds [53, 47, 54, 55]. With the ongoing development of free-electron lasers (FELs) [56, 57] and high-harmonic-generation (HHG) sources [58], (near transform limited) pulses in the extreme UV to soft X-ray region with a few femtoseconds and down to the attosecond durations and several-electron-volt bandwidth [59, 60, 61, 25, 23] become available. This makes it possible to directly probe CIs as we presently show.

The TRUECARS (Transient Redistribution of Ultrafast Electronic Coherences in Attosecond Raman Signals) technique proposed here is a novel extension of time-domain coherent anti-Stokes Raman spectroscopy (CARS) [62, 63, 33, 64], commonly used to probe vibrational coherence. In CARS, a pair of optical pulses generates a coherence between vibrational states

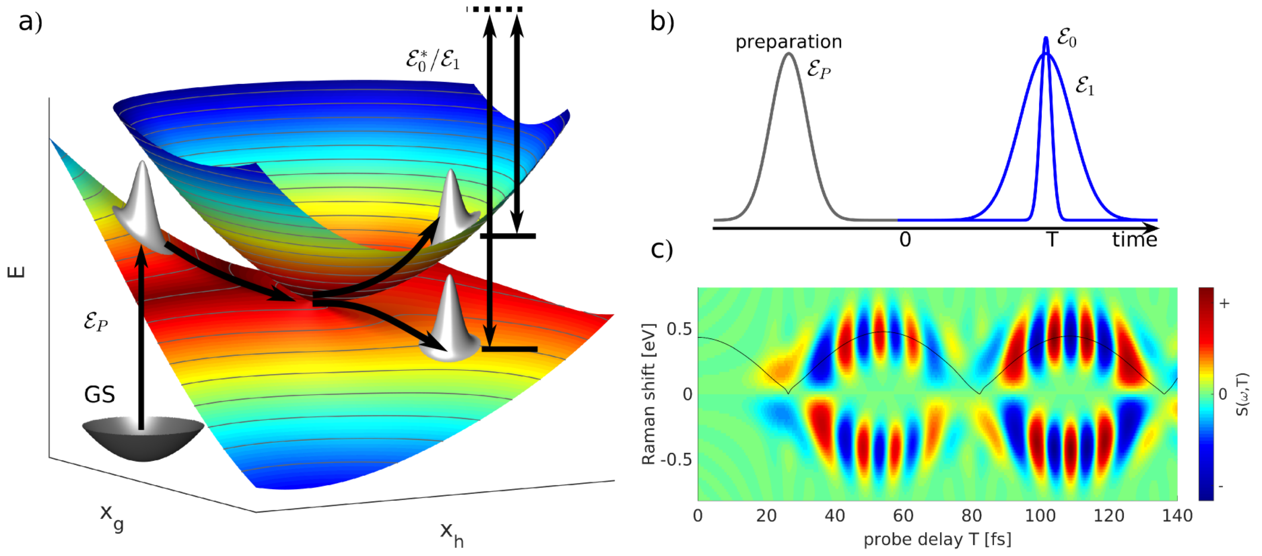

Figure 3.1: Schematic representation of the TRUECARS detection scheme. (a) A nuclear wave packet is promoted from the ground state (GS) by a pump-pulse $\mathcal{E}_P$ to an excited electronic state. As it passes the coupling region around the CI, a coherence is created between the two electronic states. The broadband $\mathcal{E}_0$/narrowband $\mathcal{E}_1$ hybrid pulse probes the electronic coherence between the nuclear wave packets on different surfaces. (b) Schematics of the pump and hybrid-probe pulse sequence. (c) Illustration of the signal calculated for a one-dimensional nuclear model. The energy splitting of the electronic states involved in the coherence (solid line) can be read from Raman shift.

which is subsequently detected via a Raman process induced by a second pair of pulses. The detected spectrum is displayed versus the time delay T between the two pairs of pulses, revealing the time-dependent vibrational coherence and its dephasing. The temporal and spectral resolution may be enhanced by taking the second pulse pair to be a hybrid pulse – a combination of a narrowband (picosecond) and a broadband (femtosecond) pulse which is known as hybrid CARS [65, 66].

The TRUECARS technique, sketched in Fig. 3.1, extends hybrid CARS in two important respects: (i) A combination of attosecond/femtosecond X-ray pulses is used to probe electronic coherence rather than conventional optical pulses that probe vibrational coherence. (ii) The coherence is not created directly by applied pulses as in CARS but is generated internally by the propagation through the CI following photoexcitation. A pump pulse first brings the molecule into an excited electronic state, preparing a non-stationary nuclear wave packet which then propagates towards the CI. The electronic coherence is not generated directly by the pulse but instead builds up during the time-evolution of the wave packet as it approaches the vicinity of the CI where the non-adiabatic intersurface coupling is present. A hybrid broadband/narrowband X-ray pulse then probes this electronic coherence by the time-resolved gain and loss of the positive and negative stimulated Raman components (see Fig. 3.1(b) for depictions of the pulse sequence). Resolving the entire spectrum of electronic Raman transitions (Fig. 3.1(c)) requires pulses with a few-electronvolt bandwidth and observing the CI dynamics requires pulses with a duration on the order of few femtoseconds or less.

As the technique is off-resonant, the molecule is coupled to the intensity of the off-resonant probing fields via the electronic polarizability operator $\hat{\alpha}$ and the matter-probe interaction Hamiltonian is

$$\hat{H}_{\mathrm{I}}(t) = \hat{\alpha}(t)|\mathcal{E}_0(t) + \mathcal{E}_1(t)|^2 \tag{3.1}$$

where $\mathcal{E}_0$ and $\mathcal{E}_1$ are the attosecond (broadband) and femtosecond (narrowband) components respectively of the probing field. The off-resonant electronic polarizability $\hat{\alpha}$ is the transition polarizability describing the Raman transitions between valence states. We do not include the photo-ionization processes in the simulations. It has been experimentally shown that X-ray Raman signals can successfully compete with the ionization background [29, 67]. To simplify the analysis, we assume both components to have the same carrier frequency ω_1. The TRUECARS signal is defined as the frequency-dispersed photon number change of the attosecond field and is given by

$$S(\omega, T) = 2\Im \int_{-\infty}^{+\infty} \mathrm{d}t \, e^{i\omega(t-T)} \mathcal{E}_0^*(\omega) \mathcal{E}_1(t-T) \times \langle \psi(t) | \hat{\alpha} | \psi(t) \rangle \tag{3.2}$$

where T is the time-delay between the probe field and the preparation pulse and $|\psi(t)\rangle$ is the total (nuclear and electronic) wavefunction. The probing fields are assumed to be temporally well-separated from the preparation process. The signal carries a phase factor $e^{i(\phi_1 - \phi_0)}$, where ϕ_i is the phase of the field $\mathcal{E}_i$. This factor causes the signal to vanish when averaged over random pulse phases; observation of TRUECARS therefore requires control of the relative pulse phases. Note that terms corresponding to electronic populations do not contribute since they carry no dynamical phase and vanish when taking the imaginary part in Eq. (3.2). TRUECARS therefore provides a background-free measurement of electronic coherence. It is also important to note that, due to the frequency-dispersion of the broadband pulse $\mathcal{E}_0(\omega)$, the field-matter interaction time is limited by the $\mathcal{E}_1$ pulse envelope. The temporal and spectral resolutions of the technique are not independent but are Fourier-conjugate pairs, both determined by the corresponding temporal and spectral profiles of $\mathcal{E}_1$. In order to resolve the changing energy gap along the CI, $\mathcal{E}_1$ must be shorter than the dynamics while spectrally narrower than any relevant energy splitting. For example, resolving a 0.1 eV energy difference implies at least a 6.5 fs pulse duration so dynamics faster than this will not be resolved.

The pulse configuration in TRUECARS is similar to transient absorption. The difference, besides the phase-matching requirement, is that the probe pulse is not resonant with any material transitions and is therefore not absorbed. Instead, there is an oscillatory redistribution of intensity between loss (positive Stokes/negative anti-Stokes) and gain (positive anti-Stokes/negative Stokes) that can affect the frequency-resolved transient intensity. The signal is linear in the probe intensity $\mathcal{E}_0\mathcal{E}_1$. Stimulated Raman spectroscopy (SRS) [68, 69, 70, 71, 72] uses the same pulse sequence but detects the quadratic signal $\mathcal{E}_0^2\mathcal{E}_1^2$. TRUECARS is therefore phase dependent whereas SRS is phase independent. The quadratic signal would allow greater resolution, since temporal and spectral resolution could then be set by the broadband and narrowband pulses respectively and would not be Fourier limited [69]. However, the quadratic signal is typically dominated by contributions stemming from electronic populations [73] and it is not therefore a background-free measurement of the electronic coherence. The linear TRUECARS signal is therefore a much cleaner way to measure the passage through a conical intersection.

Qualitative understanding of the TRUECARS signal can be facilitated by a semi-classical picture. We expand the electronic wave function in the adiabatic basis and assume that the nuclei follow the classical equations of motion:

$$|\psi(t)\rangle = \sum_a c_a(t) e^{-i\int_{-\infty}^{t} \varepsilon_a(\tau)d\tau} |a(t)\rangle \tag{3.3}$$

where the instantaneous states $|a(t)\rangle$ and energies $\varepsilon_a(t)$ vary with time through their dependence on the nuclei while the coefficients $c_a(t)$ vary due to the non-adiabatic coupling between the electronic surfaces near CIs. The coherence between the surfaces thus propagates with a time-dependent dynamical phase which generates oscillations in T with evolving period and frequency (ω_r). The energy splitting between the electronic states can thus be read not only from ω_r but also from the oscillation period in T (as can be seen by inserting Eq. (3.3) into (3.2)).

To clearly point out the unique features of the TRUECARS signal, Fig. 3.1(c) shows a simulation of a single vibrational mode with a long electronic coherence time. The model is constructed from two electronic states, which are represented by two displaced harmonic potentials and a Gaussian diabatic coupling. This model can represent, e.g., a simple diatomic molecule with an avoided crossing. A full quantum dynamical wave packet calculation is carried out on a numerical grid with a displaced Gaussian wave packet as initial condition and the TRUECARS spectrum is calculated according to eq. 3.2. In the absence of electronic coherence, the signal vanishes (this is the case in the beginning of the dynamics, Fig. 3.1(c)). As the wave packet approaches the non-adiabatic coupling region, an electronic coherence builds up and the signal appears. After it has passed the intersection, the splitting between the states increases again. The signal shows an oscillation of gain and loss features in the Stokes and anti-Stokes regime. The energy splitting (solid line) can be read directly from the Raman shift $\omega_r = \omega - \omega_1$. The broadening of the signal in ω_r is caused by the non-vanishing width of the nuclear wave packet, which covers a range of finite width of the potential energy surface. The signal builds up on both red- ($\omega_r < 0$) and blue- ($\omega_r > 0$) sides of the spectrum, appearing as two oscillating peaks. When the red side is positive and the blue side negative, the energy flows from the pulse to the molecule and the process is of Stokes type while opposite conditions yield an anti-Stokes process. The interaction with the molecule thus redistributes the field photons, either shifting the probe pulse toward the red or the blue side of the spectrum, but the total number of photons is conserved [31]. This is due to the off-resonant nature of the Raman probe used here (there is no absorption or stimulated emission) and is the origin of the 'Redistribution' in TRUECARS. This also leads to the absence of a Rayleigh peak at $\omega_r = 0$, which would come from electronic populations, making the signal background-free (induced only by electronic coherences). The signal oscillates with time T back and forth between Stokes and anti-Stokes and the oscillation period corresponds to the coherence period (the oscillations speed up and the positions of the peaks in frequency spread apart mirroring the separation of potential energy surfaces). The oscillation period

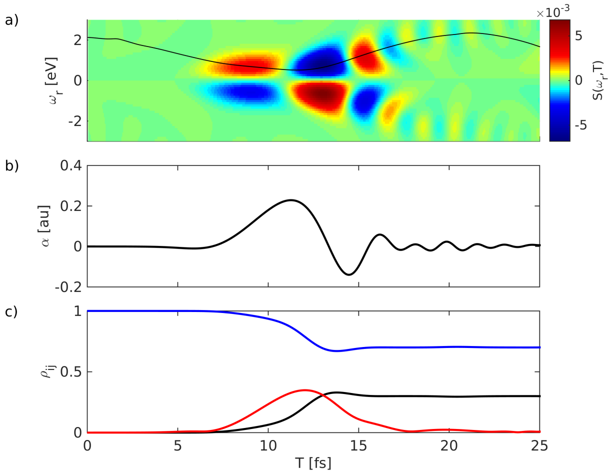

Figure 3.2: (a) Simulated TRUECARS Signal (Eq. 3.2) for the two-dimensional nuclear model with a pulse length of 1.2 fs ($\mathcal{E}_1$). The solid line indicates the average splitting of the potential energy surfaces. (b) The time dependent expectation value of the polarizability. (c) Elements of the reduced density matrix of the electronic subsystem. Blue and black: populations of the adiabatic S_2 and S_1 state respectively. Red line: the magnitude of the electronic coherence.

in T therefore also reveals the separation of adiabatic potential energy surfaces, while the magnitude of the signal envelope reveals the decay of the electronic coherence.

3.2 Simulations and Discussion

We now demonstrate the power of TRUECARS by wave packet simulation on a more realistic model system with two vibrational modes and two electronic states S_1 and S_2 and typical molecular parameters (depicted schematically in Fig. 3.1(a)). This is the minimal model required to describe a CI [74]. The two coordinates resemble the branching space of a CI and are displacements along the derivative coupling vector x_h and the gradient difference vector x_g. The initial condition is at the Franck-Condon point, chosen to be in the vicinity of the CI to allow the wave packet to reach the CI in a short period of time. Examples of molecules with ultrafast non-adiabatic dynamics include cyclohexadiene [75], ethylene [53], pyrazine [76], and DMABN [55]. The wave packet simulations are carried out numerically on a grid in the electronic and nuclear space using the diabatic basis and are transformed into the adiabatic basis as needed. The details of the calculations are given in the SI.

The molecule is assumed to be initially in its electronic ground state (S_0). An actintic pump-pulse creates an excitation in the S_2 state, thus launching the dynamics. The diabatic coupling vanishes in the Franck-Condon region to allow for an initial condition in which the Born-Oppenheimer approximation holds. The initial S_1/S_2 splitting at the Franck-Condon point is around 2 eV. The wave packet propagates freely on the S_2 surface in the branching space and approaches the CI. The resulting TRUECARS signal (Eq. 3.2) and the averaged time-dependent energy splitting is shown in Fig. 3.2(a) (solid line). The qualitative features are similar to the signal from the diatomic model shown in Fig. 3.1(c). The prepared state contains no electronic coherence and the signal turns on at around 2 fs, when the system approaches the non-adiabatic coupling region. The corresponding molecular property governing the signal, the off-resonant transition polarizability $\alpha(t)$, is shown in Fig. 3.2(b). If the $\hat{\alpha}$ is assumed to be independent of the nuclear coordinates, $\alpha(t)$ is directly proportional to the real part of the electronic coherence. In Fig. 3.2(c), the adiabatic populations are shown along with the magnitude of the electronic coherence. After the wave packet has passed the CI at around 6 fs, it travels through a coordinate region where there is a small but finite splitting between adiabatic potential energy surfaces. The signal broadening stems from two contributions: The width of the nuclear wave packet, covering a certain range of potential energy differences, and the spectral width of the probe pulse. The peak maxima are slightly shifted to larger Raman shifts due to the fact the signal vanishes at $\omega_r = 0$ (an effect that is more pronounced for smaller ω_r as is seen for $T <$ 12fs in Fig. 3.2(a)). Additionally the information about the energy splitting is also contained in the oscillations in T, indicating that the system is in close vicinity of the CI, as the oscillation frequency is lowered . At around 15 fs, the energy splitting increases again as can be seen from ω_r. Since the S_1 and S_2 states have different gradients, the overlap between the nuclear wave packets $\langle\Psi_1|\Psi_2\rangle$ decays and the signal fades out. As can be seen in Fig. 3.2, the passage through the CI happens in less than 12 fs. By utilizing 1.2 fs pulses, the wave packet's arrival at the CoIn can be timed stroboscopically to within 10 fs. Note that an even shorter coherence lifetime would not allow for a clear determination of the energy splitting, but would increase the time resolution. As is clear from the overlay of the energy splitting on the TRUECARS spectra, the technique is capable of mapping out the potential energy surfaces of the reaction coordinate near the CI. It thus gives both dynamical information on the temporal and spectral profile of the the CI by providing information about period of oscillations as well as the phase of the electronic coherences near the CI. TRUECARS might also be useful to measure the Berry phase [77], which so far has elluded detection in chemical systems.

In summary, in this chapter we have discussed a resently-proposed spectroscopic technique (TRUECARS) that can directly monitor passage through conical intersections. The technique measures the frequency-resolved stimulated Raman scattering of a probe pulse as a function of the time delay T with respect to the pump pulse. In contrast to most other methods, TRUECARS is only sensitive to electronic coherences and populations do not contribute, making it uniquely suited to probing passage through CIs by capturing the electronic coherences generated by non-adiabatic couplings in the CI vicinity. We simulated the signal for 1D and 2D vibrational model systems and demonstrated that TRUECARS with attosecond pulses can be used to measure the time-varying energy gap between two electronic states. The rapidly decreasing energy gap around the CI is fully visible in the time resolved spectrum The decay of the electronic coherences contains information about the difference of the gradients between the electronic states, giving a hint about the geometry of the CI. The primary limitation to this technique is that decoherence will eventually eliminate the signa and the technique is most useful when the CI is in close proximity to the Franck-Condon point. This makes TRUECARS an ideal tool to investigate ultra-fast, photophysical system dynamics. The experimental parameters required – broadband sub-femtosecond pulses of $\sim$ 100eV or more and spectral widths of several eV – could be realized in the near future from state of the art free-electron laser sources [57, 78].

Chapter 4

Transient Photoelectron Spectroscopy

Photoelectron spectroscopy [79] (PES), in which the kinetic energy of electrons liberated from a sample via interaction with light is measured, has long been utilized to gain knowledge of the level-structure of molecules and materials. Energy conservation implies that the photoelectron energy is indicative of the difference between the frequency of ionizing radiation and the ionization potential of the material. More recently, the technique has been extended to the time-domain. In time-resolved photoelectron spectroscopy [80] (TRPES), a pump pulse prepares the molecule in a nonstationary state, the dynamics of which are subsequently tracked by varying the delay time (labeled t_d in this chapter and in appendix B to avoid confusion with the nuclear kinetic energy operator $\hat{T}$) between the pumping pulse and a subsequent ionizing XUV or x-ray pulse, the detected quantity being the energy-resolved (or energy integrated) photoelectron yield. With the advent of ultrashort pulses, such experiments are able to achieve femtosecond resolution of excited state dynamics, allowing one to stroboscopically track ultrafast photochemical processes and nuclear dynamics.

Special attention has been drawn to the non-adiabatic dynamics through CIs due to their broad impact on photochemical and even photobiological processes [41, 42, 43, 44, 45]. CIs provide ultrafast, non-radiative decay pathways which influence product yields and reaction rates in virtually all photochemical processes. Near a CI, the nuclear and electronic degrees of freedom become strongly coupled and the Born-Oppenheimer approximation (BOA), which is based on the separation of electronic and nuclear frequencies, breaks down [81, 82]. The passage through a CI can be detected by vibrational spectroscopic signatures [52, 46, 48, 51], fast population dynamics [41, 49], and TRPES [83, 84]. However, with shorter pulses in the attosecond regime available, measuring [85] and even controlling the electronic dynamics [86] becomes possible. With the increasing availability of ultrashort pulses from high harmonic generation sources [56, 57] and free electron lasers [58], novel techniques based on a direct measurement of the electronic coherence become feasible [87, 88].

As we saw in the previous chapter, nuclear coupling in the CI-region transfers population between the electronic states while also generating coherences between them. In this chapter, we show that TRPES with sub-femtosecond pulses can be utilized to detect the electronic coherence created by the non-BOA coupling encountered by a nuclear wavepacket as it passes through the region of a CI. Multimode wave packet simulations of the TRPES of pyrazine [89, 90] show that the time dependence is essentially an overlay of electronic population with coherent nuclear dynamics, the latter of which produces oscillations at nuclear frequencies. This result can be well-understood from the perspective of a semiclassical Fermi Golden Rule (scFGR, Eq. (4.4)) in which the contributions from the various adiabatic electronic surfaces add incoherently, weighted by their time-dependent populations. The scFGR is intuitive and frequently employed to simulate and interpret spectra [84, 83, 91]. The scFGR is applicable in the BOA, where the electronic states do not couple. We show that electronic coherences created at CIs result in oscillations in the signal intensity that are missed in the standard scFGR expressions. Under certain conditions, the period of these oscillations is indicative of the average energy separation between the neutral electronic potential surfaces. This is similar to TRUECARS in that we access the transient spectral information temporally. This effect has been reported form experiments in the NO molecule [92], which showed sub-picosecond oscillations. New sub-fs light XUV and x-ray light sources can access the appropriate time-domain to observe this effect in polyatomic molecules with larger energy separations.

The focus of this chapter is to demonstrate the signatures of electronic coherence on photoelectron signals generated by sub-femtosecond pulses. We provide a novel formalism, which allows for inclusion of the electronic coherences and show how well effects are reproduced by the various simulation protocols with model systems. In section 4.1, we describe the model and the semi-classical Fermi golden rule for TRPES. In section 4.2, we obtain an exact correlation-function expression for the signal as well as a corresponding exact FGR, written as an expansion in the eigenbasis. From these exact expressions, we then rigorously derive the scFGR in section 4.3 by making the quasi-static approximation. In the process we obtain, an additional class of terms, arising from the electronic coherences. We discuss under what conditions these terms must be accounted for and what information they carry. In sections 4.4 and 4.5, we compare the features of the different levels of approximation using simulations for model systems. The content of this chapter is largely taken from Ref. [93].

4.1 Fermi's Golden Rule for TRPES

We describe TRPES with a Hamiltonian of the form discussed in [36], which neglects the interaction between the ionized molecule and the photoelectron. We work in the adiabatic basis and consider a set of neutral electronic states (labeled by a, b as they will generally be valence excitations) and ionized electronic states (labeled by α). In contrast to Eq. (1.2), we have no need to consider the Hamiltonian of the field and everything will be done semiclassically from the start. However, do must introduce a continuum of photoelectron states into which the system may emit. We therefore write the total Hamiltonian as

$$\hat{H} = \hat{H}_{\mathrm{M}} + \hat{H}_{\mathbf{p}} + \hat{H}_{\mathrm{x}}(t)\,. \tag{4.1}$$

where the molecular Hamiltonian is given by Eq. (1.3), nonadiabatic couplings between ionized states being ignored. Following Ref. [36], we utilize a second-quantized description of the photoelectron states and a first-quantized description of the bound states. This facilitates our treatment of PES in analogy with spontaneous light emission and the inclusion of molecule-photoelectron interactions (the latter are beyond the scope of this thesis and not included in our model). We take the photoelectron states to be independent of the nuclei and assume they do not interact with the ion (justified for sufficiently high-energy photoelectrons) and therefore write

$$\hat{H}_{\mathbf{p}} = \sum_{\mathbf{p}} \varepsilon_{\mathbf{p}} \hat{c}_{\mathbf{p}}^{\dagger} \hat{c}_{\mathbf{p}}, \tag{4.2}$$

for the photoelectron Hamiltonian ($\hat{c}_{\mathbf{p}}^{\dagger}, \hat{c}_{\mathbf{p}}$ are Fermi creation/annihilation operators for free photoelectrons with energy $\varepsilon_{\mathbf{p}}$). Note that the formalism can be straight-forwardly applied to photo detachment [94] as well, which only differs in the initial and final states (anion to neutral).

We work in the direct product space of bound (molecular) and continuum (photoelectron) states and the interaction with the photoionizing x-ray pulse is then written as

$$\hat{H}_{\mathrm{x}}(t) = -E_{\mathrm{x}}(t) \sum_{\mathbf{p}\alpha a} \hat{\mu}_{\mathbf{p}\alpha,a} \hat{c}_{\mathbf{p}}^{\dagger} |\alpha\rangle\langle a| + \hat{\mu}_{\mathbf{p}\alpha,a}^{\dagger} \hat{c}_{\mathbf{p}}^{\dagger} |a\rangle\langle\alpha|, \tag{4.3}$$

where $E_{\mathrm{x}}(t)$ is the ionizing x-ray pulse envelope and we neglect possible core excitations of the type discussed in chapters 2-3. The electronic matrix elements of the transition dipole remain operators in the nuclear space, as indicated by the circumflex. For simplicity, we assume that $\hat{\mu}$ is independent of the momentum $\mathbf{p}$, which is a reasonable approximation for fast photoelectrons [95], but not for slow electrons which do interact with the ion.

The photoelectron spectrum obtained via ionization by an x-ray pulse with frequency ω_{x} and pump-probe delay time t_{d} (relative to the pump) is most commonly simulated using the scFGR[84]

$$S_{\mathrm{sc}}(\varepsilon_{\mathbf{p}}, t_{\mathrm{d}}) = \int d\omega_{\mathrm{x}} |E_{\mathrm{x}}(\omega_{\mathrm{x}})|^2 S_{\mathrm{scFGR},0}(\varepsilon_{\mathbf{p}}, t_{\mathrm{d}}, \omega_{\mathrm{x}}) \tag{4.4}$$

$$S_{\mathrm{sc},0}(\varepsilon_{\mathbf{p}}, t_{\mathrm{d}}, \omega_{\mathrm{x}}) = \sum_{a\alpha} \langle |\mu_{\alpha a}\left(\mathbf{q}(t_{\mathrm{d}})\right)|^2 \rho_{aa}\left(\mathbf{q}(t_{\mathrm{d}})\right) \delta(\varepsilon_{\mathbf{p}} - \omega_{\mathrm{x}} + \varepsilon_{\alpha}\left(\mathbf{q}(t_{\mathrm{d}})\right) - \varepsilon_{a}\left(\mathbf{q}(t_{\mathrm{d}})\right))\rangle ,$$

where $\mathbf{q}(t)$ is the time-dependent set of nuclear coordinates (now written explicitly since they are computed classically) and $\langle \dots \rangle$ indicates an averaging over these coordinates. This averaging can be done at various levels of theory (ab-initio multiple spawning [96], surface hopping [97], etc.). Below, we will derive a fully quantum-mechanical version of the scFGR, in which the averaging comes as expectation values taken over the time-dependent nuclear wave function. This derivation will clarify the origin and applicability regime of Eq. (4.4) while naturally generating additional terms proportional to the electronic coherence ρ_{ab}. Note that Eq. (4.4) only contains terms proportional to the populations ρ_{aa}. Note also that the signal is dependent on the power spectrum of the ionizing x-ray pulse $|E_{\mathrm{x}}(\omega)|^2$. In contrast, the coherence terms appear with $E_{\mathrm{x}}(\omega)E^*_{\mathrm{x}}(\omega')$, which depends on the phase of the ionizing field.

4.2 The Exact Time Dependent Photoelectron Signal

We follow the microscopic treatment outlined in Refs. [98, 36] and reviewed in apprendix B.1, defining the photoelectron signal as the energy-resolved, integrated rate of change of the number of photoelectrons which gives the total energy-resolved photoelectron yield. This

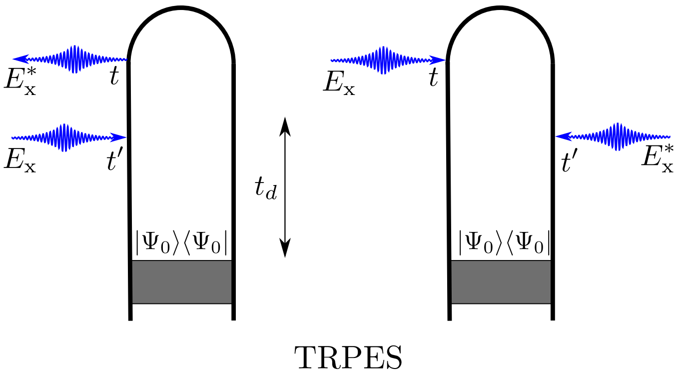

Figure 4.1: The two loop diagrams for the TRPES signal (Eq. (B.4)). Since the usual rules for loop diagrams maintain time-ordering, we show these two loops rather than a single loop with unrestricted times as would be implied by Eq. (4.5).

results in

$$S_{\rm e}(\varepsilon_{\mathbf{p}}, t_{\rm d}) = \int dt \int dt' \tilde{\mathcal{E}}_{\rm x}^{*}(t)\tilde{\mathcal{E}}_{\rm x}(t')e^{-i(\varepsilon_{\mathbf{p}}-\omega_x)(t-t')}\langle\hat{\mu}(t)\hat{\mu}^{\dagger}(t')\rangle_0\,, \tag{4.5}$$

where $\langle\ldots\rangle_0$ indicates an expectation value with respect to the initial state $|\Psi(t_0)\rangle = |\psi(t_0)\rangle \otimes |\phi(t_0)\rangle$ with ψ_0 and ϕ_0 the initial electronic and nuclear wave functions. The assumption of a product state form for the initial total wave function is justified when a single excited electronic state can be targeted by the pumping process but the generalization to a sum of such product states is straightforward if less succinct. The "e" subscript stands for "exact" and serves to differentiate it from the various approximate expressions defined below. In the above equation, the photoelectron part of the dipole correlation has been evaluated (this is possible since $[\hat{H}_{\mathbf{p}}, \hat{H}_{\rm M}] = 0$) and $\hat{\mu}$ ($\hat{\mu}^{\dagger}$)"annihilates" ("creates") the ion,

$$\hat{\mu} \equiv \sum_{\alpha a} \hat{\mu}_{\alpha a}^{\dagger}|a\rangle\langle\alpha|\,. \tag{4.6}$$

We note that Eqn. (4.5) assumes a uniform density of photoelectron states and will only be physical for $\varepsilon_{\mathbf{p}} > 0$. This can be ensured by shifting the carrier frequency of the ionizing pulse. We have also expanded the electric field amplitiudes into their positive and negative frequency components with carrier frequencies ($\tilde{\mathcal{E}}_{\rm x}^{(*)}(t)e^{\mp i\omega_x t}$) and kept only the rotating-wave terms. Equation (4.5) is the most straighforward way to simulate the time-resolved photoelectron spectrum and this will be done for 1- and 2-dimensional model systems in sections 4.4 and 4.5 respectively.

The molecular dipole correlation function in Eq. (4.5) can be straightforwardly expanded in the eigenstates of $\hat{H}_{\mathrm{mol}}$ in the full nuclear+electronic space. Indexing such states by $i, j, k, \ldots$ and expanding the initial wavefunction $|\Psi_0\rangle = \sum_i c_{i0}|i\rangle$, we obtain

$$S_{\mathrm{e}}(\varepsilon_{\mathbf{p}}, t_{\mathrm{d}}) = \sum_k |\sum_i c_{i0}\mu_{ki}\tilde{\mathcal{E}}_{\mathrm{x}}(\varepsilon_{\mathbf{p}} - \omega_{\mathrm{x}} - \varepsilon_i + \varepsilon_k)|^2 \mapsto \sum_{ki} \rho_{ii}|\tilde{\mathcal{E}}_{\mathrm{x}}\mu_{ki}|^2\delta(\varepsilon_{\mathbf{p}} - \omega_{\mathrm{x}} - \varepsilon_i + \varepsilon_k) \tag{4.7}$$

where the last relation follows on assumption of a mixed state with population of state i given by ρ_{ii} (electronic decoherence to such a mixed state can be described more rigorously in Liouville space [36]) and assuming a narrow-band pulse power spectrum. This exact Fermi Golden Rule (eFGR) in the full nuclear+electronic space is always possible to write but difficult to implement. The difficulty lies in the calculation of the eigenstates which is numerically intractible for all but the simplest systems. This form does however reveal that TRPES can be written as a sum of squares of transition amplitudes and is thus positive-definite (as must physically be the case). Also of note is the fact that the signal consists of an incoherent sum of exact population terms that do not mix; population transfer does not occur. Of course, this is a special property of the eigenbasis and does not generally hold for the product-state (adiabatic or diabatic) bases. This is of particular importance for CIs since the "good basis" becomes "bad" near the CI as the BOA breaks down and the nuclei couple different electronic states.

It is important to note that expressions formally equivalent to Eqs. (B.5) can also be obtained by calculating the expectation value of the photoelectron population for any time after the passage of the ionizing pulse. This is easily seen from the fundamental theorem of calculus on Eq.(B.1) and the initial condition of no photoelectrons [89, 90]. We have presented this slightly different derivation to highlight the analogy to light-based signals, which are derivable from the integrated rate-of-change of the photon number.

For comparison to the eFGR , it will be useful to also develop an understanding for the seperate roles that electronic populations and coherences play in Eq. (4.5) (note that populations and coherences are basis-dependent and we refer here to the adiabatic basis as opposed to the full eigenbasis which is not practial to utilize). To that end, we rewrite Eq. (4.5) using Eq. (4.6) as

$$\begin{aligned} S_{\mathrm{e}}(\varepsilon_{\mathbf{p}}, t_{\mathrm{d}}) = \int dt \int dt' \tilde{E}^*_{\mathrm{X}}(t) \tilde{E}_{\mathrm{X}}(t') e^{-i(\varepsilon_{\mathbf{p}} - \omega_{\mathrm{X}})(t-t')} \qquad (4.8) \\ \times \Bigg(\sum_{a\alpha} \langle \hat{M}^*_{a0}(t) \hat{\mu}_{\alpha a} \hat{M}_{\alpha\alpha}(t-t') \hat{\mu}^\dagger_{\alpha a} \hat{M}_{a0}(t') \rangle_{\phi_0} + \sum_{a \neq b, \alpha} \langle \hat{M}^*_{b0}(t) \hat{\mu}_{\alpha b} \hat{M}_{\alpha\alpha}(t-t') \hat{\mu}^\dagger_{\alpha a} \hat{M}_{a0}(t') \rangle_{\phi_0} \Bigg). \end{aligned}$$

In the above, we have defined the electronic transition amplitudes

$$\begin{aligned} \hat{M}_{a0}(t) &= \langle a | e^{-i\hat{H}_{\mathrm{M}} t} | \psi_0 \rangle \qquad (4.9) \\ \hat{M}_{\alpha\alpha}(t) &= \langle \alpha | e^{-i\hat{H}_{\mathrm{M}} t} | \alpha \rangle \,, \end{aligned}$$

where the expectation values are now solely over the initial nuclear wavefunction. The assumption of no coupling between ionized electronic states of the molecule prevents us from having to consider such terms as $\hat{M}_{\beta\alpha}(t)$ for $\beta \neq \alpha$.

The first term in Eq. (4.8) represents the contribution of electronic populations while the second term contains the coherence contributions. If the state initially prepared by the pump contains no electronic coherences (or they dephase before the probe) and the states $|a\rangle$ do not mix during the time propagation (they are eigenstates in the electronic subspace and the BOA holds), then the coherence terms would vanish by orthogonality. If either of these conditions is violated, the coherences must be accounted for.

4.3 The Quasistatic Approximation

To obtain the final FGR-like expression, we will substitute the temporal field envelopes in Eq. (4.8) for their Fourier transforms and approximate the nuclei as static during interaction with the ionizing pulse. This gives the quasi-static Fermi Golden Rule (qsFGR):

$$S_{\mathrm{qs}}(\varepsilon_{\mathbf{p}}, t_{\mathrm{d}}) = S_{\mathrm{qs}}^{\mathrm{pop}}(\varepsilon_{\mathbf{p}}, t_{\mathrm{d}}) + S_{\mathrm{qs}}^{\mathrm{coh}}(\varepsilon_{\mathbf{p}}, t_{\mathrm{d}})\,, \tag{4.10}$$

$$S_{\mathrm{qs}}^{\mathrm{pop}}(\varepsilon_{\mathbf{p}}, t_{\mathrm{d}}) = \sum_{a\alpha} \rho_{aa}(t_{\mathrm{d}}) |\mu_{\alpha a}(t_{\mathrm{d}}) \tilde{\mathcal{E}}_{\mathrm{x}}(\varepsilon_{\mathbf{p}} - \omega_{\mathrm{x}} + \varepsilon_{\alpha}(t_{\mathrm{d}}) - \varepsilon_{a}(t_{\mathrm{d}}))|^2\,, \tag{4.11}$$

$$\begin{aligned} S_{\mathrm{qs}}^{\mathrm{coh}}(\varepsilon_{\mathbf{p}}, t_{\mathrm{d}}) = &\sum_{a\neq b,\alpha} \rho_{ab}(t_{\mathrm{d}}) \langle \phi_{\alpha b}(t_{\mathrm{d}}) | \phi_{\alpha a}(t_{\mathrm{d}}) \rangle \mu_{\alpha b}(t_{\mathrm{d}}) \mu_{\alpha a}^{\dagger}(t_{\mathrm{d}}) \\ &\times \tilde{\mathcal{E}}_{\mathrm{x}}^{*}(\varepsilon_{\mathbf{p}} - \omega_{\mathrm{x}} + \varepsilon_{\alpha}(t_{\mathrm{d}}) - \varepsilon_{b}(t_{\mathrm{d}})) \tilde{\mathcal{E}}_{\mathrm{x}}(\varepsilon_{\mathbf{p}} - \omega_{\mathrm{x}} + \varepsilon_{\alpha}(t_{\mathrm{d}}) - \varepsilon_{a}(t_{\mathrm{d}}))\,, \end{aligned} \tag{4.12}$$

where we have replaced $c_a(t)c_b^*(t) = \rho_{ab}(t)$ for the electronic populations ($a = b$) and coherences ($a \neq b$), and explicitly separated the population and coherence terms (ε_b and $\mu_{\alpha b}$ are defined in analogy with Eqs. (B.21) and (B.22)). This is a FGR type expression in the electronic space where the time dependence due to expectation values is taken over the time-dependent nuclear wave packet as opposed to the full nuclear+electronic space. Since the summations in Eq. (4.10) contain far fewer terms than those in Eq. (4.7), this expression is much more tractable. On the other hand, it includes terms that are absent from the scFGR (Eq. (4.4)). The scFGR is an approximation to the population part of the qsFGR (Eq. (4.11)), which we term the quasi-static population Fermi Golden Rule (qspFGR) in which the nuclear propagation is treated semi-classically to obtain the time-dependence of the parameters (energies, dipoles, and populations).

Arriving at Eq. (4.8) entails no loss of generality. The key approximation, which is reflected in Eqs. (B.17)-(B.18) and (B.20)-(B.22), is that the molecule interacts with the ionizing x-ray pulse faster than the nuclei can appreciably move (the quasistatic approximation) and that the timescale of nuclear motion is much longer than the coherent electronic oscillation period. This is breaks down in the vicinity of a CI where the electronic energy gap vanishes. We have thus arrived at four versions of the FGR: (1) The exact FGR in the nuclear+electronic space (Eq. (4.7)), which does not mix populations (specifically, $|\psi_0\rangle = |i\rangle \Rightarrow |\psi(t)\rangle \propto |i\rangle$) since it is written in the eigenbasis. (2) The "quasistatic" FGR, which approximates the correlation function (from which the eFGR was obtained) by assuming frozen nuclei during the ionizing pulse in order to obtain an intuitive formula similar to the eFGR but in a more numerically tractable basis. (3) The 'quasistatic population" FGR (qspFGR), which neglects the electronic coherences in the qsFGR. (4) The "semiclassical" FGR (Eq. (4.4)) which approximates the qspFGR. Equation (4.11) still contains expectation values of the electronic energies taken over the exact nuclear wavefunction. Although this is an improvement over Eq. (4.7) (since the nuclear wavefunction can be numerically propagated without obtaining the exact eigenstates), Eq. (4.11) is still commonly approximated as in Eq. (4.4) by taking the nuclei as classical objects moving stochastically and then averaging over the resulting trajectories.

In this hierarchy of golden rules, the latter two (Eqs. (4.11) and (4.4)) appear nearly identical and both appear very similar to the exact (Eq. (4.7)). However, as we remarked earlier, the latter two are written in a product adiabatic basis rather than the full nuclear+electronic eigenbasis. While this make simulations easier due to the smaller number of terms in the summation, it also means that the states can couple and will generally mix. This mixing will transfer electronic population between states while generating electronic coherences (Eq. (4.12)). While the quasi-static assumption of frozen nuclei during the ionization process may be well-justified for ultrashort pulses, dropping the electronic coherence terms is not justified when coherences are internally generated by the propagation due to the breakdown of the BOA and the coupling of electronic states through the nuclei. We have thus shown that the FGR approach can easily be extended by the inclusion of coherence terms (Eq. (4.12)) to obtain the more general qsFGR (Eq. (4.10)). This allows the effects of electronic coherence on the TRPES signal to be calculated at a similar computational cost to the commonly employed scFGR. In Sec. 4.4, we will explore the consequences of these internally-generated coherences and what information may be obtained from their contribution to the signal.

We now examine more closely Eq. (4.12), which encodes the coherence contributions to TRPES within the quasistatic approximation. It is apparent that, while the population terms depended on the power spectrum $|\tilde{\mathcal{E}}_{\mathrm{x}}(\omega)|^2$, the coherence terms depend on the frequency-dependent phase of the ionizing pulse via $\tilde{\mathcal{E}}^*_{\mathrm{x}}(\omega)\tilde{\mathcal{E}}_{\mathrm{x}}(\omega')$, opening up another avenue of control for these signals. Also of note is the nuclear coherence factor $\langle\phi_{\alpha b}(t_{\mathrm{d}})|\phi_{\alpha a}(t_{\mathrm{d}})\rangle$ (missing from the populations since the nuclear wave packets are normalized). This factor represents the overlap of the nuclear wave packet on state a at time t_{d} with that on state b. Since the two potential surfaces are typically different, the two wave packets will generally not overlap appreciably after some time. This factor therefore adds a decay that complicates the observation of the coherence terms and can justify their exclusion, as in the scFGR, when the decay is sufficiently fast relative the delay times t_{d}. This is ordinarily the case, for example, in slow picosecond TRPES but is not generally true in the ultrafast regime. In a more comprehensive treatment, nuclear movement during ionization, as well as spectator modes, would further decohere these terms. While these effects are important, are present interest is in the effects of the electronic coherences while they are still around.

As will be illustrated in the next section, the most visible signature of the coherence terms in TRPES is a characteristic oscillatory pattern in the t_{d}-dependence of the electronic coherence $\rho_{ab}(t_{\mathrm{d}})$. The frequency of this beating pattern allows one to determine the separation between states a, b without direct spectral resolution. In principle, the actual oscillation period is related to the eigenenergies, which complicates the interpretation of the beating pattern in the region of the CI. Once the nuclear wave packet is sufficiently far from the CI for the inter-surface coupling to be small relative to the electronic energy separation, the frequency can safely be interpreted as corresponding to the gap. In our models, we find that the onset of this regime is relatively rapid (within a few fs of the wave packets arrival at the CI). In this sense, the CI acts as a scatterer that transfers population between the two electronic states but also sets in motion a coherent oscillation.

Finally, we note that, if one simply invokes the reasonable approximation that $\rho_{ab}(t_\mathrm{d}) \sim \rho_{ab} e^{-i\omega_{ab} t_\mathrm{d}}$, we can transform $a \leftrightarrow b$ and combine terms to get

$$S_\mathrm{qs}^\mathrm{coh}(\varepsilon_\mathbf{p}, t_\mathrm{d}) \sim \sum_{ab} \cos\left(\omega_{ab} t_\mathrm{d}\right) \tag{4.13}$$

where we have dropped all other factors inside the summation. This term is clearly not positive-definite and the coherence term can therefore both enhance or suppress the population term in the photoelectron signal. Thus, the presence of coherence can suppress or enhance the "primary" photoionization process. This can be understood as the presence of the coherence opening up new pathways that interfere destructively or constructively with the population ionization pathways.

4.4 Comparison of the FGR Expressions

In this section, we will simulate the TRPES signal for a model involving a single nuclear coordinate with the various FGR expressions as well as with Eq. (4.5). The correlation function expression implicitly includes both population and coherence contributions, as can be seen from its expanded form in Eq. (4.8), and, combined with a state propagation scheme, offers an exact way to simulate the full TRPES signal. Rather than specifying the adiabatic potential surfaces, we will work from the outset in the diabatic basis. This simplification to a scalar coupling retains the essential physics of an inter-surface coupling in the region of a degeneracy and the population transfer and coherence creation that follows from such coupling. We assume three relevant electronic states, two unionized (labeled $|1\rangle$ and $|2\rangle$) and one ionized ($|3\rangle$). The two unionized states intersect and are coupled near the intersection point and all three surfaces are taken to be harmonic with the same shape. This is the simplest model that can illustrate the effect of electronic coherences on TRPES signals and will serve as a readily-comprehensible test-case. The molecular Hamiltonian in the diabatic basis reads

$$\hat{H}_{\mathrm{M}} = \sum_{j=1}^{3} |j\rangle \big(\hat{T}_j + \hat{V}_j\big) \langle j| + |1\rangle \hat{V}_{12} \langle 2| + |2\rangle \hat{V}_{21} \langle 1| \tag{4.14}$$

where $\hat{T}_j \equiv -\frac{1}{2m}\frac{d^2}{dx^2}$, the nuclear kinetic energy operator, is now diagonal in the electronic space (see appendix C.0.2 for parameters). We give all three diabatic surfaces the same curvature to maximize the coherence time which is limited by the nuclear wavefunction overlap.

The initial wavepacket (assumed to be on surface 1 initially) as well as all potential surfaces and the inter-surface coupling are displayed in Fig. 4.2 (top). We then propagate this initial wavepacket using a Short Iterative Lanczos (SIL) scheme [99] and calculate the two-time dipole correlation function, working in the Condon approximation and taking all dipole elements to be unity for simplicity. More rigorous treatment of μ can be approximated for example by Dyson orbitals [100], which introduce weight factors for different ion states as well as angular distributions. The time-dependent populations of the neutral electronic states and the magnitude of their coherence are plotted in Fig. 4.2 (Bottom). Taking the ionizing pulse to be a Gaussian with central time t_{d}, standard deviation σ_T, and carrier frequency ω_{x} (see Eq. (D.3)), we calculate Eq. (4.5) and compare to the qspFGR result (Eq. (4.11)) in Fig. 4.3. This comparison immediately reveals the presence of coherent oscillations in the directly propagated signal that are absent in the approximate FGR result. This failure of the qspFGR is due to the fact that the electronic states (whether adiabatic or diabatic) are not eigenstates of the molecular Hamiltonian. The coupling $\hat{V}_{12}$ couples unionized electronic states and the propagator therefore mixes them. This renders the coherence term in Eq. (4.8) finite and we must go beyond the qspFGR/scFGR.

Although the restricted time window used to capture the ultrafast dynamics has left us with insufficient spectral resolution to directly resolve the two unionized surfaces, the beating pattern reveals their splitting. A visual inspection of the coherent oscillations reveals a period of roughly 10 fs. The average separation between unionized electronic surfaces from $t_{\mathrm{d}} = 45\,\mathrm{fs}$ to $t_{\mathrm{d}} = 65\,\mathrm{fs}$ (roughly the time from first peak to last peak in the oscillation pattern) corresponds to a beating period of 9.74 fs, a relative error of only 2.6%.

In deriving Eq. (4.11), we have made the quasistatic approximation, where we neglected the kinetic energy for the duration of the ionizing pulse and the contribution from electronic coherences. To investigate the relative importance of these two approximations, we also have computed separately the first term in Eq. (4.8), which neglects coherences but makes no assumption of frozen nuclei, and Eq. (4.12), which is the contribution from electronic coherences but assumes frozen nuclei during the ionization. Although it is clear that the origin of the oscillatory pattern is the coherence terms, we would like to determine how good the quasistatic approximation is. In particular, if the qsFGR (Eq. (4.10)) is a good approximation to Eq. (4.5), then this simple patch-up can account for the coherent oscillations and we could avoid the extra propagation that comes with violations of the quasistatic approximation. The qsFGR therefore offers a simple extension of the scFGR that captures the effects of electronic coherences generated internally by the propagation through a region of nonadiabatic dynamics. It is important to note however, that correctly reproducing these oscillations will require accurate propagation of the magnitude and phase of the coherence $\rho_{ab}(t_{\mathrm{d}})$.

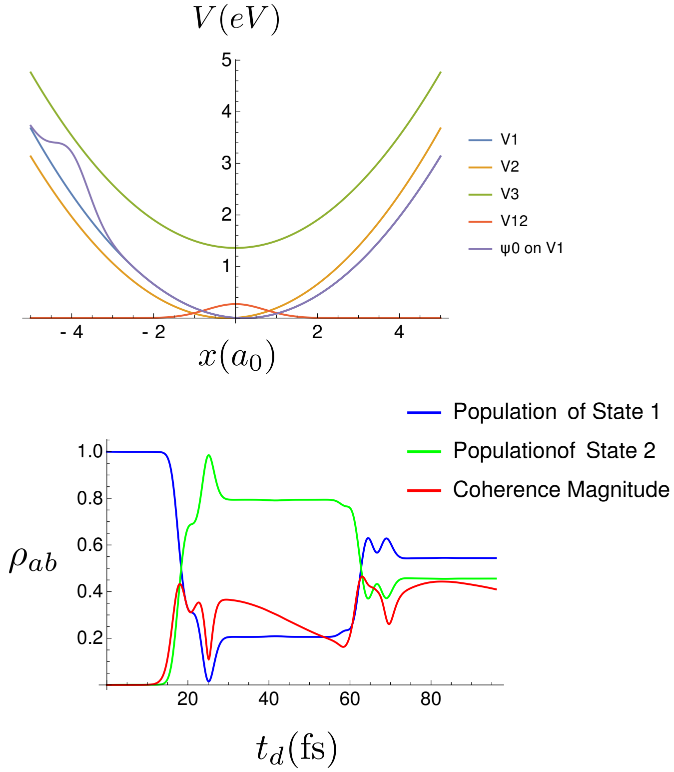

Figure 4.2: (Top) Nuclear dependence of the diabatic electronic energies including the potential coupling the two unionized surfaces. The initial nuclear wavepacket (rescaled for visualization) is on the V_1 surface. (Bottom) The populations and coherence magnitude for the unionized adiabatic states for the first 96 femtoseconds. It is noteworthy that the coherence remains appreciable relative to the populations for some time after its creation.

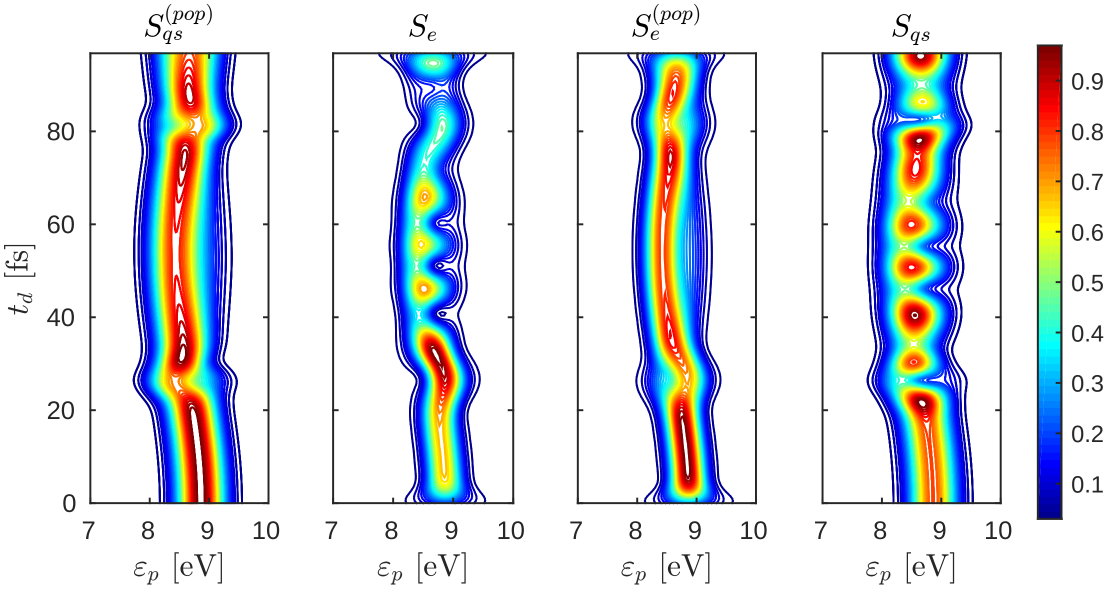

Figure 4.3: Time-resolved photoelectron spectrum for the 1-D model (appendix C.0.2 simulated using the qspFGR (Eq. (4.11)) (far left), the full correlation function and a direct propagation scheme (Eq. (4.5)) (middle left). Note the prominent oscillations in the latter simulation that reflect the generation of electronic coherence at the CI. This beating pattern is clearly absent from the scFGR simulation on the left. To assess the relative importance of (1) the quasistatic approximation and (2) neglecting electronic coherences, we also present the population-only contribution to the correlation-function expression for TRPES (first term in Eq. (4.8) (middle left) and compare to the qsFGR (Eq. (4.10)) (far right). Note the similarity of the exact and quasi-static results. This indicates that the quasistatic approximation is good enough for qualitative purposes provided electronic coherence terms are included.

4.5 Electronic Coherences Created at Conical Intersections

We now present simulations of the TRPES signal for a molecular model system (see appendix **??** for details) representing the branching space of a Conical Intersection [101] by using the exact expression in combination with a fully quantum propagation. We take into account two excited electronic states S_1 and S_2 and the two nuclear coordinates $x = (x_g, x_h)$ that resemble the gradient difference and the derivative coupling vector respectively. The cation states D_0 and D_1 are used as target states to probe the electron dynamics near the CI. The cationic potential energy surfaces (PES) are in the same nuclear coordinates but do not posses a CI in the space used for the simulations. The ionization energies for D_0 and D_1 at the CI point are 6.9 and 7.5 eV respectively. The molecular Hamiltonian is composed of a Cartesian-type kinetic-energy operator and the corresponding neutral and cation diabatic PESs:

$$H = \sum_{j=1}^{4} |j\rangle\big(\hat{T}_j + \hat{V}_j\big)\langle j| + |1\rangle\hat{V}_{12}\langle 2| + |2\rangle\hat{V}_{21}\langle 1| \tag{4.15}$$

where V_1 and V_2 are PESs of the neutral states S_1 and S_2, V_{12} is the diabatic coupling, V_3 and V_4 are the PESs of the cation states D_0 and D_1 and $\hat{T}_j \equiv \sum_{i\in h,g} \frac{-1}{2m}\frac{d^2}{dx_i^2}$ is the nuclear kinetic energy operator acting on electronic state j (we use a reduced mass m of 30000 au or $\approx$ 16 amu). The transition dipole moments between the neutral cation states are assumed to be constant with respect to the nuclear coordinate. The time evolution is simulated by wave packet dynamics on a numerical grid using a time stepping scheme (see appendices B.1 and C.1). The initial wave function is created by assuming impulsive excitation from the electronic ground state S_0 to the S_2 state.

The time evolution of the populations and the electronic coherence of the neutral states S_1

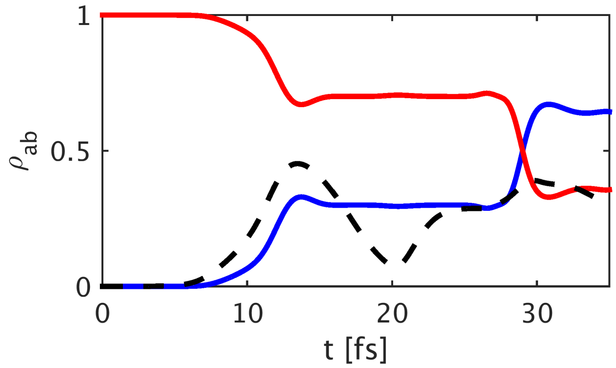

Figure 4.4: Time evolution of the electronic states populations (S_2 red, S_1 blue) and the coherence magnitude (black, dashed) for the CI model.

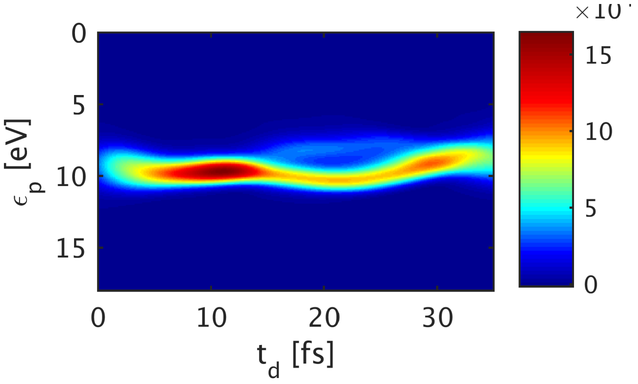

Figure 4.5: TRPES Signal for CI with 4 fs FHWM and 20 eV central frequency.

and S_2 is shown in Fig. 4.4. The wave packet reaches the CI within ≈8-15 fs, resulting in an overall population transfer of ≈30 %. The electronic coherence build up is maximal at 13.5 fs, when the main fraction of the wave packet has passed the CI, followed by a decay of the coherence caused by the different gradients in S_1 and S_2. At 20 fs, the wave packet returns and the coherence rebuilds until the second passage through the CI at ≈30 fs. Between 15 and 25 fs the system the systems moves through a region, where coupling V_{12} is negligible and the nuclear wave packets propagate freely on the potential energy surfaces. Note that the term electronic coherence is not clearly defined around the CI since the nuclear and electronic wave functions are strongly mixed (i.e. around 10 and 30 fs).

The corresponding TRPES signals calculated for the exact correlation function expression (Eq. 4.5) are shown in Fig. 4.5 and Fig. 4.6 for two ionization pulse lengths. The signal in

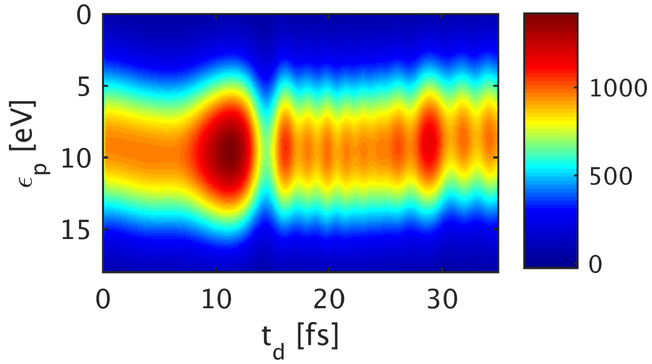

Figure 4.6: TRPES Signal for CI with 200 as FHWM and 20 eV central frequency.

Fig. 4.5 is calculated for an ionization pulse, which is long compared to the time scale of the electron dynamics (4 fs FWHM). The splitting of both states is spectrally resolved at around 20 fs (the faint signal at 7 eV stems from the S_1 state). However, the fast oscillation which are expected from the coherence contribution can not be resolved with the chosen pulse length. The signal in Fig. 4.6 is calculated for an ionization pulse short compared to the time scale of the electron dynamics (0.2 fs FWHM). Here, the spectral features can not be resolved anymore. The coherent oscillation pattern in the time domain is now fully resolved and visible between 15 fs and 20 fs. The two ion states are separated by ≈0.6 eV, and they can not be distinguished for the chosen pulse parameters. However, the coherent oscillation pattern is not affected by presence of two ion states. The coherent features of the TRPES signal can be matched in an approximate way against the time evolution of the real part of the coherence $\Re(\rho_{ab})$ (see appendix B.1.1 for details) shown in Fig. 4.7(a). The adiabatic and diabatic coherence are identical, while the wave packet leaves the coupling region (Fig. 4.7(b)) and the oscillations in the signal stem solely from the electronic states. This can be understood qualitatively by the inspection of Eq. (4.8), which separates the contributions to signal into electronic populations and coherences. Assuming the Condon approximation and the limit of short ionization pulses (i.e. the nuclei do not move in the ion states) the second term in Eq. (4.8) is proportional to the real part of the coherence $\Re(\rho_{ab})$. Note that a negative $\Re(\rho_{ab})$ depletes the signal contribution from the populations due to destructive

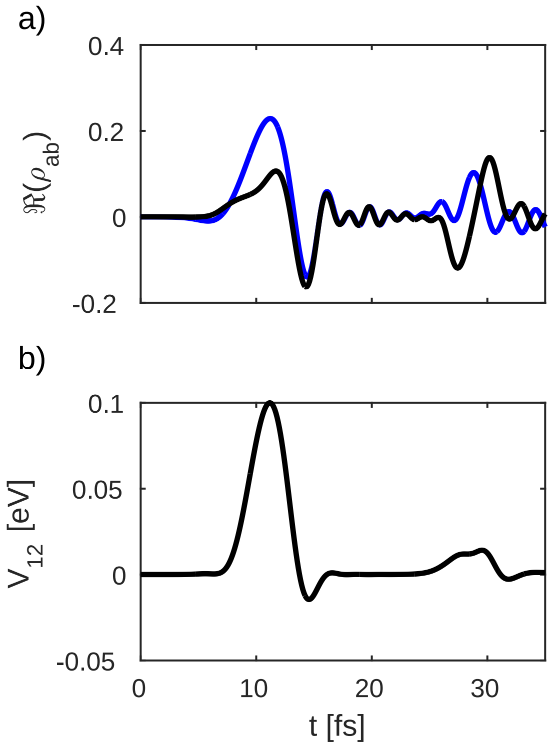

Figure 4.7: (a) Time evolution of the real part of the electronic coherence in the diabatic basis (blue) and the adiabtic basis (black). (b) Time evolution of the Expectation value of the diabatic coupling (V_{12})

interference (as for example at 14.5 fs in Fig. 4.7 and Fig. 4.6).

From the comparison of the signals in Fig. 4.5 and Fig. 4.6, it becomes clear that, in the exact expression, the signal is fully subject to the Fourier uncertainty – Time and frequency have to be traded off against each other like in an experiment. However, this is not the case for the qsFGR, where a change in pulse length only affects the spectral but not the temporal resolution.

4.6 Conclusions

In this chapter we have presented and analyzed a hierarchy of expressions for the calculation of TRPES signals. The main results of the chapter are the exact correlation function expression (Eq. (4.5)) and the qsFGR (Eq. (4.10)), which extends the widely used scFGR (Eq. (4.4)) via the inclusion of electronic coherences, accounting for the nuclear overlap between the electronic states. In contrast to the pure population contribution, this term is sensitive to the phase of the ionizing electric field and leads to a beating pattern in the photoelectron yield. In model calculations, we have shown that these oscillations can be resolved by the use of attosecond pulses. While the exact correlation function method is mainly intended for use with wave packet propagation protocols on small systems and can be computationally demanding, the qsFGR can be used along with semi-classical molecular dynamics protocols to simulate larger molecular systems. The presented formalism can be applied in an analogous way for the description of photo-detachment signals in anions ($A^- \rightarrow A$ rather than $A \rightarrow A^+$) [94].

In previous studies [89, 90], exact wavefunction propagations were used that are formally identical to our Eq. (4.5). Those studies focused on coherent vibrational dynamics and slower electronic population dynamics. Moreover, a common model to consider is one in which each neutral state ionizes to a separate cationic state. In the absence of intersurface coupling in the cationic manifold, the coherence terms for such models vanish identically. Although such coupling had been considered [90], we can see by Eq. (4.8) that the influence of such terms will be limited by the temporal duration of the ionizing pulse. When only electronic population dynamics and coherent vibrational dynamics are important, the qspFGR (which may be approximated by the scFGR) is sufficient to simulate the signal in the quasistatic limit. This approximation is intuitive and frequently employed [84, 83, 91]. It is only when the two neutral states can both ionize to the same cationic state and the pulses employed are sufficiently short to capture the electronic oscillations that the coherence terms are revealed.

The strategies presented to calculate the signal can readily be interfaced with existing non-adiabatic molecular (quantum) dynamics simulation protocols. The most straightforward way is to evaluate the correlation function Eq. (4.5) directly from a time propagation of a wave function in the combined electronic+nuclear space. For example, the molecular system can be propagated in a wave packet approach with the Fourier method [99] in a reduced space of nuclear coordinates [102] including the non-adiabatic couplings [103, 104]. The numerical evaluation of the correlation function is then straightforward [52]. Alternatively approximate wave function methods like Multi Configuration Time-Dependent Hartree (MCTDH) [105] can be used to include more vibrational modes and also to evaluate the correlation function. Semi-classical wave packet propagation protocols like Ab Initio Multiple Spawning (AIMS) [96] or Hagendorn wave packets [106] provide access to the nuclear wave function and are thus also suitable for the the correlation function method. However, the numerical effort to calculate the signal grows quadratically with the number of time steps, since the correlation function is a function of two variables (t and t'). Moreover, it requires a propagation on the potential energy surface of the ionized molecule. This is in contrast to the various derived FGR expressions, where the numerical effort of the signal calculation only grows linearly with the number of steps. The exact FGR expression (Eq. 4.7)) requires the eigenstates in the full electronic + nuclear subspace and is thus limited in its applicability. It may however be advantageous in special cases where an diagonalization of an approximate Hamiltonian is feasible (for example in combination with a vibronic coupling Hamiltonian [107]). The linear scaling with respect to the number of time steps might outperform the cost of diagonalization in some cases.

The different types of the FGR presented here neglect the nuclear propagation in the ionized states and only require a single time propagation, making them suitable for combination with semi-classical protocols and the description of larger systems. The scFGR, which neglects the contributions of the electronic coherences, has been successfully used in combination with AIMS [84]. An extension to use it with the qsFGR (Eq. (4.10)) seems straightforward, since AIMS properly includes the necessary nuclear overlap term (Eq. (4.12)). In principle, the qsFGR expression can also easily be applied to all wave function based methods mentioned above, as long as the nuclear overlap term is accessible. In contrast to the correlation function, the qsFGR does not require time propagation in the ionized molecular states, significantly simplifying its calculation. Simulation protocols like Tully's fewest switch surface hopping (FSSH) method [97], which treat the nuclei classically are easy to combine with the scFGR [36, 108]. However, the basic version of the FSSH algorithm does not account for the decay of electronic coherences. The result would be an overestimation of coherence contributions to the TRPES signal. Extensions of FSSH, which allow corrections for coherence decay [109, 110, 111, 112], may be used to approximate the nuclear overlap term in Eq. (4.12), and combine the class of FSSH methods with the qsFGR. TRPES could provide an experimental test for the various simulation algorithms.

Our model system simulations clearly indicate that a fast build up of electronic coherences results in an ultrafast, time-domain oscillation pattern in the TRPES signal. Its oscillation period is connected to the energy splitting between the neutral electronic states. A comparison of the different signals yields the conclusion that the qsFGR is a good approximation for the inclusion of electronic coherences beyond the scFGR. However, the quasistatic approximation introduces a unrealistic resolution in the time domain by ignoring the time evolution of the system within the pulse duration. The qsFGR is thus valid for pulses which are short compared to the timescale of the internal dynamics with the scFGR making the additional assumption of neglecting electronic coherences.

In this chapter, we have simulated a model system of a CI between excited molecular states to demonstrate that the coherent oscillation pattern can be observed in a realistic setting. To obtain an observable coherence, a system with a CI in the vincinity of the Franck-Condon point is required to retain a compact wave packet (for example [53, 55, 75, 76]). The oscillation pattern is revealed if appropriate sub-femtosecond pulses are chosen. The information about the potential energy surface splitting can then be detected through the oscillation period in the time domain instead of the frequency domain. Note that this method accesses information similarly to the resonant linear absorption signal [98, 87]. Finally we note that wave functions at CIs are known to have a geometric Berry phase [77] that depends on the topology and is independent of the details of the potential surfaces. The Berry phase so far has eluded detection in chemical systems. Spectroscopic signals like TRPES and TRUECARS [88], which are sensitive to the phase of the pulse and the phase of the electronic coherences, might also provide a new strategy for the experimental observation of geometric phases.

Chapter 5

Conclusion

In this thesis, we have endeavored to provide a very general viewpoint from which to analyze signals performed with ultrafast x-ray pulses. The first step of this is to separate the last (or last few) interaction(s) from all previous interactions in the perturbative expansion of a material expectation value. The latter, called the pump, creates an arbitrary nonstationary state that evolves freely for at least some finite time before the former interaction(s), termed the probe. This formulation is quite general. The point is that, provided the pump and probe are temporally seperable, the information to which a given probe technique is sensitive does not depend on the (pumped) state of the matter. Thus, by cataloguing a variety of probes and their properties, we can establish an understanding for what a given signal will show.

Chapter 2 provides a systematic classification scheme for x-ray Raman signals in terms of correlation functions of the resonant or off-resonant polarizability $\hat{\alpha}$. The basis of all signals examined is the frequency-dispersed photon number change, with it's zeroth and first moments playing the role of auxilliary signals corresponding to total photon number change and total field energy change respectively. Each of these three types of signals can be resonant or off-resonant, linear or quadratic (or higher order) in the field intensity, and performed with broadband or hybrid pulses. After systematic analysis on simple model systems, general properties of all of these signals were obtained, permitting one to select from this toolbox of techniques based on the information one wants to probe.

In chapter 3, we track the dynamics of 1- and 2-D model systems using the $S_{\mathrm{OLH}}^{(\mathrm{fd})}$ detection protocol. Though low-order, this signal is perhaps not as obvious initially since it frequently vanishes, requiring the presence of electronic coherences in the material as well as control of the relative phases of the hybrid pulse constituents in order to remain finite. As an off-resonant signal, it total photon number is conserved and photons are merely redistributed between the modes of the electromagnetic field. We thus term this technique transient redistribution of ultrafast electronic coherences by attosecond Raman spectroscopy or TRUECARS. This technique is analogous to the second half of an electronic coherent anti-stokes Raman spectroscopy (electronic-CARS) experiment, the primary difference being that the detected coherence is generated internally by nonadiabatic couplings rather than imprinted externally via a Raman interaction with a previously-applied laser pulse. This technique directly times the arrival of the nuclear wavepacket at the region of the CI since this is the point where the coherences are generated by the NACs. Moreover, the resulting coherent oscillations reveal the time-evolving gap between the electronic energy levels. Although this is, in principle, frequency-domain information, it would not be accessible via a frequency-domain experiment since the nuclear configuration is highly transient.

In chapter 4, we apply a similar analysis to time-resolve photoelectron spectroscopy (TR-PES). The relevant material parameter is now a two-point time correlation function rather than a single-time expectation value as in TRUECARS and thus the required time-propagations are somewhat more demanding. This leads us to explore a hierarchy of ways in which to account for the nuclear dynamics. Our analysis lead to a quasistatic approximation, in which the nuclei are taken as frozen during the ionization process, that serves as a sort of middle-ground between an eigenstate representation and the correlation function expressions. This expression is fully quantum-mechanical but readily lends itself to semiclassical or classical simulation. The approach could also be used to derive a quasistatic approximation for $S_{\mathrm{RQ}}^{(\mathrm{fd})}$ by taking the nuclei as frozen during the time spent in a core excited state. Given that this signal is, at its core, a four-point correlation function, such a simplification could greatly facilitate calculation.

The extension of spectroscopic techniques into the attosecond and x-ray regimes offers promising new possibilities for probing matter. Newly-developed XFEL and HHG sources can produce pulses with these parameters, bringing ultrafast material dynamics that is ordinarily unseen into the range of experiment. The dream of making molecular movies, of stroboscopically watching frame-by-frame as complicated reaction dynamics play out, is drawing closer. Simulating and interpretating these signals is a significant challenge, as we begin to enter regimes where long-used approximations lose validity, but one with high reward, improving humanity's understanding of chemical dynamics. We hope that this thesis can be of some small help to those who embark on this journey.

Bibliography

[1] Saar Rahav and Shaul Mukamel. Ultrafast nonlinear optical signals viewed from the molecules perspective: Kramers-heisenberg transition amplitudes vs. susceptibilities. *Adv. At. Mol., Opt. Phys.*, 59:223, 2010.

[2] Ahmed H Zewail. Laser femtochemistry. *Science*, 242(4886):1645–1653, 1988.

[3] Ahmed H Zewail. Femtochemistry: Atomic-scale dynamics of the chemical bond. *The Journal of Physical Chemistry A*, 104(24):5660–5694, 2000.

[4] Shaul Mukamel and Saar Rahav. Ultrafast nonlinear optical signals viewed from the molecules perspective: Kramers–heisenberg transition-amplitudes versus susceptibilities. *Advances in atomic, molecular, and optical physics*, 59:223–263, 2010.

[5] Konstantin E Dorfman and Shaul Mukamel. Multidimensional spectroscopy with entangled light: loop vs ladder delay scanning protocols. *New journal of physics*, 16(3):033013, 2014.

[6] S. Mukamel. *Principles of Nonlinear Optics and Spectroscopy*. Oxford University Press, Oxford, UK, 1995.

[7] Dmitry Pestov, Robert K Murawski, Ariunbold Gombojav, Xi Wang, Miaochan Zhi, Alexei V Sokolov, Vladimir A Sautenkov, Yuri V Rostovtsev, and Marlan O Scully. Hybrid of frequency and time resolved cars. In *Conference on Lasers and Electro-Optics*, page CThY6. Optical Society of America, 2007.

[8] YL Li, L Huang, RJ Dwayne Miller, Taisuke Hasegawa, and Yoshitaka Tanimura. Two-dimensional fifth-order raman spectroscopy of liquid formamide: Experiment and theory. *The Journal of Chemical Physics*, 128(23):234507, 2008.

[9] Ji-xin Cheng, Andreas Volkmer, Lewis D. Book, and X. Sunney Xie. Multiplex coherent anti-stokes raman scattering microspectroscopy and study of lipid vesicles. *The Journal of Physical Chemistry B*, 106(34):8493–8498, 2002.

[10] Michiel Mller and Juleon M. Schins. Imaging the thermodynamic state of lipid membranes with multiplex cars microscopy. *The Journal of Physical Chemistry B*, 106(14):3715–3723, 2002.

[11] Tak W. Kee and Marcus T. Cicerone. Simple approach to one-laser, broadband coherent anti-stokes ramanscattering microscopy. *Opt. Lett.*, 29(23):2701–2703, Dec 2004.

[12] Andreas Volkmer. Vibrational imaging and microspectroscopies based on coherent anti-stokes raman scattering microscopy. *Journal of Physics D: Applied Physics*, 38(5):R59, 2005.

[13] Bernhard von Vacano, Lars Meyer, and Marcus Motzkus. Rapid polymer blend imaging with quantitative broadband multiplex cars microscopy. *Journal of Raman Spectroscopy*, 38(7):916–926, 2007.

[14] Ian A. Walmsley and Christophe Dorrer. Characterization of ultrashort electromagnetic pulses. *Adv. Opt. Photon.*, 1(2):308–437, Apr 2009.

[15] Xi Wang, Aihua Zhang, Miaochan Zhi, Alexei V. Sokolov, George R. Welch, and Marlan O. Scully. Heterodyne coherent anti-stokes raman scattering for spectral phase retrieval and signal amplification. *Opt. Lett.*, 35(5):721–723, Mar 2010.

[16] Sukesh Roy, Paul J. Wrzesinski, Dmitry Pestov, Marcos Dantus, and James R. Gord. Single-beam coherent anti-stokes raman scattering (cars) spectroscopy of gas-phase co2 via phase and polarization shaping of a broadband continuum. *Journal of Raman Spectroscopy*, 41(10):1194–1199, 2010.

[17] L. Yuan, A.A. Lanin, P.K. Jha, A.J. Traverso, D.V. Voronine, K.E. Dorfman, A.B. Fedotov, G.R. Welch, A.V. Sokolov, A.M. Zheltikov, and M.O. Scully. Coherent raman umklappscattering. *Laser Physics Letters*, 8(10):736–741, 2011.

[18] Joe Farrell, Brian McFarland, Nora Berrah, C Bostedt, John Bozek, Phil Bucksbaum, Ryan Coffee, James Cryan, L Fang, Raimund Feifel, et al. Ultrafast x-ray probe of nucleobase photoprotection. In *Quantum Electronics and Laser Science Conference*, pages QW1F–4. Optical Society of America, 2012.

[19] Yoshitaka Tanimura and Shaul Mukamel. Two-dimensional femtosecond vibrational spectroscopy of liquids. *The Journal of Chemical Physics*, 99(12):9496–9511, 1993.

[20] Fouad El-Diasty. Coherent anti-stokes raman scattering: Spectroscopy and microscopy. *Vibrational Spectroscopy*, 55(1):1 – 37, 2011.

[21] Konstantin E Dorfman, Benjamin P Fingerhut, and Shaul Mukamel. Time-resolved broadband raman spectroscopies: A unified six-wave-mixing representation. *The Journal of Chemical Physics*, 139(12):124113, 2013.

[22] H Frostig, T Bayer, N Dudovich, Y Eldar, and Y Silberberg. Single-pulse two-dimensional raman spectroscopy. *In Press*.

[23] Cristian Manzoni, Oliver D Mücke, Giovanni Cirmi, Shaobo Fang, Jeffrey Moses, Shu-Wei Huang, Kyung-Han Hong, Giulio Cerullo, and Franz X Kärtner. Coherent pulse synthesis: towards sub-cycle optical waveforms. *Laser Photonics Rev.*, 2014.

[24] S Shwartz, Matthias Fuchs, JB Hastings, Y Inubushi, T Ishikawa, T Katayama, DA Reis, T Sato, K Tono, M Yabashi, et al. X-ray second harmonic generation. *Physical Review Letters*, 112(16):163901, 2014.

[25] Tenio Popmintchev, Ming-Chang Chen, Dimitar Popmintchev, Paul Arpin, Susannah Brown, Skirmantas Ališauskas, Giedrius Andriukaitis, Tadas Balčiunas, Oliver D Mücke, Audrius Pugzlys, et al. Bright coherent ultrahigh harmonics in the kev x-ray regime from mid-infrared femtosecond lasers. *Science*, 336(6086):1287–1291, 2012.

[26] Satoshi Tanaka and Shaul Mukamel. Coherent x-ray raman spectroscopy: a nonlinear local probe for electronic excitations. *Physical review letters*, 89(4):043001, 2002.

[27] Shaul Mukamel, Daniel Healion, Yu Zhang, and Jason D. Biggs. Multidimensional attosecond resonant x-ray spectroscopy of molecules: Lessons from the optical regime. *Annu. Rev. Phys. Chem.*, 64:101, May 2013.

[28] H. R. Hudock, B. G. Levine, A. L. Thompson, Helmut Satzger, Dave Townsend, N. Gador, Albert Stolow, and Todd J. Martinez. Ab initio molecular dynamics and time-resolved photoelectron spectroscopy of electronically excited uracil and thymine. *J. Phys. Chem. A*, 111:8500–8508, 2007.

[29] S Miyabe and P Bucksbaum. Transient impulsive electronic raman redistribution. *Phys. Rev. Lett.*, 114(14):143005, 2015.

[30] BK McFarland, JP Farrell, S Miyabe, F Tarantelli, A Aguilar, N Berrah, C Bostedt, JD Bozek, PH Bucksbaum, JC Castagna, et al. Ultrafast x-ray auger probing of photoexcited molecular dynamics. *Nat. Comm.*, 5, 2014.

[31] Konstantin E Dorfman, Kochise Bennett, and Shaul Mukamel. Detecting electronic coherence by multidimensional broadband stimulated x-ray raman signals. *arXiv preprint arXiv:1506.08226*, 2015.

[32] Kazuo Nakamoto. *Infrared and Raman spectra of inorganic and coordination compounds.* Wiley Online Library, 1986.

[33] Takuro Ideguchi, Simon Holzner, Birgitta Bernhardt, Guy Guelachvili, Nathalie Picqué, and Theodor W Hänsch. Coherent raman spectro-imaging with laser frequency combs. *Nature*, 502(7471):355–358, 2013.

[34] Jason D. Biggs, Yu Zhang, Daniel Healion, and Shaul Mukamel. Two-dimensional stimulated resonance raman spectroscopy of molecules with broadband x-ray pulses. *The Journal of Chemical Physics*, 136(17):174117–174117–16, May 2012.

[35] Yu Zhang, Jason D Biggs, Weijie Hua, Konstantin E Dorfman, and Shaul Mukamel. Three-dimensional attosecond resonant stimulated x-ray raman spectroscopy of electronic excitations in core-ionized glycine. *Physical Chemistry Chemical Physics*, 16:24323, 2014.

[36] Kochise Bennett, Markus Kowalewski, and Shaul Mukamel. Probing electronic and vibrational dynamics in molecules by time-resolved photoelectron, auger-electron, and x-ray photon scattering spectroscopy. *Faraday Discuss.*, 177:405–428, 2015.

[37] Bijay Kumar Agarwalla, Hideo Ando, Konstantin E Dorfman, and Shaul Mukamel. Stochastic liouville equations for femtosecond stimulated raman spectroscopy. *The Journal of Chemical Physics*, 142(2):024115, 2015.

[38] G Batignani, G Fumero, S Mukamel, and T Scopigno. Energy flow between spectral components in 2d broadband stimulated raman spectroscopy. *Physical Chemistry Chemical Physics*, 17(16):10454–10461, 2015.

[39] Philipp von den Hoff, Sebastian Thallmair, Markus Kowalewski, Robert Siemering, and Regina de Vivie-Riedle. Optimal control theory - closing the gap between theory and experiment. *Phys. Chem. Chem. Phys.*, 14:14460, 2012.

[40] Maria F Garcia-Parajo. Optical antennas focus in on biology. *Nat. Photon.*, 2(4):201–203, 2008.

[41] Dario Polli, Piero Altoe, Oliver Weingart, Katelyn M. Spillane, Cristian Manzoni, Daniele Brida, Gaia Tomasello, Giorgio Orlandi, Philipp Kukura, Richard A. Mathies, Marco Garavelli, and Giulio Cerullo. Conical intersection dynamics of the primary photoisomerization event in vision. *Nature*, 467(7314):440–443, September 2010.

[42] Silvia Rinaldi, Federico Melaccio, Samer Gozem, Francesca Fanelli, and Massimo Olivucci. Comparison of the isomerization mechanisms of human melanopsin and invertebrate and vertebrate rhodopsins. *P. Natl. Acad. Sci. USA*, 111(5):1714–1719, February 2014.

[43] Mario Barbatti, Giovanni Granucci, Maurizio Persico, Matthias Ruckenbauer, Mario Vazdar, Mirjana Eckert-Maksić, and Hans Lischka. The on-the-fly surface-hopping program system Newton-X: Application to ab initio simulation of the nonadiabatic photodynamics of benchmark systems. *J. Photochem. Photobiol. A*, 190(2-3):228–240, 2007.

[44] Mario Barbatti, Adélia J. A. Aquino, Jaroslaw J. Szymczak, Dana Nachtigallová, Pavel Hobza, and Hans Lischka. Relaxation mechanisms of UV-photoexcited DNA and RNA nucleobases. *Proc. Natl. Acad. Sci. USA*, 107(50):21453–21458, December 2010.

[45] A. L. Sobolewski, W. Domcke, C. Dedonder-Lardeux, and C. Jouvet. Excited-state hydrogen detachment and hydrogen transfer driven by repulsive $1\pi\sigma^*$ states: A new paradigm for nonradiative decay in aromatic biomolecules. *Phys. Chem. Chem. Phys.*, 4(7):1093–1100, 2002.

[46] A. Raab, G. A. Worth, H. D. Meyer, and L. S. Cederbaum. Molecular dynamics of pyrazine after excitation to the s2 electronic state using a realistic 24-mode model hamiltonian. *J. Chem. Phys.*, 110(2):936, January 1999.

[47] Takuya Horio, Takao Fuji, Yoshi-Ichi Suzuki, and Toshinori Suzuki. Probing ultrafast internal conversion through conical intersection via Time-Energy map of photoelectron angular anisotropy. *J. Am. Chem. Soc.*, 131(30):10392–10393, August 2009.

[48] Thomas A. A. Oliver, Nicholas H. C. Lewis, and Graham R. Fleming. Correlating the motion of electrons and nuclei with two-dimensional electronicvibrational spectroscopy. *P. Natl. A. Sci. USA*, 111(28):10061–10066, July 2014.

[49] B. K. McFarland, J. P. Farrell, S. Miyabe, F. Tarantelli, A. Aguilar, N. Berrah, C. Bostedt, J. D. Bozek, P. H. Bucksbaum, J. C. Castagna, R. N. Coffee, J. P. Cryan, L. Fang, R. Feifel, K. J. Gaffney, J. M. Glownia, T. J. Martinez, M. Mucke, B. Murphy, A. Natan, T. Osipov, V. S. Petrović, S. Schorb, Th Schultz, L. S. Spector, M. Swiggers, I. Tenney, S. Wang, J. L. White, W. White, and M. Gühr. Ultrafast x-ray auger probing of photoexcited molecular dynamics. *Nature Commun.*, 5, June 2014.

[50] Markus Kowalewski, Kochise Bennett, Konstantin E Dorfman, and Shaul Mukamel. Catching conical intersections in the act: Monitoring transient electronic coherences by attosecond stimulated x-ray raman signals. *Physical review letters*, 115(19):193003, 2015.

[51] Henry Timmers, Zheng Li, Niranjan Shivaram, Robin Santra, Oriol Vendrell, and Arvinder Sandhu. Coherent electron hole dynamics near a conical intersection. *Phys. Rev. Lett.*, 113(11), September 2014.

[52] Markus Kowalewski and Shaul Mukamel. Stimulated raman signals at conical intersections: Ab initio surface hopping simulation protocol with direct propagation of the nuclear wave function. *The Journal of Chemical Physics*, 143(4):044117+, July 2015.

[53] H. Tao, T. K. Allison, T. W. Wright, A. M. Stooke, C. Khurmi, J. van Tilborg, Y. Liu, R. W. Falcone, A. Belkacem, and T. J. Martinez. Ultrafast internal conversion in ethylene. i. the excited state lifetime. *J. Chem. Phys.*, 134(24):244306, June 2011.

[54] Serguei Patchkovskii and Michael S. Schuurman. Short-Time dynamics at a conical intersection in High-Harmonic spectroscopy. *J. Phys. Chem. A*, 118(51):12069–12079, December 2014.

[55] Michał A. Kochman, Attila Tajti, Carole A. Morrison, and R. J. Dwayne Miller. Early events in the nonadiabatic relaxation dynamics of 4-(N,N-Dimethylamino)benzonitrile. *J. Chem. Theory Comput.*, 11(3):1118–1128, March 2015.

[56] Y Ding, Z Huang, D Ratner, P Bucksbaum, and H Merdji. Generation of attosecond x-ray pulses with a multicycle two-color enhanced self-amplified spontaneous emission scheme. *Phys. Rev. Top.-Ac.*, 12(6):060703, 2009.

[57] W. Helml, A. R. Maier, W. Schweinberger, I. Grguraš, P. Radcliffe, G. Doumy, C. Roedig, J. Gagnon, M. Messerschmidt, S. Schorb, C. Bostedt, F. Grüner, L. F. DiMauro, D. Cubaynes, J. D. Bozek, Tschentscher Th., J. T. Costello, M. Meyer,

R. Coffee, S. Düsterer, A. L. Cavalieri, and R. Kienberger. Measuring the temporal structure of few-femtosecond free-electron laser x-ray pulses directly in the time domain. *Nat. Photon.*, 8(12):950–957, December 2014.

[58] Paul Arpin Margaret M. Murnane Tenio Popmintchev, Ming-Chang Chen and Henry C. Kapteyn. The attosecond nonlinear optics of bright coherent x-ray generation. *Nat. Photonics*, 4:822–832, Nov 2010.

[59] M Harmand, R Coffee, MR Bionta, M Chollet, D French, D Zhu, DM Fritz, HT Lemke, N Medvedev, B Ziaja, et al. Achieving few-femtosecond time-sorting at hard x-ray free-electron lasers. *Nature Photon.*, 7(3):215–218, 2013.

[60] Ivanka Grguraš, Andreas R Maier, C Behrens, T Mazza, TJ Kelly, P Radcliffe, S Düsterer, AK Kazansky, NM Kabachnik, Th Tschentscher, et al. Ultrafast x-ray pulse characterization at free-electron lasers. *Nature Photon.*, 6(12):852–857, 2012.

[61] Ch Bostedt, JD Bozek, PH Bucksbaum, RN Coffee, JB Hastings, Z Huang, RW Lee, S Schorb, JN Corlett, P Denes, et al. Ultra-fast and ultra-intense x-ray sciences: first results from the linac coherent light source free-electron laser. *J. Phys. B: At. Mol. Opt. Phys.*, 46(16):164003, 2013.

[62] A Laubereau and W Kaiser. Vibrational dynamics of liquids and solids investigated by picosecond light pulses. *Rev. Mod. Phys.*, 50(3):607, 1978.

[63] K. Yoshihara, R. Inaba, H. Okamoto, M. Tasumi, K. Tominaga, and Nelson. K.A. Vibrational and rotational dynamics of molecules in solution studied by femtosecond cars and raman echo. In Wiersma. D.A., editor, *Femtosecond Reaction Dynamics*, pages 299–310. North-Holland, Amsterdam, 1994.

[64] Hadas Frostig, Tim Bayer, Nirit Dudovich, Yonina C. Eldar, and Yaron Silberberg. Single-beam spectrally controlled two-dimensional raman spectroscopy. *Nat. Photon.*, 9(5):339–343, May 2015.

[65] Dmitry Pestov, Xi Wang, Gombojav O Ariunbold, Robert K Murawski, Vladimir A Sautenkov, Arthur Dogariu, Alexei V Sokolov, and Marlan O Scully. Single-shot detection of bacterial endospores via coherent raman spectroscopy. *P. Natl. A. Sci. USA*, 105(2):422–427, 2008.

[66] Joseph D Miller, Sukesh Roy, Mikhail N Slipchenko, James R Gord, and Terrence R Meyer. Single-shot gas-phase thermometry using pure-rotational hybrid femtosecond/picosecond coherent anti-stokes raman scattering. *Opt. Express*, 19(16):15627–15640, 2011.

[67] Clemens Weninger, Michael Purvis, Duncan Ryan, Richard A London, John D Bozek, Christoph Bostedt, Alexander Graf, Gregory Brown, Jorge J Rocca, and Nina Rohringer. Stimulated electronic x-ray raman scattering. *Physical review letters*, 111(23):233902, 2013.

[68] Masayuki Yoshizawa and Makoto Kurosawa. Femtosecond time-resolved raman spectroscopy using stimulated raman scattering. *Phys. Rev. A*, 61:013808, Dec 1999.

[69] Philipp Kukura, David W McCamant, and Richard A Mathies. Femtosecond stimulated raman spectroscopy. *Annu. Rev. Phys. Chem.*, 58:461–488, 2007.

[70] Zhigang Sun, J Lu, Dong H Zhang, and Soo-Y Lee. Quantum theory of (femtosecond) time-resolved stimulated raman scattering. *J. Chem. Phys.*, 128(14):144114, 2008.

[71] Benjamin P Fingerhut, Konstantin E Dorfman, and Shaul Mukamel. Probing the conical intersection dynamics of the rna base uracil by uv-pump stimulated-raman-probe signals; ab initio simulations. *J. Chem. Theo. Comput.*, 10(3):1172–1188, 2014.

[72] F Bencivenga, R Cucini, F Capotondi, A Battistoni, R Mincigrucci, E Giangrisostomi, A Gessini, M Manfredda, IP Nikolov, E Pedersoli, et al. Four-wave mixing experiments with extreme ultraviolet transient gratings. *Nature*, 520(7546):205–208, 2015.

[73] Weijie Hua, Sven Oesterling, Jason D Biggs, Yu Zhang, Hideo Ando, Regina de Vivie-Riedle, Benjamin P Fingerhut, and Shaul Mukamel. Monitoring conical intersections in the ring opening of furan by attosecond stimulated x-ray raman spectroscopy. *Structural Dynamics*, 3(2):023601, 2016.

[74] Wolfgang Domcke, David Yarkony, and Horst Köppel. *Conical intersections: electronic structure, dynamics and spectroscopy*, volume 15. World Scientific, 2004.

[75] Hiroyuki Tamura, Shinkoh Nanbu, Toshimasa Ishida, and Hiroki Nakamura. Ab initio nonadiabatic quantum dynamics of cyclohexadiene/hexatriene ultrafast photoisomerization. *J. Chem. Phys.*, 124(8):084313, February 2006.

[76] Takuya Horio, Takao Fuji, Yoshi-Ichi Suzuki, and Toshinori Suzuki. Probing ultrafast internal conversion through conical intersection via Time-Energy map of photoelectron angular anisotropy. *J. Am. Chem. Soc.*, 131(30):10392–10393, August 2009.

[77] Di Xiao, Ming-Che Chang, and Qian Niu. Berry phase effects on electronic properties. *Rev. Mod. Phys.*, 82(3):1959–2007, July 2010.

[78] Senlin Huang, Yuantao Ding, Zhirong Huang, and Ji Qiang. Generation of stable sub-femtosecond hard x-ray pulses with optimized nonlinear bunch compression. *Physical Review Special Topics-Accelerators and Beams*, 17(12):120703, 2014.

[79] T. A. Carlson. Photoelectron spectroscopy. *Ann. Rev. Phys. Chem.*, 26(1):211–234, 1975.

[80] Albert Stolow, Arthur E. Bragg, and Daniel M. Neumark. Femtosecond Time-Resolved photoelectron spectroscopy. *Chem. Rev.*, 104(4):1719–1758, April 2004.

[81] Henning Meyer. The molecular hamiltonian. *Annu. Rev. Phys. Chem.*, 53(1):141–172, 2002.

[82] Graham A Worth and Lorenz S Cederbaum. Beyond born-oppenheimer: molecular dynamics through a conical intersection. *Annu. Rev. Phys. Chem.*, 55:127–158, 2004.

[83] Jr-Wei Ho, Hung-Chien Yen, Wei-Kuang Chou, Chih-Nan Weng, Li-Hao Cheng, Hui-Qi Shi, Szu-Hsueh Lai, and Po-Yuan Cheng. Disentangling intrinsic ultrafast Excited-State dynamics of cytosine tautomers. *J. Phys. Chem. A*, 115(30):8406–8418, June 2011.

[84] Alexis L. Thompson and Todd J. Martinez. Time-resolved photoelectron spectroscopy from first principles: Excited state dynamics of benzene. *Faraday Discuss.*, 150(0):293–311, 2011.

[85] M. Hentschel, R. Kienberger, Ch Spielmann, G. A. Reider, N. Milosevic, T. Brabec, P. Corkum, U. Heinzmann, M. Drescher, and F. Krausz. Attosecond metrology. *Nature*, 414(6863):509–513, November 2001.

[86] P. von den Hoff, R. Siemering, M. Kowalewski, and R. de Vivie-Riedle. Electron dynamics and its control in molecules: From diatomics to larger molecular systems. *Selected Topics in Quantum Electronics, IEEE Journal of*, 18(1):119–129, January 2011.

[87] Konstantin E. Dorfman, Kochise Bennett, and Shaul Mukamel. Detecting electronic coherence by multidimensional broadband stimulated x-ray raman signals. *Phys. Rev. A*, 92(2), August 2015.

[88] Markus Kowalewski, Kochise Bennett, Konstantin E. Dorfman, and Shaul Mukamel. Catching conical intersections in the act: Monitoring transient electronic coherences by attosecond stimulated X-Ray raman signals. *Phys. Rev. Lett.*, 115:193003, 2015.

[89] Matthias Seel and Wolfgang Domcke. Model studies on femtosecond time-resolved ionization spectroscopy of excited-state vibrational dynamics and vibronic coupling. *Chem. Phys.*, 151(1):59–72, 1991.

[90] Susanne Hahn and Gerhard Stock. Efficient calculation of femtosecond time-resolved photoelectron spectra: method and application to the ionization of pyrazine. *Phys. Chem. Chem. Phys.*, 3(12):2331–2336, 2001.

[91] Thomas S Kuhlman, William J Glover, Toshifumi Mori, Klaus B Møller, and Todd J Martínez. Between ethylene and polyenes-the non-adiabatic dynamics of cis-dienes. *Faraday Discuss.*, 157:193–212, 2012.

[92] Peter Trabs, Franziska Buchner, Masood Ghotbi, Andrea Lübcke, Hans-Hermann Ritze, Marc J. J. Vrakking, and Arnaud Rouzée. Time-, angle- and kinetic-energy-resolved photoelectron spectroscopy of highly excited states of NO. *J. Phy. B: At. Mol. Opt. Phys.*, 47(12):124016, June 2014.

[93] Kochise Bennett, Markus Kowalewski, and Shaul Mukamel. Nonadiabatic dynamics may be probed through electronic coherence in time-resolved photoelectron spectroscopy. *Journal of chemical theory and computation*, 2015.

[94] Xiyi Chen and Stephen E Bradforth. The ultrafast dynamics of photodetachment. *Annu. Rev. Phys. Chem.*, 59:203–231, 2008.

[95] Jingtao Zhang and Takashi Nakajima. Influence of coulomb potential for photoionization of h atoms in an elliptically polarized laser field: Velocity gauge versus length gauge. *Phys. Rev. A*, 77(4):043417, April 2008.

[96] M. Ben-Nun, Jason Quenneville, and Todd J. Martínez. Ab initio multiple spawning: photochemistry from first principles quantum molecular dynamics. *J. Phys. Chem. A*, 104(22):5161–5175, May 2000.

[97] Sharon Hammes-Schiffer and John C. Tully. Proton transfer in solution: Molecular dynamics with quantum transitions. *J. Chem. Phys.*, 101(6):4657–4667, September 1994.

[98] Saar Rahav and Shaul Mukamel. Multidimensional attosecond photoelectron spectroscopy with shaped pulses and quantum optical fields. *Phys. Rev. A*, 81(6):063810, 2010.

[99] David J. Tannor. *Introduction to Quantum Mechanics: A Time-Dependent Perspective.* University Science Books, October 2006.

[100] C. Melania Oana and Anna I. Krylov. Dyson orbitals for ionization from the ground and electronically excited states within equation-of-motion coupled-cluster formalism: Theory, implementation, and examples. *J. Chem. Phys.*, 127(23):234106, December 2007.

[101] Wolfgang Domcke, David R. Yarkony, and Horst Köppel. *Conical Intersections*, volume 17. WORLD SCIENTIFIC, November 2011.

[102] M. Kowalewski, J. Mikosch, R. Wester, and R. de Vivie-Riedle. Nucleophilic substitution dynamics: Comparing wave packet calculations with experiment. *J. Phys. Chem. A*, 118:4661–4669, June 2014.

[103] Benjamin P. Fingerhut, Dorothee Geppert, and Regina de Vivie-Riedle. Ultrafast dissociation pathways of diphenylmethyl chloride to generate reactive carbo cations. *Chem. Phys.*, 343(2-3):329–339, January 2008.

[104] Philipp von den Hoff, Sebastian Thallmair, Markus Kowalewski, Robert Siemering, and Regina de Vivie-Riedle. Optimal control theory - closing the gap between theory and experiment. *Phys. Chem. Chem. Phys.*, 14:14460, 2012.

[105] Hans-Dieter Meyer. Studying molecular quantum dynamics with the multiconfiguration time-dependent hartree method. *WIREs Comput. Mol. Sci.*, 2(2):351–374, March 2012.

[106] Raoul Bourquin, Vasile Gradinaru, and George A. Hagedorn. Non-adiabatic transitions near avoided crossings: theory and numerics. *J. Math. Chem.*, 50(3):602–619, April 2012.

[107] H. Köppel, W. Domcke, and L. S. Cederbaum. Multimode molecular dynamics beyond the Born-Oppenheimer approximation. 57:59–246, 1984.

[108] Alexander Humeniuk, Matthias Wohlgemuth, Toshinori Suzuki, and Roland Mitrić. Time-resolved photoelectron imaging spectra from non-adiabatic molecular dynamics simulations. *J. Chem. Phys.*, 139(13):134104, October 2013.

[109] Brian R. Landry and Joseph E. Subotnik. How to recover marcus theory with fewest switches surface hopping: Add just a touch of decoherence. *J. Chem. Phys.*, 137(22):22A513, December 2012.

[110] Giovanni Granucci, Maurizio Persico, and Alberto Zoccante. Including quantum decoherence in surface hopping. *J. Chem. Phys.*, 133(13):134111, October 2010.

[111] Günter Käb. Fewest switches adiabatic surface hopping as applied to vibrational energy relaxation†. *J. Phys. Chem. A*, 110(9):3197–3215, March 2006.

[112] Craig C. Martens. Communication: Fully coherent quantum state hopping. *J. Chem. Phys.*, 143(14):141101, October 2015.

[113] A. M. D. Lee, J. D. Coe, S. Ullrich, M. L. Ho, S. J. Lee, B. M. Cheng, M. Z. Zgierski, I. C. Chen, T. J. Martinez, and Albert Stolow. Substituent effects on dynamics at conical intersections: ,-Enones. *J. Phys. Chem. A*, 111(47):11948–11960, November 2007.

[114] H.-J. Werner, P. J. Knowles, G. Knizia, F. R. Manby, M. Schütz, et al. Molpro, version 2010.1, a package of ab initio programs, 2010. see http://www.molpro.net.

Appendix A

Rate-of-Change of Photon Number

From the field point-of-view, perhaps the simplest starting point from which to derive expressions for the various spectroscopic signals, is to suppose that we detect the integrated rate of change of the photon number operator in some "signal" mode

$$S(\Lambda) = \int dt \langle \frac{d\hat{N}_{\mathrm{s}}}{dt} \rangle (t) = i[\hat{H}, \hat{N}_{\mathrm{s}}] = i[\hat{H}_{\mathrm{I}}, \hat{N}_{\mathrm{s}}] \tag{A.1}$$

where Λ stands for the set of parameters that define the externally applied field and we have used Heisenberg's equation of motion and the fact that $\hat{N}$ fails to commute only with the interaction part of the Hamiltonian. This definition of the signal corresponds to detecting the frequency-dispersed gain/loss. Using the mode-expansion of the electric field

$$\hat{\mathbf{E}}(t) = i \sum_{\mathbf{k}\lambda} \sqrt{\frac{2\pi\hbar\omega_{\mathbf{k}}}{\mathcal{V}}} \epsilon^{(\lambda)}(\hat{\mathbf{k}}) e^{-i\omega t} \hat{a}_{\mathbf{k},\lambda} + \mathrm{H.c.} \equiv \hat{\mathbf{E}}^{(+)}(t) + \hat{\mathbf{E}}^{(-)}(t), \tag{A.2}$$

where "H.c." stands for the Hermitian conjugate and we have split the field into its positive and negative frequency components, this commutator is evaluated to be

$$S(\Lambda) = -\Im[\int dt\langle \hat{\mathbf{E}}^{(-)}_{\mathbf{k}_s}(t) \cdot \hat{\mathbf{V}}(t)\rangle]. \tag{A.3}$$

It is possible to derive an equivalent expression from the matter point-of-view, computing the rate of change of the molecular energy. There are two reasons we prefer the field perspective. First, there are certain techniques for which the signal emitted at the source is not identical to the observed signal (what is emitted is not the same as what is detected). In these cases, post-emission effects must be taken into account and this is best handled from the field-perspective. Although this type of situation is more common for electronic spectroscopies (in which electrons rather than photons are detected), detector gating and sensitivity functions, for example, require such extensions. A second and more fundamental reason is philosophical: it is the fields that are ultimately detected so it is the field operators that should taken to be directly connected to the observable quantities such as spectroscopic signals.

We have yet to discuss the state of the electromagnetic field and Eq. (A.3) is sufficiently general to accomodate signals that utilize quantum states of light. In this manuscript however, we will only concern ourselves with heterodyne-detected (or stimulated) signals, in which the light may be taken as classical, and homodyne-detected (or spontaneous) signals, in which the signal mode of the elctromagnetic field is initially in the vacuum state $|0\rangle$. We explore these two types of signals below.

A.0.1 Heterodyne-Detected (Stimulated) Signals

When considering the photon gain/loss of externally applied laser beams or pulses, it is permissible to take the field to be in a coherent state (i.e., an eigenstate of $\hat{a}$). This then reduces the signal to

$$S(\Lambda) = -\Im[\int dt\mathbf{E}^{(-)}_{\mathbf{k}_\mathrm{s}}(t)\cdot\langle\hat{\mathbf{V}}(t)\rangle] = -\,\Im[\int dt\mathbf{E}(\mathbf{k}_\mathrm{s})e^{i\omega_\mathrm{s}t}\cdot\langle\hat{\mathbf{V}}(t)\rangle] = \tag{A.4}$$

$$-\Im[\mathbf{E}(\mathbf{k}_\mathrm{s})\cdot\langle\hat{\mathbf{V}}(\omega_s)\rangle].$$

In the main text, we will take the externally applied fields to be paraxial and collinear so that the wavevector dependence may be replaced by the frequency. Either of the final two expressions may be preferred for simulation purposes depending on whether the time- or frequency-domain dipole expectation-value is more readily calculable. For example, in atomic or static molecular spectra, the frequency domain is most easily computed. In the more complex molecular calculations wherein the nuclear-dependencies and NACs play a significant role, the dynamics may be sufficiently complicated that it is difficult to propogate for the long times necessary for a numeric evaluation of the Fourier Transform. Fortunately, we will ordinarily be interested in temporally-limited interactions. The field envelopes can then be used to limit the necessary extent of temporal propagation. Importantly, this approach is not applicable to spontaneous signals since the emission event is not controlled.

Appendix B

Simulation Protocols for TRPES

In section 4.4 and Fig. 4.3, we used two different simulation protocols for TRPES with the same model and initial conditions. These protocols, based on Eq. (4.5) and Eq. (4.11) respectively, both propagate the full nuclear+electronic wavefunction quantum mechanically. In this appendix, we will explain in greater detail these two simulation procedures.

B.1 Correlation Function Expression

The photoelectron signal is defined as the energy-resolved, integrated rate of change of the number of photoelectrons which gives the total energy-resolved photoelectron yield

$$S(\varepsilon_{\mathbf{p}}, t_{\mathrm{d}}) = \int dt \frac{d}{dt} \langle \hat{n}_{\mathbf{p}}(t) \rangle. \tag{B.1}$$

It depends on photoelectron energy $\varepsilon_{\mathbf{p}}$ and the delay time t_{d} of the x-ray pulse relative to state preparation. The signal that we derive generally depends on all parameters describing the ionizing pulse and can be manipulated by pulse shaping but for simplicity we only explicitly state the t_{d} dependence. Assuming that the photoelectrons are generated only by interaction with the x-ray pulse (that is, $[\hat{n}_{\mathbf{p}}, \hat{H}_{\mathrm{M}}] = 0$ where $\hat{n}_{\mathbf{p}} = \hat{c}^{\dagger}_{\mathbf{p}}\hat{c}_{\mathbf{p}}$ is the occupation number of the photoelectron state $|\mathbf{p}\rangle$), we have, from the Heisenberg equation of motion

$$\dot{\hat{n}}_{\mathbf{p}} = -i[\hat{n}_{\mathbf{p}}, H] = -iE_{\mathrm{x}}(t)\left(\hat{\mu}_{\mathbf{p}} - \hat{\mu}^{\dagger}_{\mathbf{p}}\right) , \tag{B.2}$$

where the operator

$$\hat{\mu}_{\mathbf{p}} \equiv \sum_{\alpha a} \hat{\mu}^{\dagger}_{\alpha a}\hat{c}_{\mathbf{p}}|a\rangle\langle\alpha| \tag{B.3}$$

annihilates a photoelectron and returns the molecule to an unionized state.

We will carry out the calculation in Hilbert space since we have an eye toward numerical propagation of the nuclear+electronic wavefunction. We note however that a Liouville space treatment would facilitate the incorporation of environmental degrees of freedom (spectator nuclear modes can also be treated at this level) [36]. For simplicity, we will not explicitly incorporate the pumping process but rather take the system to be prepared in a known non-stationary state at time τ_0. Since the initial state of the photoelectron is the vacuum $|0\rangle$, the expectation values in Eq. (B.2) vanishes to first order in E_{x}. Under the assumption that the ionizing x-ray pulse is well-separated temporally from the preparation process, we may expand the signal to second order in the interaction Hamiltonian to obtain

$$S_{\mathrm{e}}(\varepsilon_{\mathbf{p}}, t_{\mathrm{d}}) = \int dt \int dt' \theta(t-t') E_{\mathrm{x}}(t) E_{\mathrm{x}}(t') \left(\langle \hat{\mu}_{\mathbf{p}}(t)\hat{\mu}^{\dagger}_{\mathbf{p}}(t')\rangle_0 + \langle \hat{\mu}_{\mathbf{p}}(t')\hat{\mu}^{\dagger}_{\mathbf{p}}(t)\rangle_0\right) \tag{B.4}$$

which may also be read directly from the diagrams in Fig. 4.1. Switching $t \mapsto t'$ in the second term then yields

$$S_{\mathrm{e}}(\varepsilon_{\mathbf{p}}, t_{\mathrm{d}}) = \int dt \int dt' E_{\mathrm{x}}(t) E_{\mathrm{x}}(t') \langle \hat{\mu}_{\mathbf{p}}(t)\hat{\mu}^{\dagger}_{\mathbf{p}}(t')\rangle_0 \,. \tag{B.5}$$

Since the photoelectron and the molecular Hamiltonians commute, we may factor the expectation value and evaluate the photoelectron part yielding Eqn. (4.5), which may also be written in the frequency domain as

$$S_{\mathrm{e}}(\varepsilon_{\mathbf{p}}, T) = \int\int \frac{d\omega d\omega'}{4\pi^2} \tilde{E}^*_{\mathrm{x}}(\omega)\tilde{E}_{\mathrm{x}}(\omega')\langle\hat{\mu}(\omega + \omega_x - \varepsilon_{\mathbf{p}})\hat{\mu}^\dagger(\omega' + \omega_x - \varepsilon_{\mathbf{p}})\rangle_0\,, \tag{B.6}$$

where we have substituted the temporal field envelopes for their Fourier transforms

$$\tilde{E}_{\mathrm{x}}(t) = \int \frac{d\omega}{2\pi}\tilde{E}_{\mathrm{x}}(\omega)e^{-i\omega t} \tag{B.7}$$

and the conjugate relation for $\tilde{E}^*_{\mathrm{x}}(t)$. The first simulation protocol is based on Eqn. (4.5) and directly propagates the total nuclear+electronic wavefunction. Thus, we begin with the initial state $|\Psi_0\rangle = |\phi_0\rangle \otimes |1\rangle$ and propagate to some $t_{\max}$ in units of δt (we used $\delta t = 6t_h \approx 120$as) via the Lanczos algorithm. This therefore generates a list of wavefunctions

$$|\Psi_{12}(t)\rangle \equiv e^{-i\hat{H}_{\mathrm{M}}t}|\Psi_0\rangle \qquad 0 < t < t_{\max} \tag{B.8}$$

where the "12" subscript emphasizes that, since the system begins in state $|1\rangle$ and $\hat{H}_{\mathrm{M}}$ doesn't couple neutral and ionized electronic states, the propagation is entirely in the manifold of nuclear electronic states. For time t, $0 < t < t_{\max}$, we apply the dipole operator, thus generating a list,

$$\hat{\mu}^\dagger|\Psi_{12}(t)\rangle \qquad 0 < t < t_{\max}, \tag{B.9}$$

of the total wavefunction following dipole excitation at time t. In our simulations, we take the dipole operator to be merely map the wavepackets on the neutral surfaces directly to the ionic surface. Thus,

$$\hat{\mu}^\dagger = \sum_{a=1,2}|3\rangle\langle a| \Rightarrow \hat{\mu}^\dagger|\Psi_{12}(t)\rangle = |\phi_{12}(t)\rangle \otimes |3\rangle \tag{B.10}$$

in our model. The correlation function relevant for the TRPES signal is

$$\langle\hat{\mu}(t)\hat{\mu}^\dagger(t')\rangle = \langle\phi_{12}(t)|e^{-i\hat{\varepsilon}_3(t-t')}|\phi_{12}(t')\rangle \tag{B.11}$$

Since the action of the $\hat{\mu}$'s ionizes the system, the remaining exponential propagates the nuclear wavepacket along the ionized surface for time $t-t'$. For every time t', $0 < t' < t_{\max} - \delta T$, we therefore generate a matrix of propagated wavepackets

$$|\phi_3(t,t')\rangle = e^{-i\hat{\varepsilon}_3(t-t')}|\phi_{12}(t')\rangle \qquad t' - \delta T < t < t' + \delta T \tag{B.12}$$

representing propagation in the unionized manifold up to time t' and then in the ionized manifold from t' to t (with no restriction on the relative order of t, t'). The restriction $|t-t'| < \delta T$ speeds up the calculation and is valid because the electric field factors $E_{\mathrm{x}}(t^{(\prime)})$ restrict t to be near t' for temporally limited pulses. In our propagation, we used $\delta T = 30$fs for a Gaussian field envelope of $\sigma_{\mathrm{x}} = 2.5$fs. We now obtain the original correlation function by taking the inner product

$$\langle\hat{\mu}(t)\hat{\mu}^\dagger(t')\rangle = \langle\phi_{12}(t)|\phi_3(t,t')\rangle. \tag{B.13}$$

Multiplying this quantity by the field factors defines a two-time function

$$K(t,t') \equiv E_{\mathrm{x}}(t)E_{\mathrm{x}}(t')\langle\phi_{12}(t)|\phi_3(t,t')\rangle \tag{B.14}$$

and the evaluation of the TRPES signal (Eq. (4.5)) amounts to a 2D Fourier Transform of this function (actually, a "diagonal" subset of the transformed function $\tilde{K}(\Omega,\Omega')$ in which $\Omega = -\Omega'$). We thus have

$$S(\varepsilon_{\mathbf{p}},T) = K(\varepsilon_{\mathbf{p}} - \omega_x, \omega_x - \varepsilon_{\mathbf{p}}) \tag{B.15}$$

which depends on time parametrically through the transformed electric field factors. It is this result that is displayed as the S_e in Fig. 4.3. This same basic procedure was also used to generate the S_e^{pop} of Fig. 4.3 except that coherences were projected out.

B.1.1 Semiclassical and Quasistatic FGR

From Eqn. (4.8), we make the variable substitutions $\tau = t - t'$, $\bar{t} = \frac{1}{2}(t + t')$ to obtain

$$\begin{aligned} S_{\mathrm{e}}(\varepsilon_{\mathbf{p}}, T) = \int\!\!\int \frac{d\omega d\omega'}{2\pi^2} \int d\bar{t} \int d\tau \tilde{\mathcal{E}}_{\mathrm{x}}^*(\omega) \tilde{\mathcal{E}}_{\mathrm{x}}(\omega') e^{-i(\varepsilon_{\mathbf{p}} - \omega_{\mathrm{x}} - \frac{\omega+\omega'}{2})\tau} e^{i(\omega-\omega')\bar{t}} \\ \times \Bigg(\sum_{a\alpha} \langle \hat{M}_{a0}^*(\bar{t} + \frac{1}{2}\tau) \hat{\mu}_{\alpha a} \hat{M}_{\alpha\alpha}(\tau) \hat{\mu}_{\alpha a}^\dagger \hat{M}_{a0}(\bar{t} - \frac{1}{2}\tau) \rangle_{\phi_0} \\ + \sum_{a \neq b, \alpha} \langle \hat{M}_{b0}^*(\bar{t} + \frac{1}{2}\tau) \hat{\mu}_{\alpha b} \hat{M}_{\alpha\alpha}(\tau) \hat{\mu}_{\alpha a}^\dagger \hat{M}_{a0}(\bar{t} - \frac{1}{2}\tau) \rangle_{\phi_0} \Bigg). \end{aligned} \tag{B.16}$$

In order to simplify the exact transition amplitudes introduced above, we will take the nuclei to be static and neglect the nuclear kinetic energy during the interaction with the ionizing pulse. We term this the quasistatic approximation. For the middle propagators in Eq. (B.16), the implications are clear and we may write

$$\hat{M}_{\alpha\alpha}(\tau) \mapsto e^{-i\hat{\varepsilon}_\alpha \tau}. \tag{B.17}$$

To handle the remaining transition amplitudes, we propagate under the full Hamiltonian up to the delay time t_{d} and then under the quasistatic approximation. We thus shift the integration $\bar{t} \mapsto \bar{t} + T$ and write

$$\hat{M}_{a0}(t_{\mathrm{d}} + \bar{t} \pm \frac{1}{2}\tau) = \hat{M}_{aa}(\bar{t} \pm \frac{1}{2}\tau) \hat{M}_{a0}(t_{\mathrm{d}}) = e^{-i\hat{\varepsilon}_a(\bar{t} \pm \frac{1}{2}\tau)} \hat{M}_{a0}(t_{\mathrm{d}}) \tag{B.18}$$

where the first equality follows from neglecting the adiabatic coupling after propagation to t_{d} and the second equality comes directly from neglecting the $\hat{T}$ terms in $\hat{H}_{\mathrm{M}}$. Inserting this into Eq. (B.16), we obtain

$$\begin{aligned} S(\varepsilon_{\mathbf{p}}, T) = \int\!\!\int \frac{d\omega d\omega'}{2\pi^2} \int d\bar{t} \int d\tau \tilde{\mathcal{E}}_{\mathrm{x}}^*(\omega) \tilde{\mathcal{E}}_{\mathrm{x}}(\omega') e^{-i(\varepsilon_{\mathbf{p}} - \omega_{\mathrm{x}} - \frac{\omega+\omega'}{2})\tau} e^{i(\omega-\omega')(\bar{t}+T)} \\ \times \Bigg(\sum_{a\alpha} \langle \hat{M}_{a0}^*(T) e^{i\hat{\varepsilon}_a(\bar{t}+\frac{1}{2}\tau)} \hat{\mu}_{\alpha a} e^{-i\hat{\varepsilon}_\alpha \tau} \hat{\mu}_{\alpha a}^\dagger e^{-i\hat{\varepsilon}_a(\bar{t}-\frac{1}{2}\tau)} \hat{M}_{a0}(T) \rangle_{\phi_0} \\ + \sum_{a\neq b,\alpha} \langle \hat{M}_{b0}^*(T) e^{i\hat{\varepsilon}_b(\bar{t}+\frac{1}{2}\tau)} \hat{\mu}_{\alpha b} e^{-i\hat{\varepsilon}_\alpha \tau} \hat{\mu}_{\alpha a}^\dagger e^{-i\hat{\varepsilon}_a(\bar{t}-\frac{1}{2}\tau)} \hat{M}_{a0}(T) \rangle_{\phi_0} \Bigg) . \end{aligned} \tag{B.19}$$

To carry out the $\bar{t}$ and τ integrations, we now formally act with the transition amplitudes on the initial nuclear wavepacket. This propagates the nuclear wavepacket to time t_{d}. We then take the nuclear wavepacket as frozen for the integrations, allowing us to replace the ε's with their expectation values over the frozen wavepacket.

$$\hat{M}_{a0}(t_{\mathrm{d}}) |\phi_0\rangle = c_a(t_{\mathrm{d}}) |\phi_a(t_{\mathrm{d}})\rangle \tag{B.20}$$

with $c_a(t)$ the time-dependent propability amplitude associated with electronic state $|a\rangle$ and $\phi_a(t_{\mathrm{d}})$ the nuclear wavepacket on electronic surface a at time T and replace the adiabatic potentials with

$$\begin{aligned} \varepsilon_a(t_{\mathrm{d}}) \equiv \langle \phi_a(t_{\mathrm{d}}) | \hat{\varepsilon}_a | \phi_a(t_{\mathrm{d}}) \rangle \\ \varepsilon_\alpha(t_{\mathrm{d}}) \equiv \langle \phi_{\alpha a}(t_{\mathrm{d}}) | \hat{\varepsilon}_\alpha | \phi_{\alpha a}(t_{\mathrm{d}}) \rangle. \end{aligned} \tag{B.21}$$

The second equation follows upon defining the nuclear wavepacket after dipolar excitation

$$\hat{\mu}_{\alpha a}^\dagger |\phi_a(t_{\mathrm{d}})\rangle \equiv \mu_{\alpha a}^*(t_{\mathrm{d}}) |\phi_{\alpha a}(t_{\mathrm{d}})\rangle. \tag{B.22}$$

Such an expression is possible to write because the dipole operator $\hat{\mu}_{\alpha a}^\dagger$ simply maps the original nuclear wavefunction $|\phi_a(t_{\mathrm{d}})\rangle$ to a new wavefunction $|\phi_{\alpha a}(t_{\mathrm{d}})\rangle$, the details of which reflect the dependence of the dipole on the nuclear coordinates. The time-dependence of the resulting c-number $\mu^*_{\alpha a}$ is necessary since the dipole is not unitary and the transformed nuclear wavefunction has a time-dependent normalization which is absorbed into the $\mu^*_{\alpha a}$. Thus, in this approximation, the vibronic states can be altered by the dipole operator but not by the time propagators. Note that if, as in the Condon approximation, the nuclear wavefunction is unaffected by the electronic dipole operator, we have $|\phi_{\alpha a}(t_{\mathrm{d}})\rangle = |\phi_a(t_{\mathrm{d}})\rangle$ and $\mu^*_{\alpha a}(t_{\mathrm{d}}) = \mu^*_{\alpha a}$ and things simplify somewhat. Inserting Eqs. (B.20)-(B.22) into (B.19), we may now carry out the time integrations since all operators have been replaced by their expectation values yielding Eqn. (4.10).

The second simulation protocol used is based on Eq. (4.11). We first note that our uniform dipole operator in the Condon approximation allows us to drop the $\mu_{\alpha a}$ factor. Using the same list

$$|\Psi_{12}(t)\rangle \equiv e^{-i\hat{H}_{\mathrm{M}}t}|\Psi_0\rangle \qquad 0 < t < t_{\max} \tag{B.23}$$

generated in the first protocol, we project onto a neutral state $|a\rangle$, defining

$$\langle a|\Psi_{12}(t)\rangle = c_a(t)|\phi_a(t)\rangle \tag{B.24}$$

in accordance with Eq. (B.20). We now take expectation values of the electronic energies over this nuclear wavepacket

$$\begin{aligned} \langle\phi_a(t)|\hat{\varepsilon}_a|\phi_a(t)\rangle &\equiv \varepsilon_a(t) \\ \langle\phi_a(t)|\hat{\varepsilon}_\alpha|\phi_a(t)\rangle &\equiv \varepsilon_\alpha(t). \end{aligned} \tag{B.25}$$

Combined with the populations $|c_a(t)|^2$, these expectation values are then all the ingredients to Eqs. (4.11), (4.12), and therefore (4.10). For the ionizing field amplitude profile $E_{\mathrm{x}}(\omega)$, we use a Gaussian spectral field envelope of width $\sigma_\omega^{-1} \approx 2.5$fs for comparison to the temporal field envelope used in the previous section. We thereby generate the qspFGR of Fig. 4.3. Note that both simulation protocols begin with the same wave function propagated in the neutral manifold. This propagation is what generates the coherences that lead to the oscillations in the photoelectron signal. The correlation-function protocol also requires propagation in the ionized manifold as well as including electronic coherences which are omitted in the qsFGR (the quasistatic assumption).

Appendix C

Model Systems for Nuclear Dynamics

In this appendix, we collect the paremeters defining the models used to simulate nuclear dynamics in chapters 3 and 4.

C.0.2 1D-Model System

To show the basic features of nuclear dynamics, we use a simple, harmonic 1-dimensional model. The diabatic potential energy curves are given by two displaced parabolas. As always, all quantities are given in atomic units ($\hbar = m_e = 4\pi\epsilon_0 = 1$).

$$H_1 = \frac{1}{2} 0.01 \left(x - 0.2\right)^2 \tag{C.1}$$

$$H_2 = \frac{1}{2} 0.01 \left(x + 0.2\right)^2 \tag{C.2}$$

The diabatic coupling is given by a Gaussian function

$$H_{12} = 0.01 \exp\left(-x^2\right) , \tag{C.3}$$

Table C.1: Parameters for the Polynomial expansions of the diabatic states of the two dimensional model. and couplings (given in atomic units).

Surf.	c_{00}	c_{10}	c_{01}	c_{20}	c_{11}	c_{02}	c_{30}	c_{21}	c_{12}	c_{03}
H_1	-0.001854	-0.02817	-0.114	0.3156	-0.1576	0.2457	0.1237	0.2883	-0.2856	0.1071
H_2	-0.001247	0.01804	0.02297	0.4546	-0.2419	0.2242	0.2404	0.1135	-0.3448	0.07928
H_{12}	0.0006653	-0.05699	-0.001481	-0.02017	-0.06204	0.02157	0.06652	0.05527	0.04719	0.02031

representing an avoided crossing. The reduced mass of the system is assumed to be $m = 5100$. The wave packet simulations and the signal calculation is analogous to the two-dimensional model described in appendix C.1.

C.0.3 2D Model System

For the TRUECARS signal, we use a two-dimensional model system inspired by the S_2-S_1 CI in acrolein [113]. The system has been chosen as a role model to obtain realistic parameters for the energy splittings between the PESs and the couplings. The adiabatic and diabatic states were calculated in the vinicinty of the CI with the program package MOLPRO [114] at the CASSCF(6/5)/6-31+G* level of theory. The two coordinates of the system, x_h and x_g, correspond to the orthonormal versions of the derivative coupling vector and the gradient difference vector respectively. The diabatic potential energy surfaces and the diabatic couplings have been calculated on a 9×9 grid with maximum displacements of ±0.4. The CI is located at the origin of the coordinate system. The resulting data is fitted to a third order polynomial:

$$f(x_h, x_g) = c_{00}+c_{10}x_h+c_{01}x_g+c_{20}x_h^2+c_{11}x_hx_g+c_{02}x_g^2+c_{30}x_h^3+c_{21}x_h^2x_g+c_{12}x_hx_g^2+c_{03}x_g^3 \quad \text{(C.4)}$$

The respective parameter sets c_{ij} for H_1, H_2 and H_{12} are given in tab. C.2. The polynomial allows for extrapolation of the data to a wider parameter range, necessary to run the wave packet simulations. The resulting diabatic surfaces, denoted by H_1 and H_2, are shown in Fig. C.1. The diabatic coupling H_{12} is created by eq. C.4 and shaped by gaussian functions.

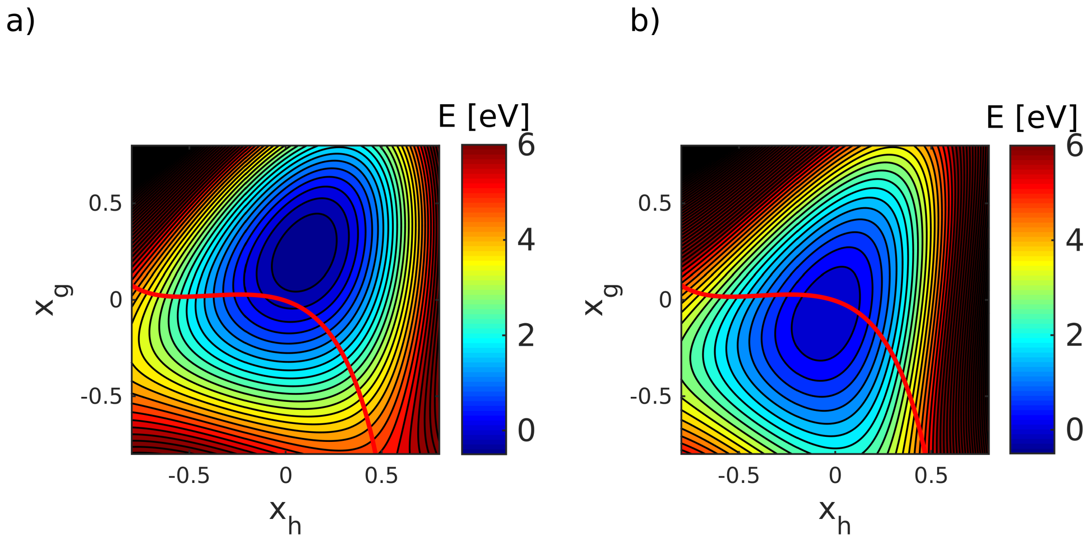

Figure C.1: Diabatic potential energy surfaces a) H_1 and b) H_2. The conical intersection is in the center of the coordinate system. The red line indicates the intersection between both surfaces in the diabatic representation.

$$H_{12} = f(x_h, x_g) h(x_h) \exp\left(\frac{-x_g^2}{0.08}\right) \tag{C.5}$$

where $h(x_h)$ is

$$h(x_h) = \begin{cases} \exp\left(-\dfrac{x_h^2}{0.18}\right) & x_h < 0 \\ \exp\left(-\dfrac{x_h^2}{0.045}\right) & x_h \geq 0 \end{cases} \tag{C.6}$$

The Gaussian envelope lets the diabatic coupling term vanish in areas far from the CoIn and diabatic states become identical to the adiabatic states. The resulting coupling function is shown in Fig. C.2. The corresponding adiabatic PESs are readily obtained by diagonalization of the diabatic surfaces (Fig. C.3).

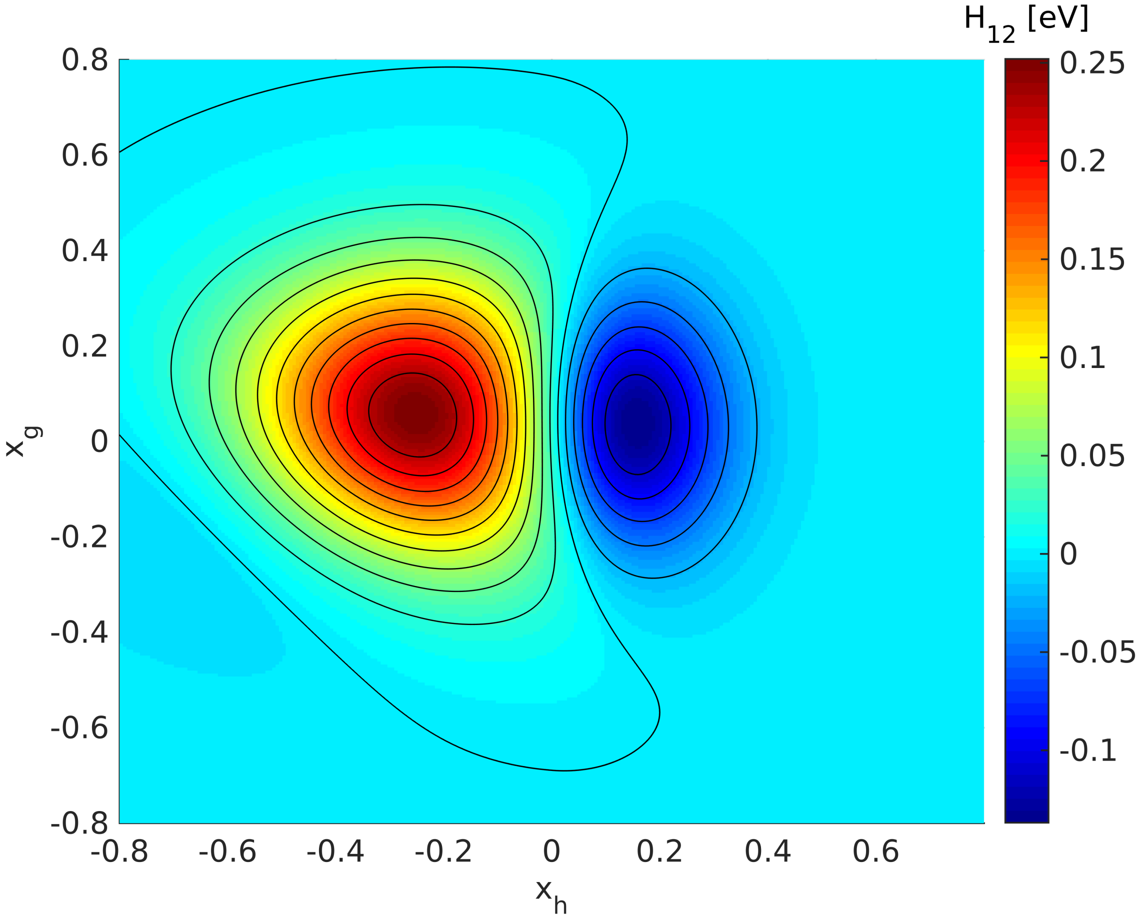

Figure C.2: Contourplot of the diabatic coupling element H_{12}.

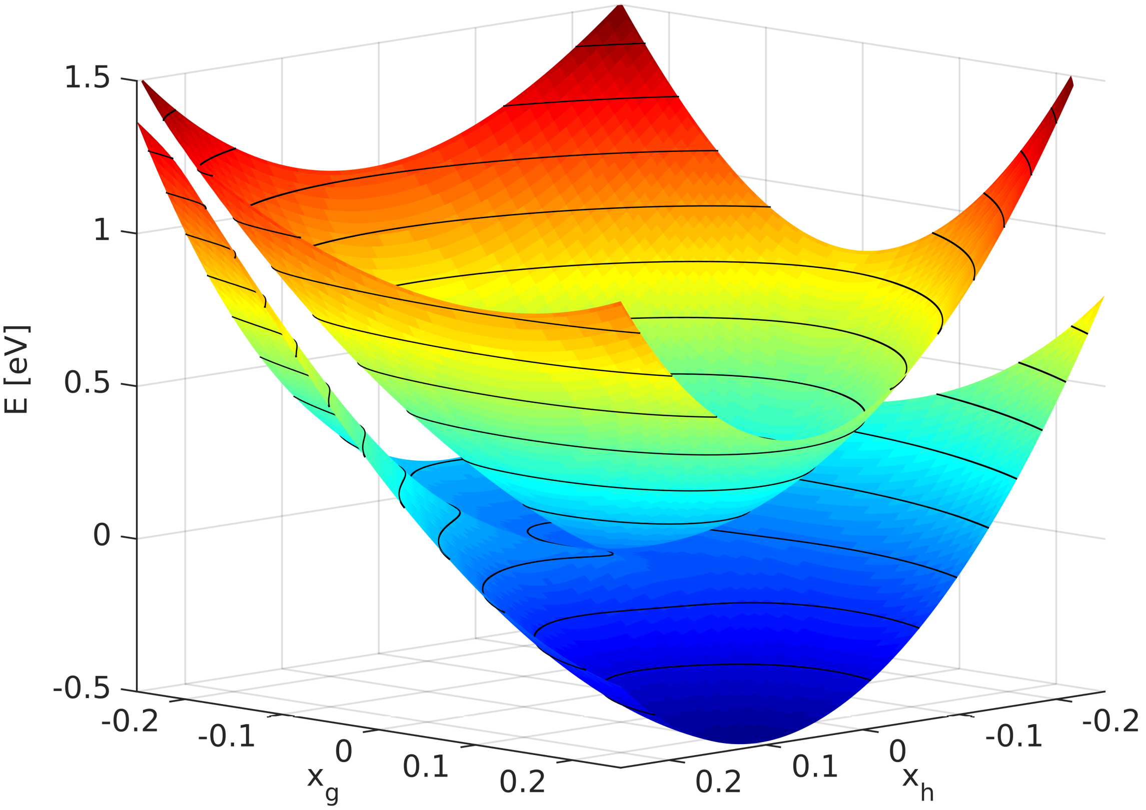

Figure C.3: Adiabatic potential energy surfaces. The conical intersection is in the center of the coordinate system.

C.1 Vibronic Wave Packet Simulations

The wave packet simulations are carried out on the diabatic surfaces by solving the time dependent Schrödinger equation numerically on a position space grid by the Fourier method [99]. The corresponding Hamiltonian in the diabatic representation reads:

$$H = -\mathbb{1}\frac{1}{2m}\sum_{i\in\{h,g\}}\frac{\mathrm{d}^2}{\mathrm{d}x_i^2} + \begin{pmatrix} H_1(x) & H_{12}(x) \\ H_{12}(x) & H_2(x) \end{pmatrix} \tag{C.7}$$

where the reduced mass m is 30000 au ($\approx$ 16 amu) for both coordinates and $x = (x_h, x_g)$. The time stepping

$$\psi(x, t+\Delta t) = \exp\left(-iH\Delta t\right)\psi(x,t)\,, \tag{C.8}$$

is calculated with the Short Iterative Lanczos (SIL) method [99], and a step size of $\Delta t = 4\,\mathrm{au}$ ($\approx 100\,\mathrm{as}$). The corresponding diabatic wave function is expressed in terms of the electronic states:

$$\psi(x,t) = \begin{pmatrix} \phi_1(x,t) \\ \phi_2(x,t) \end{pmatrix} \tag{C.9}$$

with the normalization $\langle\psi|\psi\rangle = 1$. The resulting time series $\psi(x,t)$ is used subsequently in the signal calculation.

C.1.1 2D Model with Cationic States

?? To discuss photoionization, we extend the two-dimensional model system described in appendix C.0.3 inspired by the S_2-S_1 CI in acrolein [113, 52, 36]. The cation states D_0 and D_1 are in the same nuclear coordinate system as the neutral states and determined at the

Table C.2: Parameters for the Polynomial expansions of the diabatic states of the two dimensional model. and couplings (given in atomic units).

Surf.	c_{00}	c_{10}	c_{01}	c_{20}	c_{11}	c_{02}	c_{30}	c_{21}	c_{12}	c_{03}
V_3	0.260	0.02054	-0.0402	0.3953	-0.03684	0.1665	0.3105	0.1293	-0.2761	0.1213
V_4	0.2862	0.0007407	-0.07507	0.1504	-0.232	0.1897	0.2963	0.2851	-0.3168	0.09636

Table C.3: Parameters for the 4th order parameters of V$_4$ (Eq. (C.10))(given in atomic units).

c_{40}	c_{31}	c_{22}	c_{13}	c_{04}
0.4607	0.4479	0.2463	-0.1592	0.01413

CASSCF(5/5)/6-31+G* level of theory. The PES for the D$_0$ state is fitted with Eq. (C.4). The ion state D$_1$ (V_4) is fitted by a fourth order polynomial:

$$f_2(x_h, x_g) = f_1(x_h, x_g) + c_{40}x_h^4 + c_{31}x_h^3x_g + c_{22}x_h^2x_g^2 + c_{13}x_hx_g^3 + c_{04}x_g^4 \tag{C.10}$$

The respective parameter sets c_{ij} for the ion states Vs are given in table C.2. The additional 4th order parameters for V_4 are given in table C.3. The parameters for the two neutral states as well as a graphical representation are given in Ref. [88]. The polynomial allows for extrapolation of the data to a wider parameter range, necessary to run the wave packet simulations. The potential energy surfaces of the cation states are shown in Fig. C.4.

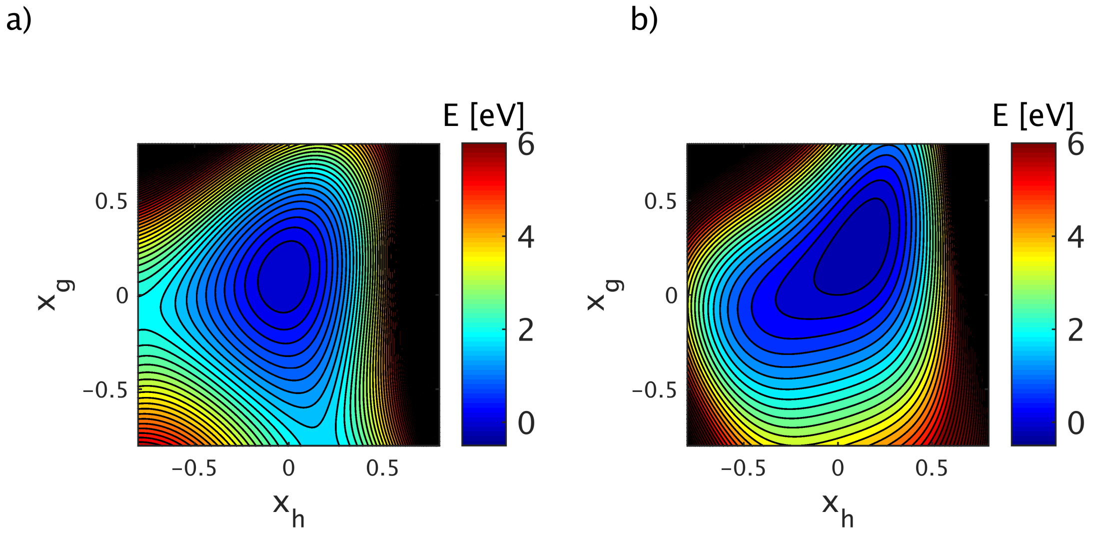

Figure C.4: Potential energy surfaces of the cation states a) V_3 and b) V_4.

Appendix D

Useful Formulas

We collect here various important formulas used in calculating the signals discussed in the main text. Due to it's intimate connection with the material time-propagator, the Fourier transform of the Heaviside theta function

$$\int dt\theta(t)e^{it(\omega-\omega_0+i\Gamma)} = \frac{i}{\omega-\omega_0+i\Gamma} \tag{D.1}$$

plays an important role. An ultrashort pulse with central time t_j and carrier frequency ω_j can be representated as the sum of positive and negative frequency components

$$E_j(t) = \mathcal{E}_j^*(t)e^{i\omega_j(t-t_j)} + \mathcal{E}_j(t)e^{-i\omega_j(t-t_j)} \qquad \Rightarrow \qquad E_j(\omega) = e^{i\omega_j t_j}\left(\mathcal{E}_j(\omega) + \mathcal{E}_j^*(\omega)\right) \tag{D.2}$$

where $\mathcal{E}_j(t)$ is the spectral pulse envelope centered at t_j and $\mathcal{E}_j(\omega)$ and $\mathcal{E}_j^*(\omega)$ are spectral pulse envelopes centered at $\pm\omega_j$ respectively. To simulate signals, we will often employ Gaussian pulses

$$\mathcal{E}_j(t) = \frac{\sigma_j}{\sqrt{2\pi}}e^{-\frac{\sigma_j^2(t-t_j)^2}{2}}e^{i\phi_j} \qquad \mathcal{E}_j(\omega) = \frac{1}{\sqrt{2\pi}}e^{-\frac{(\omega-\omega_j)^2}{2\sigma_j^2}}e^{i\phi_j} \tag{D.3}$$

where σ_j is the standard deviation of the j-th spectral pulse envelope, $\sigma_j^{(-1)}$ is the corresponding temporal standard deviation, and ϕ_j is an arbitrary phase.

D.0.2 Wavefunction vs. Density Matrix

It is well known that, because of decoherence phenomena due to system-bath interactions, non-isolated systems can not always be described as a pure state $|\psi\rangle$ [6] but rather as a statistical mixture $\rho = \sum_k P_k |\psi_k\rangle\langle\psi_k|$. Expectation values of operators are evaluated via

$$\langle \hat{O} \rangle = \langle \psi | \hat{O} | \psi \rangle \leftrightarrow \mathrm{Tr}\,[\hat{O}\rho]. \tag{D.4}$$

The time evolutions of $|\psi\rangle$ and ρ are given by

$$|\psi(t)\rangle = U(t,t')|\psi(t')\rangle \leftrightarrow \rho(t) = \mathcal{U}(t,t')\rho(t') \rightarrow U(t,t')\rho(t')U^{\dagger}(t,t') \tag{D.5}$$

where

$$U(t,t') = \mathcal{T} e^{-i\int_{t'}^{t} H'(\tau)d\tau} \tag{D.6}$$

is the time-ordered exponential propagator and we work in the interaction picture with respect to $\hat{H}'(t)$ so that operators pick up the field-free time dependence

$$\hat{O}(t) = e^{i\hat{H}_0 t}\hat{O}e^{-i\hat{H}_0 t}. \tag{D.7}$$

Note that the last arrow in Eq. (D.5) assumes Hamiltonian, commutator evolution of ρ

$$\dot{\rho} = -i[\hat{H}'(t), \rho] \tag{D.8}$$

and more general evolutions are certainly possible. [NOTE: make reference to masters equations Lindbladd, etc]. In the most general case, the evolution of the density matrix will be determined by a tetradic operator $\mathcal{L}$ called the Liouvillian

$$\dot{\rho}_{lk} = -i \sum_{mn} \mathcal{L}_{lk,mn} \rho_{mn} \tag{D.9}$$

In such a situation, it pays recast the problem in Liouville space, in which ρ is a vector and the above evolution equation can be handled with the usual matrix techniques. There are thus three levels at which we may describe a quantum system. The Liouville-space approach is the most general and most numerically taxing. When system-bath interactions are negligible, we may choose a wavefunction or density-matrix based approach and utilize Hamiltonian time-evolution in Hilbert space. In this manuscript, we will calculate all expectation values in Hilbert space. In chapter 2, we give eigenstate expansions in terms of the more-general density-matrix expressions while also including formal time-evolution expressions in terms of both ρ and $|\psi\rangle$. In chapter 3, we make the simplifying assumption of a pure state for the purposes of illustrating the nuclear dynamics. Both approaches are then discussed in the context of photoelectron spectroscopy in chapter 4. Finally, we note that more general propagations can be bundled into the calculation of the "initial" density matrix. This makes the density-matrix expressions in chapter 2 entirely general as long as system-bath interactions are negligible during the probing process itself.

D.0.3 Polarizability due to Gaussian Pulses

Above, we have encountered the polarizability due to a hybrid pulse

$$\alpha_{ca}^{(jk)}(\omega) = \sum_{x} \frac{\tilde{\mathcal{E}}_j^*(\omega)\tilde{\mathcal{E}}_k(\omega + \omega_j - \omega_k + \omega_{ca})(\epsilon_j \cdot \mathbf{V}_{cx})(\epsilon_k \cdot \mathbf{V}_{xa})}{\omega + \omega_j - \omega_{xa} + i\Gamma_x}. \tag{D.10}$$

This frequency-dependent polarizability can take the place of the final interaction or an earlier interaction in the perturbative expansion of a particular signal. In the latter case, the integrated polarizability

$$\alpha_{ca}^{(jk)} = \int \frac{d\omega}{2\pi}\alpha_{ca}^{(jk)}(\omega) \tag{D.11}$$

is required. With the choice of Gaussian pulses, these integrals can be evaluated analytically, easing the computational burden of simulating signals. In this subsection, we evaluate this quantity for a hybrid Gaussian pulse. Plugging Eqs. (D.10)-(D.3) into Eq. (D.11) gives

$$\alpha_{ca}^{(jk)} = \frac{\sum_{\nu}\hat{V}_{cx}^{(\nu)}\hat{V}_{xa}^{(\nu)}}{3(2\pi)^2\sigma_j\sigma_k}\int d\omega\frac{\exp\left(-\frac{\omega^2}{2\sigma_j^2}\right)\exp\left(-\frac{(\omega+\omega_j-\omega_k+\omega_{ca})^2}{2\sigma_k^2}\right)}{\omega+\omega_j-\omega_{xa}+i\Gamma_x} \tag{D.12}$$

where ν indexes cartesian coordinates and we have employed an isotropic average to reduce the dot products between the field vectors and the transition dipole moments. Completing the square in the numerator gives

$$\alpha_{ca}^{(jk)} = \sum_{x,\nu}\frac{\hat{V}_{cx}^{(\nu)}\hat{V}_{xa}^{(\nu)}}{3(2\pi)^2\sigma_j\sigma_k}\exp\left(-(\omega_j-\omega_k+\omega_{ca})^2(\frac{1}{2\sigma_k^2}-\sigma_{jk}^2)\right)\int d\omega\frac{\exp\left(-\frac{(\omega+\tilde{\omega})^2}{\sigma_{jk}^2}\right)}{\omega+\omega_j-\omega_{xa}+i\Gamma_x} \tag{D.13}$$

where we have defined $\sigma_{jk}^2 = \frac{2\sigma_j^2\sigma_k^2}{\sigma_j^2+\sigma_k^2}$ and $\tilde{\omega} = (\omega_j-\omega_k+\omega_{ca})\frac{\sigma_{jk}^2}{2\sigma_j^2}$. Defining the integral in the last factor of the above, we shift the integration and employ Eq. (D.1)

$$A \equiv \int d\omega\frac{\exp\left(-\frac{(\omega+\tilde{\omega})^2}{\sigma_{jk}^2}\right)}{\omega+\omega_j-\omega_{xa}+i\Gamma_x} = -i\int_0^\infty dt e^{it(\omega_j-\tilde{\omega}-\omega_{xa}+i\Gamma_x)}\int d\omega e^{it\omega}e^{-\frac{\omega^2}{\sigma_{jk}^2}}. \tag{D.14}$$

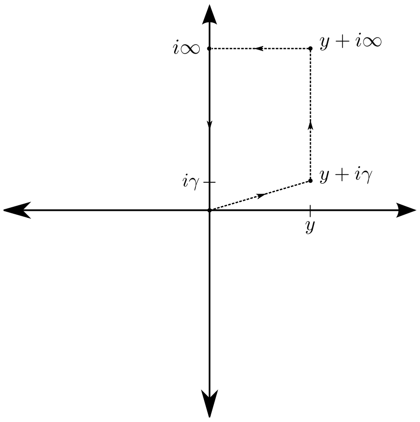

Figure D.1: Illustration of the contour of integration for Eq. (D.18).

The $d\omega$ integration can now be carried out as a simple Gaussian integral via completing the square. This gives

$$A = -i\sigma_{jk}\sqrt{\pi}\int_0^\infty dt e^{it(\omega_j-\tilde{\omega}-\omega_{xa}+i\Gamma_x)} e^{-\frac{t^2\sigma_{jk}^2}{4}} \tag{D.15}$$

Completing the square again then gives

$$A = -i\sigma_{jk}\sqrt{\pi} e^{-\frac{(\omega_j-\tilde{\omega}-\omega_{xa}+i\Gamma_x)^2}{\sigma_{jk}^2}} \int_0^\infty dt e^{-\frac{(t-i\frac{2}{\sigma_{jk}}(y+i\gamma))^2\sigma_{jk}^2}{4}} \tag{D.16}$$

where we have defined $y = \frac{\omega_j-\tilde{\omega}-\omega_{xa}}{\sigma_{jk}}$ and $\gamma = \frac{\Gamma_x}{\sigma_{jk}}$. To do this last integral, we switch to complex variable $\tau = \frac{\sigma_{jk}}{2}(i(t+\frac{2\gamma}{\sigma_{jk}}) + \frac{2y}{\sigma_{jk}})$, resulting in

$$A = -i\sigma_{jk}\sqrt{\pi} e^{-\frac{(\omega_j-\tilde{\omega}-\omega_{xa}+i\Gamma_x)^2}{\sigma_{jk}^2}} \frac{2}{i\sigma_{jk}} \int_{y+i\gamma}^{y+i\infty} d\tau e^{\tau^2}. \tag{D.17}$$

This last integral may be evaluated using the residue theorem. We employ the contour shown in Fig. D.1. Since the integrand has no poles in the complex plain, the contour integral vanishes

$$\oint_{\mathcal{C}} d\tau e^{\tau^2} = 0 = \int_{y+i\gamma}^{y+i\infty} d\tau e^{\tau^2} + \int_{y+i\infty}^{i\infty} d\tau e^{\tau^2} + \int_{i\infty}^{0} d\tau e^{\tau^2} + \int_{0}^{y+i\gamma} d\tau e^{\tau^2}. \tag{D.18}$$

Now, it is clear that

$$\int_{y+i\infty}^{i\infty} d\tau e^{\tau^2} = \int_{y}^{0} d\tau' e^{\tau'^2} e^{2i\tau'\infty} e^{-\infty^2} \to 0 \tag{D.19}$$

so that the closure at $i\infty$ contributes nothing. The integral down the imaginary axis

$$\int_{i\infty}^{0} d\tau e^{\tau^2} = -i\frac{\sqrt{\pi}}{2} \tag{D.20}$$

is easily evaluated, and the last integral is

$$\int_{0}^{y+i\gamma} d\tau e^{\tau^2} = \frac{\sqrt{\pi}}{2}\mathrm{erfi}(y+i\gamma) \tag{D.21}$$

We thus have

$$A = -\pi e^{-\frac{(\omega_j-\tilde{\omega}-\omega_{xa}+i\Gamma_x)^2}{\sigma_{jk}^2}}[i-\mathrm{erfi}(y+i\gamma)] \tag{D.22}$$

and

$$\begin{aligned}\alpha_{ca}^{(jk)} = &\sum_{x,\nu}\frac{\hat{V}_{cx}^{(\nu)}\hat{V}_{xa}^{(\nu)}}{12\pi\sigma_j\sigma_k}\exp\left(-(\omega_j-\omega_k+\omega_{ca})^2(\frac{1}{2\sigma_k^2}-\sigma_{jk}^2)\right) \\ &\times\exp\left(-\frac{(\omega_j-\tilde{\omega}-\omega_{xa}+i\Gamma_x)^2}{\sigma_{jk}^2}\right)\left[\mathrm{erfi}(\frac{\omega_j-\tilde{\omega}-\omega_{xa}+i\Gamma_x}{\sigma_{jk}})-i\right]\end{aligned} \tag{D.23}$$

where, for brevity, we abstain from re-substituting $\tilde{\omega}$ terms of the original quantities. This expression is useful in simulation certain signals from chapter 2 when utilizing Gaussian pulses.